Lehrstuhl für Solartechnik

RWTH AACHEN UNIVERSITY

Diese Arbeit wurde vorgelegt am DLR - Institut für Solarforschung, Lehrstuhl für Solartechnik

Modellierung, technische Analyse und Simulationstool-Entwicklung eines solarbasierten Methanolsyntheseprozesses

Modelling, technologic analysis and simulation tool development of a solar-based methanol synthesis process

Masterarbeit
Masterthesis

vorgelegt von
Adrian Bäuml
370538

Erstprüfer: Univ.-Prof. Dr.-Ing. Robert Pitz-Paal
Zweitprüfer: Univ.-Prof. Dr. rer. nat. Christian Sattler

Betreuender wiss. Mitarbeiter: Diego Andres Cordoba Lopez

Köln-Porz, den 27. Mai 2024

Abstract

As global methanol demand is rising and with it the CO_2 emissions due to its production, the need for green alternatives is growing faster. To address this environmental challenge, the German Aerospace Center (DLR) is developing a Python-based yield calculation software for solar plants to investigate pathways for efficient production of electricity or process heat. This work adds multiple components to the existing library of this yield calculator to feature a complete methanol synthesis process from CO_2. By integrating an alkaline electrolyzer, a fixed-bed reactor with gas recycling, and a distillation unit, the implemented components address both the nonlinear efficiency and the complex dynamics of startup processes. These components and their aggregation into a synthesis plant were validated with results from recent literature. The components were analyzed on a technological level regarding their behaviour during startup procedures and load changes to identify potential bottlenecks in production. However, without an economic analysis, no single component stood out as the most critical regarding the startup of the system. With the employed control strategy, the methanol reactor takes longer to adapt too load changes than the other two components due to long residence times of the synthesis gases, while different control strategies could prevent or reduce this divergence.

Kurzdarstellung

Da die globale Methanolnachfrage steigt und damit auch die CO_2-Emissionen durch dessen Produktion, wächst der Bedarf an grünen Alternativen schneller. Um diese Umweltproblematik anzugehen, entwickelt das Deutsche Zentrum für Luft- und Raumfahrt (DLR) eine Python-basierte Ertragsberechnungssoftware für Solaranlagen, um Wege für eine effiziente Produktion von Strom oder Prozesswärme zu untersuchen. Diese Arbeit fügt der bestehenden Bibliothek dieses Ertragsrechners mehrere Komponenten hinzu, um einen vollständigen Methanolsyntheseprozess aus CO_2 darzustellen. Durch die Integration eines alkalischen Elektrolyseurs, eines Festbettreaktors mit Gasrecycling und einer Destillationseinheit werden sowohl die nichtlineare Effizienz der Komponenten als auch die komplexen Dynamiken der Startprozesse adressiert. Diese Komponenten und ihre Aggregation zu einer Syntheseanlage wurden anhand von Ergebnissen aus aktuellen Literatur validiert. Die Komponenten werden auf technischer Ebene hinsichtlich ihres Verhaltens während der Anfahrvorgängen und Lastwechseln analysiert, um mögliche Engpässe in der Produktion zu identifizieren. Ohne einen wirtschaftlichen Ansatz erwies sich jedoch keine einzelne Komponente als die kritischste beim Anfahren der Anlage. Mit der angewandten Regelstrategie benötigt der Methanolreaktor länger, um sich an Laständerungen anzupassen, als die anderen beiden Komponenten, aufgrund der langen Verweilzeiten der Synthesegase. Unterschiedliche Regelstrategien könnten jedoch diese Abweichung verhindern oder reduzieren.

Contents

List of Figures

List of Tables

Nomenclature

Abbreviations

Acronym	Description
AEL	Alkaline Electrolyzer
AEM	Anion Exchange Membrane
CSTR	Continuous Stirred-Tank Reactors
DMFC	Direct Methanol Fuel Cell
HHV	Higher Heating Value
HTF	Heat-Transfer-Fluid
KPI	Key Performance Indices
LHHW	Langmuir-Hinshelwood-Hougen-Watson
LHV	Lower Heating Value
MTM	McCabe-Thiele-Method
NRTL	Non-Random Two-Liquid
PEM	Polymer Electrolyte Membrane
PFR	Plug Flow Reactors
RWGS	Reverse-Water-Gas-Shift-Reaction
SOEC	Solid Oxide Electrolyzer
VLE	Vapor-Liquid-Equilibria
WGS	Water-Gas-Shift-Reaction
YACOP	Yield Assessment Calculation and Optimization Program

1 Introduction

Methanol plays a crucial role as an energy source and serves as a fundamental chemical in the chemical industry, particularly for the synthesis of formaldehyde, which accounts for 29% of all methanol usage. It can also be used as a fuel for specially adapted petrol engines. Starting from 2009, multiple national fuel blending standards went into effect in China, including mixtures of 85% (M85) and 100% (M100) methanol blends [BM16]. In total, gasoline blends and biodiesel account for 14% of all methanol usage. Methanol is also expected to play significant roles as hydrogen carrier or in direct methanol fuel cells (DMFCs), especially as DMFC efficiency continues to improve [BM16]. The global methanol demand is illustrated in figure 1.1. In 2015, it was around 60 to 70 million tons per year (Mt/year) and is expected to increase to 190 Mt/year by the year 2030. Additionally, more than 80% of methanol production is based on steam reforming [Dai16].

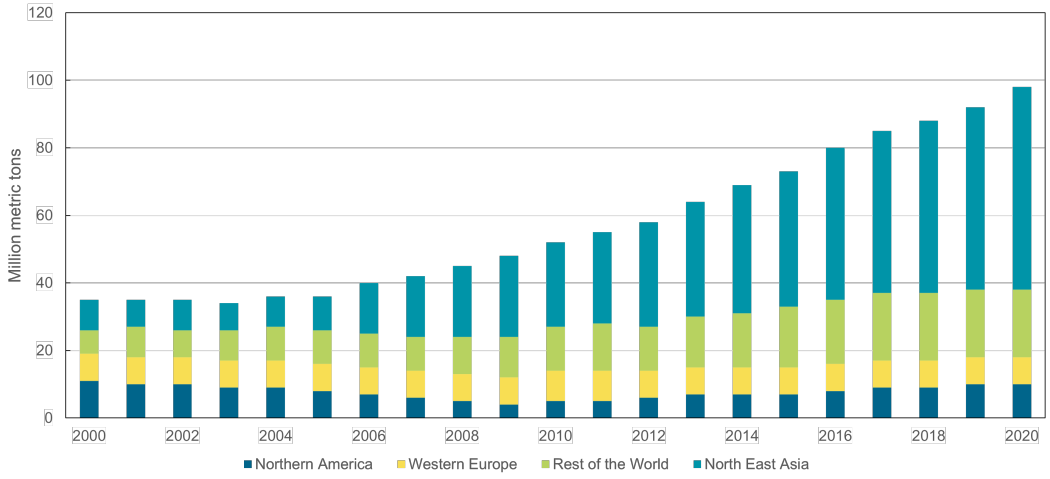

Figure 1.1: Global Methanol demand from 2000 to 2020 [Alv16]

The traditional methanol synthesis process utilizes fossil raw materials such as natural gas, and crude oil, or coal for production, which are associated with high specific CO_2 emissions throughout the product cycle. However, by combining renewable energies such as solar power plants with the provision of necessary raw materials through green hydrogen, CO_2 emissions can be significantly reduced. Such plants are already in operation, such as the George Olah plant in Iceland, which has an annual production of 1.3-4 million tons (Mt) of methanol per year. This plant began production in 2012 as the first commercial facility of its kind [Car12]. Another notable plant is the Shunli

methanol plant in China, which has been producing 110 Mt of methanol since the third quarter of 2022 [Car22]. Both of these plants achieve an impressive 80-90% reduction in carbon dioxide emissions compared to conventional plants. Therefore, Methanol is often regarded as a promising alternative to fossil fuels [WS17].
In this thesis, a model of the complete methanol synthesis, including distillation, will be developed using the Python-based yield calculation software YACOP. The hydrogen required for methanol synthesis will be provided via an alkaline electrolyzer, which will also be implemented as part of this work.
Alkaline electrolysis recognized for its scalability and maturity, serves as a pivotal component in large-scale plant applications. This technology has undergone extensive research and development. In this thesis, the simulation framework is built upon detailed physical and chemical models of both electrolysis and methanol synthesis. The synthesis reactor model is designed to be versatile, accommodating various reactor types with the flexibility to adjust kinetic modeling parameters. This approach ensures a dynamic and interconnected simulation platform for studying methanol production processes.
Furthermore, the distillation column model will be designed to predict product concentrations and accurately calculate heat flow duties. Methanol synthesis and distillation are both characterized by lengthy start-up times, necessitating the development of an effective operating strategy that considers these dynamics. The dynamic behavior of the components, crucial not only during startup, but also during load changes, will be a key focus. Validation of the models will involve comparing simulation results with existing literature findings to ensure accuracy and reliability.
This work aims to address the feasibility of implementing chemical processes within YACOP and identify the conditions under which such realizations are possible. Additionally, the study will assess the functionally critical components of production within the context of the implemented model. The objective is to provide insights into the operational requirements and limitations of simulating chemical processes using YACOP, focusing on key components that significantly influence process performance and efficiency.
The first chapter will focus on the literature concerning the three key components implemented in the framework of this thesis. Starting with the alkaline electrolyzer, and continuing with the methanol synthesis reactor and the distillation unit, the chapter will close with a presentation of complete methanol synthesis plants reported in past publications.
In the methodology chapter, the simulation environment is presented. Then the implemented models are further explained in detail.
Afterwards, the results of the component validations using literature are presented. As done in the previous chapters, the components are looked at independently at first, while the results of the system evaluation are presented at last.
The last chapter is summarizing the underlying models and results of this work, while also giving an outlook on further research approaches.

2 State of the Art

This chapter is delivering an overview of advancements in the field of renewable methanol synthesis, while firstly addressing the components of synthesis plants individually, starting with the electrolyzer. Alkaline electrolysis is a well-established method for producing hydrogen and is increasingly being integrated with renewable energy to produce what is known as "green hydrogen". This process utilizes electricity generated from renewable sources such as solar, wind, or hydroelectric power to power the electrolysis of water, resulting in hydrogen production without carbon emissions, thus contributing to a more sustainable energy landscape. This part discusses recent improvements in the design and efficiency of these systems and the challenges of scaling them up for industrial use. The next component is the reactor for the actual methanol synthesis from CO_2. Methanol synthesis from carbon dioxide and hydrogen represents a sustainable approach by utilizing captured carbon dioxide from carbon capture processes, thereby benefiting the environment. In this chapter, we look into chemical reactors and explore various methods for modeling chemical reactions, with a focus on plug flow reactors. Subsequently, we examine past studies related to methanol synthesis in fixed bed reactors, analyzing and comparing their findings and methodologies. This investigation aims to provide insights into effective reactor design and optimization for sustainable methanol production processes.

The next section of this chapter focuses on the separation of methanol and water through distillation. It begins with a mathematical description of Vapor-Liquid-Equilibria (VLE) and introduces various models for determining activity coefficients. The McCabe-Thiele-Method is then presented, which is used for designing distillation columns based on material balances. This section concludes with discussion on startup simulations of methanol-water distillation columns, highlighting the operational consideration and dynamics involved in initiating these processes.

Finally, complete methanol synthesis plants are introduced, focusing mainly on plants with similar levels of detail and reactors.

Overall, this chapter aims to provide a comprehensive overview of the latest research and advancements in methanol production using solar power. It underscores the importance of interdisciplinary collaboration across diverse fields, including chemical engineering, renewable energy, and environmental science, to drive the progress of sustainable energy solutions.

2.1 Electrolysis

Currently, over 95% of hydrogen production is derived from fossil fuels, primarily through steam-reforming, a process that demands elevated temperatures ranging from 700°C to 1000°C. Unfortunately, this method generates approximately 10 kilograms of CO_2 emissions for each kilogram of hydrogen produced [LDL+22]. Despite its economic advantage, steam-reforming's viability is increasingly challenged by carbon taxation, particularly in Europe. In contrast, green or low-carbon hydrogen is an important tool for decarbonizing energy and chemical sectors, usually achieved via electrolysis. [LDL+22]

Electrolysis disassembles water molecules into hydrogen and oxygen using electrical energy. Hydrogen forms at the cathode (negative electrode) and oxygen at the anode (positive electrode), with an electrolyte situated in between to enable ion transfer and serve as both an electrical and ionic conductor. The specific ions involved, H^+, OH^-, or O^{2-}, dictate the electrolyzer's classification as either polymer electrolyte membrane- (PEM), acidic-, alkaline-(AEL), or solid oxide electrolyzer. An essential component of electrolyzer cells is a separator or diaphragm, which ensures that the produced gases—hydrogen and oxygen—do not mix, allowing them to be extracted individually [BT20].

Electrolyzers operate under diverse pressures and temperatures. PEM and alkaline units typically function at temperatures below 80°C and 220°C, respectively, while solid oxide electrolyzers need temperatures above 600°C. Momentarily, PEM electrolyzers stacks are less powerful, however, the gap between stack sizes of alkaline electrolyzers and PEM electrolyzers is growing smaller. [The]

Both alkaline and PEM electrolyzers, display similar electrical efficiencies between 50 to 83 kWh per Kg hydrogen, or 4.09 to 6.8 kWh per cubic meter hydrogen. [LADF14] However, the capital costs of alkaline electrolyzer systems remain significantly lower compared to PEM electrolyzers with similar maximum power, primarily due to the use of cheaper electrode materials. This cost advantage currently makes alkaline electrolyzers more attractive for commercial and large-scale applications.

Anion Exchange Membrane (AEM) technology is an emerging technology that aims to combine the advantages of alkaline and PEM electrolyzers. AEM electrolyzers operate under alkaline conditions, potentially reducing the need for precious metal catalysts and thus lowering costs. Promising high efficiency and flexibility in operation. However, the technology is still in the early stages of commercial deployment.

Solid Oxide Electrolyzers (SOEC) operate at high temperatures, often exceeding 700°C, which enables highly efficient hydrogen production, potentially achieving over 80% efficiency in terms of the higher heating value (HHV) of hydrogen. These electrolyzers can utilize heat from external sources, making them well-suited for integration with industrial processes that generate waste heat. However, the high operating temperatures present challenges related to materials durability and long-term operation reliability. [The]

Tech.	Operation Temp.	Efficiency (kWh/kg H_2)	Capital Cost
AEL	Up to 80°C	50 - 83	Low
PEM	Up to 80°C	50 - 83	Higher
AEM	Similar to AEL/PEM	Potentially high	Lower*
SOEC	Above 600°C	Potentially over 80% HHV	High**

Table 2.1: Comparison of electrolyzer technologies. *AEM aims to reduce costs by avoiding precious metals. **SOEC's costs are due to high-temp operation. [LADF14]

2.1.1 Alkaline Electrolysis

This section will focus more on the alkaline electrolysis. According to the reaction described in equation 2.1, the excess electrons at the cathode lead to the formation of hydrogen and hydroxide ions. These ions subsequently migrate towards the anode due to their negative charge.

$$4\,H_2O + 4\,e^- \rightarrow 2\,H_2 + 4\,OH^- \tag{2.1}$$

The oxidization of the hydroxide ions at the anode produces water and oxygen according to reaction 2.2:

$$4\,OH^- \rightarrow 2\,H_2O + O_2 + 4\,e^- \tag{2.2}$$

To prevent the mixing of gases produced in the cell and to avoid the formation of a short circuit between the electrodes, an effective separator is essential [GRZ17]. An easy schematic diagram of an alkaline electrolysis cell is shown in figure 2.1.

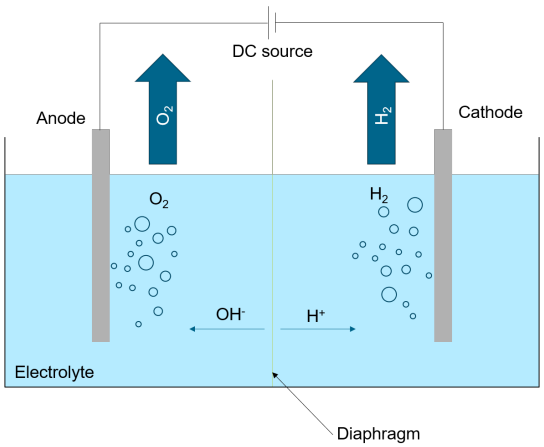

Figure 2.1: Simple schematic of an alkaline electrolysis cell

The cell voltage required for chemical reaction 2.1 and 2.2 can be determined by the

the free reaction enthalpy ΔG_R represented in equation 2.4 for the overall reaction 2.3.

$$2\ H_2O \rightarrow 2\ H_2 + O_2 \tag{2.3}$$

$$\Delta G_R = \Delta H_R - T \cdot \Delta S_R \tag{2.4}$$

Here, ΔH_R is the reaction enthalpy, T is the temperature in Kelvin and ΔS_R is the reaction entropy.
Using ΔG_R, the cell voltage can be calculated by applying equation 2.5:

$$U_{rev} = -\Delta G_R/(nF) \tag{2.5}$$

in which $n = 2$ is the number of exchanged electrons, and $F = 96485 Cmol^{-1}$ is the faradaic constant. At a temperature of 25°C and ambient pressure of 1 bar, the free reaction enthalpy for the total reaction is $\Delta G_R = 237 kJmol^{-1}$, leading to a reversible cell voltage of $U_{rev} = -1.23V$. As the free reaction enthalpy is positive at standard conditions, electrolysis is a non-spontaneous reaction, meaning energy is to be added to the system. [Ull03]
The actual cell voltage needs to be higher than the reversible cell voltage, due to irreversibilities in the reaction. Therefore, the thermo-neutral cell voltage U_{th} described by equation 2.6 accounts for the necessary voltage for water splitting, considering irreversible thermal losses. The enthalpy change ΔH_R can be calculated from equation 2.4.

$$U_{th} = -\Delta H_R/(nF) \tag{2.6}$$

At standard conditions, where the reaction enthalpy for the total reaction is $\Delta H_R = 286 kJmol^{-1}$, the thermo-neutral cell voltage is $U_{th} = -1.48V$. [Ull03]
Finally, the energy efficiency is calculated using the thermo-neutral voltage (2.6) and the actual cell voltage U with the following expression:

$$\eta_e = \frac{U_{th}}{U} \tag{2.7}$$

2.1.2 Modeling Approach

The basis for the implemented alkaline electrolyzer were the models presented by Ulleberg [Ull03] and Sanchez et al. [SARCJ18]. Ulleberg provided an accurate mathematical model for an advanced alkaline electrolyzer, based on the combination of fundamental thermodynamics, heat transfer theory, and empirical electro-chemical relationships. The polarization curve proposed by Ulleberg is shown in equation 2.8:

$$U_{\text{cell}} = U_{\text{rev}} + (r_1 + r_2 \cdot \theta) \cdot i + s \cdot \log\left[\left(1 + \frac{t_2}{\theta} \cdot + \frac{t_3}{\theta^2} \cdot\right) j + 1\right] \tag{2.8}$$

where:

- U_{cell} is the cell voltage.
- i is the current density.
- θ is the temperature in °C.

The rest of the parameters are listed below in table 2.2. The reference system for Ulleberg was the stand-alone photovoltaic hydrogen energy plant in Jülich, meaning all empirical parameters and the validation of Ulleberg were based on the PHOEBUS plant in Jülich (26 kw, 7 bar), and the HYSOLAR (10 kw, 5 bar) test and research facility in Stuttgart [Ull03].

Parameter	**Equation** 2.8	**Equation** 2.9	**Unit**
r_1	$8.05 \cdot 10^{-5}$	$4.45153 \cdot 10^{-5}$	Ωm^2
r_2	$-2.5 \cdot 10^{-7}$	$6.88874 \cdot 10^{-9}$	$\Omega m^2 °C^{-1}$
s	0.185	0.33824	V
t_1	-1.002	-0.01539	$m^2 A^{-1}$
t_2	8.424	2.00181	$m^2 °C A^{-1}$
t_3	247.3	15.24178	$m^2 °C^2 A^{-1}$
d_1	–	$-3.12996 \cdot 10^{-6}$	Ωm^2
d_2	–	$-4.47137 \cdot 10^{-7}$	$\Omega m^2 \text{bar}^{-1}$

Table 2.2: Polarization curve parameters of Ulleberg and Sanchez et al.

Sanchez et al. incorporated two additional parameters, d_1 and d_2, to include the variation of the cellular voltage according to the pressure changes, resulting in polarization curve 2.9 with p being the pressure of the electrolyzer in bar [SARCJ18]:

$$U_{\text{cell}} = U_{\text{rev}} + ((r_1 + d_1) + r_2 \cdot \theta + d_2 \cdot p) \cdot i + s \cdot \log\left[\left(1 + \frac{t_2}{\theta} \cdot + \frac{t_3}{\theta^2} \cdot\right) j + 1\right] \tag{2.9}$$

In figure 2.2, the cell voltage is plotted against the current density for various pressures and temperatures, utilizing equation (2.9). The specific parameters used are detailed in table 2.2. As shown in Figure 2.2, the cell voltage exhibits a stronger dependence on temperature than on operating pressure. [BT20] Due to this dependency, high

operation pressures are preferred when gases need to be compressed for storage or further use, as it reduces the compression power required without negatively impacting the electrolyzer's performance. However, this requirement implies that the water supplied to the electrolyzer must also be pressurized to the operating pressure.

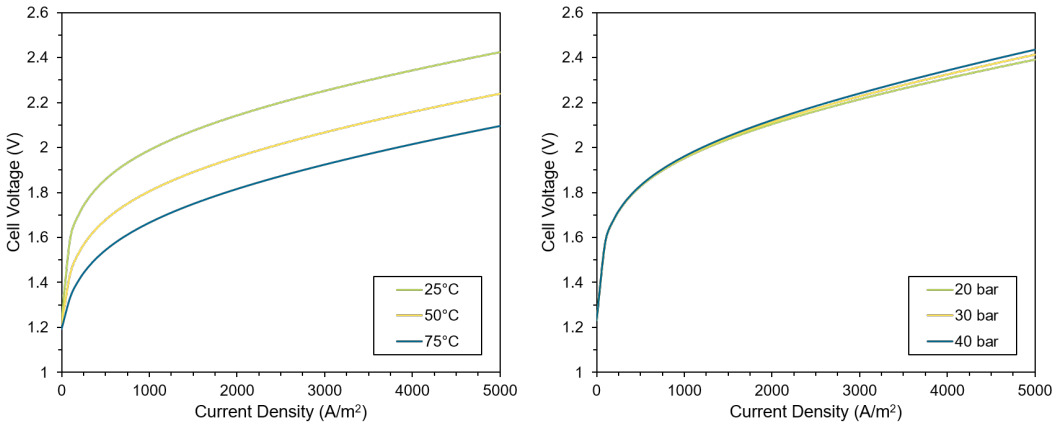

Figure 2.2: Typical I-U curves of an electrolyzer cell at different temperatures

The connection between the consumed power of the electrolyzer and the hydrogen production $n\dot{}_{H_2}$ is expressed in the faradaic efficiency η_F (2.10):

$$\dot{n}_{H_2} = \eta_F \frac{n_c \cdot I}{zF} \quad [mol/s] \tag{2.10}$$

where:

- n_c is the number of cells of the electrolyzer.
- z is the number of electrons per mole hydrogen.
- F is the Faraday constant.
- I is the current.

To calculate the faradaic efficiency, Ulleberg proposed the following expression (2.11):

$$\eta_F = \frac{(I/A)^2}{f_1 + (I/A)^2} f_2 \tag{2.11}$$

where:

- A is the cell area.
- f_1 and f_2 are empirical parameters, listed in table 2.3 for the PHOEBUS electrolyzer at 80°C and multiple temperatures for the HYSOLAR electrolyzer [Ull03].

	PHOEBUS	**HYSOLAR**	**HYSOLAR**	**HYSOLAR**	
T	80	40	60	80	° C
f_1	250	150	200	250	mA^2cm^{-4}
f_2	0.96	0.00	0.985	0.980	0...1

Table 2.3: Faradaic efficiency parameters by Ulleberg [Ull03]

The faradaic efficiency describes the current efficiency, meaning it is the amount of current that is actually producing hydrogen, in relation to the total amount of current flowing in the electrolyzer.

2.1.3 Startup Behavior

In most techno-economic analysis of alkaline water electrolysis, the startup behavior is only implemented superficially by considering a time and cost penalty on the hydrogen production that is not depending on the stack parameters. Bertuccioli et al. [LADF14] observed that modern alkaline electrolyzers typically require anywhere from 20 minutes to several hours to reach their minimum partial load, which usually ranges from 20-40% of the nominal load. The startup time is influenced by the electrolyzer's design (pressurized/unpressurized) and its initial state. Starting from cold state takes longer compared to starting from a power conservation mode, which is a stand-by mode facilitating quicker production resumption after downtime. The ramp-up rates reported in 2014 varied from 0.1% to 10% of the nominal load per second, highlighting the diverse operational behaviors of these electrolyzers [LADF14].
Lüke et al. [LZ20] highlight the robustness of modern alkaline systems, noting that stacks can be ramped up to 50% of the nominal load within one minute by utilizing the excess heat generated during the reaction, to heat up the system afterwards. This capability was demonstrated with a 2 MW alkaline water electrolysis (AWE) system in the *Carbon2Chem* project [SK18].

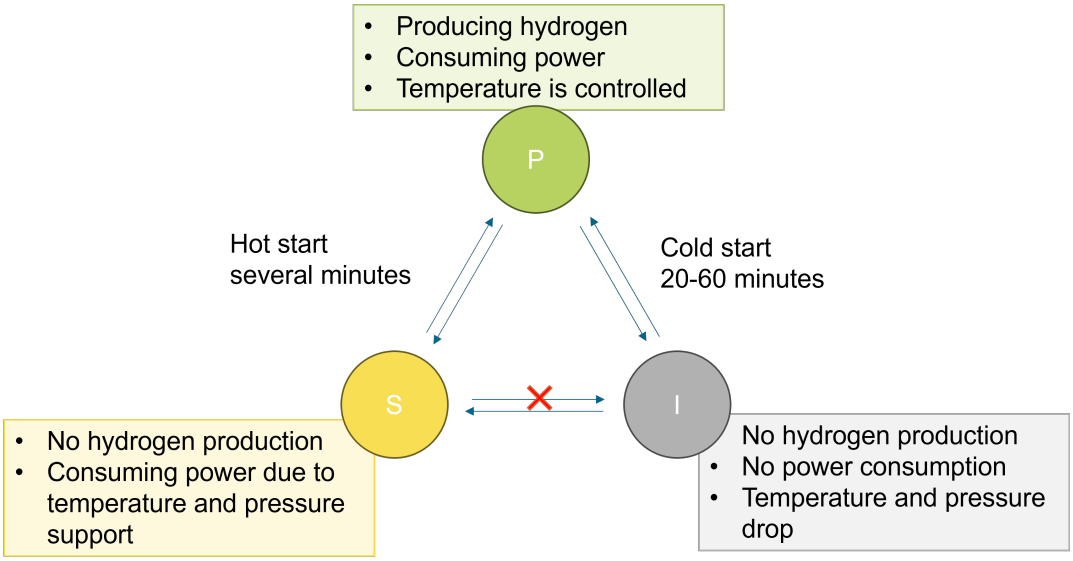

Figure 2.3: State characterization and mutual transitions of Varela et al. [VMZ21]

Varela et al. [VMZ21] addressed the flexibility constraint resulting from the startup time of electrolyzers with an appropriate scheduling approach. They implemented a three state model to describe the operational behavior of the electrolyzer, including the production state, standby state and idle state.
In their study, they used a fixed time step size of 1 h and investigated startup times of 30-60 minutes from an idle state or 20 minutes from a standby state. During the simulation, they implemented a constraint ensuring that an electrolyzer stack

could not resume production without a minimum idle period of 1 h, which effectively extended the startup time to 60 minutes.
During the described standby mode, the hydrogen mass flow is zero, but the electrolyzer continues to consume electricity. In their investigation using a stack size of 2.1 MW electricity nominal load, Varela et al. found that the standby load of 0.3 MW was slightly lower than the minimum partial load of 0.35 MW. This observation underscores the operational characteristics and energy consumption profiles of alkaline electrolyzers during different operational states.
By employing multiple electrolyzer stacks and implementing an effective control strategy over a specific time horizon of one year, Varela et al. demonstrated the ability to utilize 89% of the expected renewable energy. This study emphasizes the advantages of using multiple stacks over single stacks compared to single stacks in mitigating startup penalties, including reduced start up times and costs. [VMZ21]
Zheng et al. [ZYBM22] also introduced a multi-state electrolyzer model and compared different models with various level of detail regarding optimal control strategy and computation time. The difference between the models is expressed in the varying efficiency of the electrolyzer under partial load, fluctuations in temperature and the inclusion of state transitions depending on the level of detail. The simplest model is a model with constant temperature, efficiency and no state transitions. On the other hand, the most complex model incorporates all three variations—varying efficiency with partial load, temperature fluctuations, and state transitions. Intermediate models between these extremes were also explored, encompassing different combinations of these factors.
As Zheng et al. consider a day-ahead dispatch of the electrolyzer system, the electricity prices are known. This means that startup times for hot and cold starts can be planned perfectly according to the optimal monetary yield. The type of startup does however have an effect on the monetary yield, as the cold start costs 98€ and the hot start only costs 10€ [ZYBM22].

2.2 Chemical Reactor

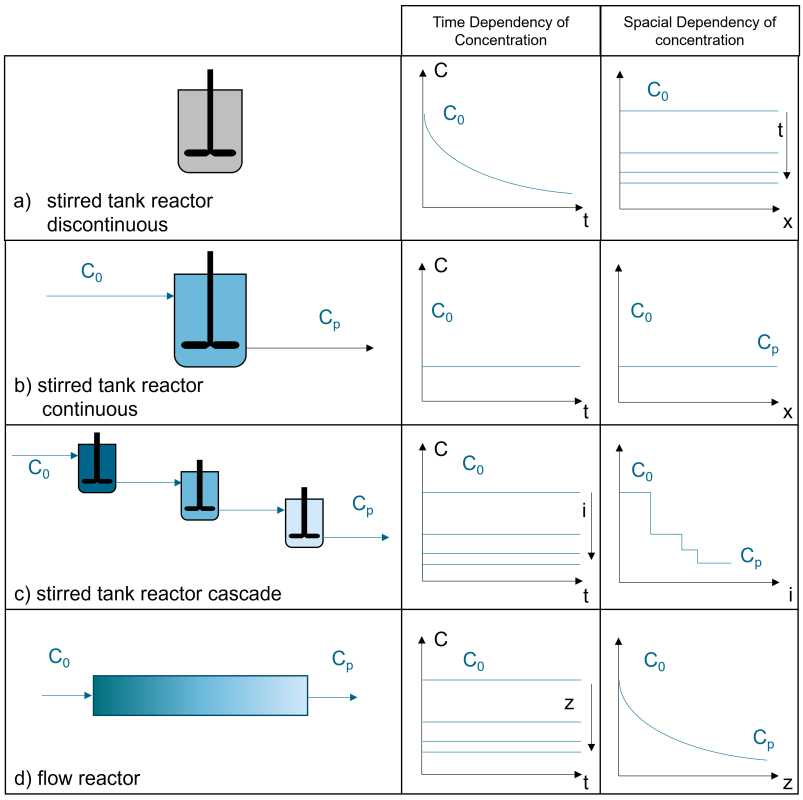

Figure 2.4: Concentration profiles in iso-thermally operated ideal reactors. C: reactant concentration, x: spatial coordinate, t: time, i: number of stages, z: longitudinal coordinate. [BAJV16]

The chemical reactor is the key component of the methanol synthesis. It houses the chemical conversion process, while managing the essential reaction parameters like temperature and pressure. Figure 2.4 shows different concentration profiles of multiple reactor types and the analogy between time and spatial dependency across stirred reactor types and flow reactors. A cascade of continuously operated stirred tank reactors with a large number of tanks is in its behavior similar to a flow reactor. The performance of a reactor is primarily evaluated using technical indices such as conversion, selectivity and yield. Conversion represents the ratio of reactants that have been consumed to the total amount of reactants introduced into the reactor. A higher conversion of reactant A indicates that less of reactant A remains in the system after the reaction has occurred. Selectivity is defined as the ratio of the moles of desired products to the moles of reactant consumed, or alternatively, the moles of desired products to the total moles of products formed including by-products. In the context of methanol synthesis, selectivity describes the ratio of methanol produced to other potential products like water and carbon monoxide, as outlined in 2.2.1. The

yield is a combination of conversion and selectivity, as it describes the amount of desired products divided by the moles of consumed reactant. It is usually expressed as a percentage, indicating how much of the initial reactants ended up as the desired product. Chemical reactors can be classified into two main categories: continuously operated reactors and discontinuous reactors. Continuously operated reactors include systems like Continuous Stirred-Tank Reactors (CSTRs) and Plug Flow Reactors (PFRs), while discontinuous reactors refer to Batch Reactors. The choice of reactor type depends on several factors including reaction kinetics and the scale of production. Each reactor type offers distinct advantages and challenges. Continuous reactors are well-suited for large-scale production and processes with steady-state conditions, offering continuous output and controlled residence times. On the other hand, batch reactors are versatile and suitable for small-scale or flexible production scenarios, allowing for easier control over reaction conditions and product quality in batch-wise operations [BAJV16].
Plug Flow Reactors or Packed Bed Reactors are often used for methanol synthesis from CO_2 as mentioned in [VDB13], [Bus96] and [SBP$^+$20]; which is why their mathematical description is further explained in the following paragraph.
To accurately simulate reactions in a flow reactor, it is essential to develop a precise mathematical description of the reaction kinetics, equilibrium, and the substance and heat transport processes involved. This typically requires a spatially resolved model of the reactor, particularly in the axial dimension. Such model takes into account changes and interactions along the length of the reactor, allowing for a comprehensive analysis of the system's behavior and performance.
The equations for calculating the performance of ideal reactors in isothermal operation are derived from the relevant material balance equations. The difference between the inflow and outflow of a reactant, results from the sum of the formation or consumption by chemical reactions, as well as from the accumulation or depletion of the respective substance in the balanced reaction space. In any reactor, the following continuity approach can be established for each component:

$$\frac{\partial n_j}{\partial x} = \dot{n}_{j,\mathrm{in}} - \dot{n}_{j,\mathrm{out}} + \sum_i \nu_{ij} r_{\mathrm{i,x}} \tag{2.12}$$

where:

- n_j is the amount of component j,
- $\dot{n}_{j,\mathrm{in}}$ is the inflow of component j into the balance room,
- $\dot{n}_{j,\mathrm{out}}$ is the outflow of component j from the balance room x,
- ν_{ij} is the stoichiometric coefficient of component j in the i. reaction,
- $r_{\mathrm{i,x}}$ is the conversion rate of the i. reaction in the balance room.

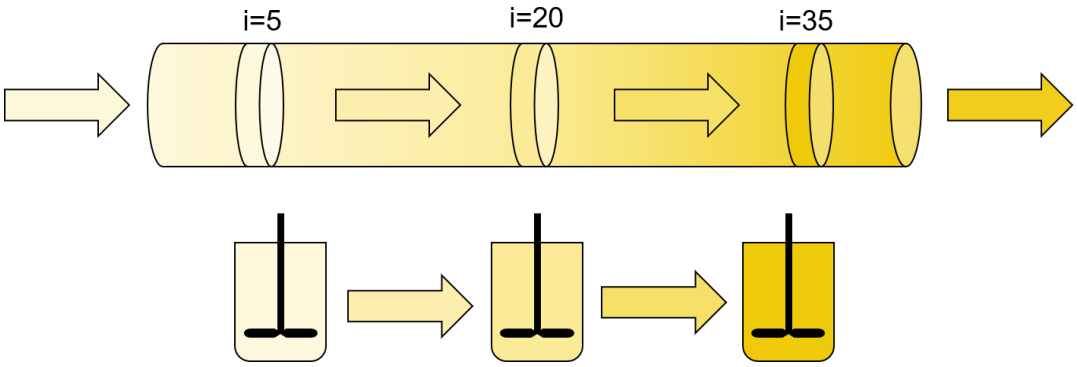

Figure 2.5: Plug flow reactor and stirred batch reactor cascade with 40 hypothetical batch reactors.

The derivative on the left-hand side of equation 2.12 represents the accumulation of component j in the balanced reaction space, hence it becomes zero during steady state operation. When choosing balanced spaces small enough in the reactor, and using the analogy shown in figure 2.4, equation 2.12 can be modified to equation 2.13, while creating a disc balance in the tubular reactor, neglecting radial differences. This step resembles a first order Taylor series approximation.

$$\dot{n}_{j,z} - \dot{n}_{j,z+dz} = -\sum_{i} \nu_{ji} r_{idV} \tag{2.13}$$

where:

- z is the longitudinal coordinate of the flow reactor, with $z = 0$ at the inflow,
- $\dot{n}_{j,z}$ is the inflow of component j at coordinate z,
- $\dot{n}_{j,z+dz}$ the outflow of component j at $z + dz$,
- $\dot{r}_{idV}$ the reaction speed based on the balance room size.

This implementation is equal to a stirred batch reactor cascade with $i = z/dz$ batch reactors. [BAJV16]
In case of catalyst-driven reactions, equation 2.14 can be derived by replacing the reaction speed based on the balance room size for a reaction speed based on catalyst mass in the balance room.

$$\dot{n}_{j,z} - \dot{n}_{j,z+dz} = -\sum_{i} \nu_{ji} r_{i,cat} \tag{2.14}$$

2.2.1 Methanol Synthesis

As the global focus shifts towards sustainable energy, developing alternative liquid fuels for the transport sector has become crucial. These fuels need to be produced using renewable energy sources and non-limited material to ensure a significant reduction in CO_2 emissions compared to current technologies. Methanol, with its dual role as an energy carrier and a basic chemical in the industry, is a prime candidate for these alternative liquid fuels. Traditionally, methanol is synthesized using fossil raw materials such as natural gas and crude oil, leading to high CO_2 emissions. However, integrating solar power plants and green hydrogen into the production process can drastically reduce these emissions. By leveraging renewable energy sources like solar power for methanol production and employing green hydrogen, the process becomes more sustainable and aligns with global CO_2 reduction goals. [WS17] In this section the methanol synthesis equations are introduced, and kinetic modeling approaches are presented. Methanol synthesis from CO_2 can take place in either one or two steps. In one step, the synthesis is described in the reaction equation (2.15). For the reaction in two steps, carbon monoxide CO is first formed via the reverse water-gas shift reaction, as shown in reaction equation (2.17). Carbon monoxide is then available for reaction equation (2.16). [VDB13]

$$CO_{2(g)} + 3\,H_{2(g)} \Leftrightarrow CH_3OH_{(l)} + H_2O_{(g)} \quad \Delta H = -87kJ/mol(298K) \tag{2.15}$$

$$CO_{(g)} + 2\,H_{2(g)} \Leftrightarrow CH_3OH_{(l)} \quad \Delta H = -128kJ/mol(298K) \tag{2.16}$$

$$CO_{(g)} + H_2O_{(g)} \Leftrightarrow CO_{2(g)} + H_{2(g)} \quad \Delta H = -41.2kJ/mol(298K) \tag{2.17}$$

However multiple studies like [SMC98] suggest that (2.15) can be neglected, as the intrinsic rate of CO_2 hydrogenation is approximately 20 times faster than that of CO hydrogenation. This proves that CO_2 is the main source of carbon for the methanol synthesis. This was also proven by Chinchen et al. [CDJ$^+$88] and Rozovksii et al. [Roz89].

There are multiple works in literature that describe the kinetics for equation (2.15) and (2.17), compared among others by Peter et al. [PFR$^+$12]. The authors distinguish between Power Law Models, Langmuir-Hinshelwood-Hougen-Watson(LHHW) Models, and Micro-kinetic Models, each with their own unique advantages and disadvantages. While Power Law Models are usually used to describe chemical reactions for lesser-known mechanisms, LHHW Models and especially Micro-kinetic models require a higher level of understanding. It is reported that the LHHW Model and the Power Law Model as global models can describe the methanol synthesis rate more accurately than the Micro-kinetic Model, yielding only slightly different results. According to the authors, the LHHW Model is better suited to fit data outside the provided experimental window, but in general all three models can predict the reaction rates within the data boundaries of 460-605 K and 5-60 bar. [PFR$^+$12]. Bussche et al. [Bus96] performed an analysis of the kinetic parameters, taking into account both the literature and their own experimental data. To describe the reaction rate of both reactions, the authors propose the following two expressions:

$$r_{MeOH} = K_1 p_{CO_2} p_{H_2} (1 - \frac{p_{H_2O} p_{CH_3OH}}{K_{eq1} p_{H_2} 3 p_{CO_2}}) \frac{1}{\beta^3} \quad [\frac{mol}{kg_{cat} s}] \tag{2.18}$$

$$r_{RWGS} = K_5 p_{CO_2} (1 - \frac{K_{eq2} p_{H_2O} p_{CO}}{p_{H_2} p_{CO_2}}) \frac{1}{\beta} \quad [\frac{mol}{kg_{cat} s}] \tag{2.19}$$

$$\beta = 1 + K_2 \frac{p_{H_2O}}{p_{H_2}} + k_3 p_{H_2}^{0.5} + k_4 p_{H_2O} \tag{2.20}$$

The reaction speed is hereby calculated in dependence of the partial pressures of the reactants and temperature dependent equilibrium constants, and it's unit is $mol/kg_{cat}s$. This results in the Langmuir-Hinshelwood-Hougen-Watson kinetic model with few parameters, meaning all educts must be adsorbed at the catalyst surface, and in this case is the surface reaction limiting the reaction speed and not the diffusion speed in the catalyst pellets. The use of partial pressures over fugacities is a simplification that is often used in literature, as the compressibility factors are reported to be inside the 0.99 to 1.01 range [Bus96]. The equilibrium constants K_{eq1} and K_{eq2} are taken from Graaf et al. [GSB88], and are calculated by the following equations:

$$log_{10}(K_{eq1}) = \frac{3066}{T} - 10.592 \tag{2.21}$$

$$log_{10} \frac{1}{K_{eq2}} == \frac{3066}{T} + 2.029 \tag{2.22}$$

Other kinetic parameter values K_1 to K_5 were parameterized by the following equation (2.23):

$$k_i = A_i exp(-\frac{B(i)}{R}(\frac{1}{T_{av}} - \frac{1}{T})) \tag{2.23}$$

in which T_{av} equals 501.57 K. The parameters are listed in table 2.4.

$K1$ and $K5$ are the rate constants of their respective equations, while $K2 - K4$ represent the equilibrium dynamics of the reaction along with K_{eq1} and K_{eq2}. β is the expression to account for the competitive adsorption and desorption of the different species on the catalyst surface. Validity of the parameters range between temperatures of 453.15 K and 553.15 K, and pressures of 15 bar and 51 bar.
In their work, Mignard et al. [MP08] extended the pressure range covered by their model, along with that of Van Dal et al. [VDB13], to encompass pressures ranging from 15 bar to 75 bar. Despite this expansion, Mignard et al. and Van Dal et al. utilized parameters similar to those used by Bussche et al. However, the specific calculation of these parameters was determined using equation (2.24), as described in their respective studies.

$$k_i = A_i exp(-\frac{B(i)}{RT}) \tag{2.24}$$

Bussche			Van Dal		
K_i		value	K_i		value
K_1	A	7,070.34	K_1	A	1.07
	B	36,696		B	40000
K_2	A	3,453.38	K_2	A	3453.38
	B	-		B	-
K_3	A	30.82	K_3	A	0.499
	B	17,197		B	13,197
K_4	A	558.17	K_4	A	6.62 e-11
	B	124,119		B	124,119
K_5	A	1.65	K_5	A	1.22 e10
	B	-94,765		B	-98,084

Table 2.4: Parameter Values of kinetic equations

Furthermore, both studies used reaction rate equations based on the total catalyst mass. This does include the reduction of the spatial dimensions of the simulated reactor down to a one-dimensional model. To make this possible, the following assumptions and simplifications must be made [MCR11]:

- Negligible radial diffusion: constant temperature and concentration profiles an all directions except the axial direction for both the reactants and the catalyst.
- Negligible axial diffusion: no diffusion along the axis of the reactor.
- Negligible catalyst deactivation during steady state.
- Pseudo-homogeneous and uniform catalytic particles are assumed due to the small size of particles

Figure 2.6 shows the small difference between the calculations of Bussche et al. (b) and Van-Dal et al. (a). The major difference is the behavior in the first 0.03 m of the reactor, which is due to the adjustment made by Mignard et al. [MP08] on the reaction activation energies. [VDB13]
The operating conditions for Bussche and Van-Dal are listed in table 2.5. Both Bussche and Van-Dal use a flow reactor in a loop configuration, to recycle the gases at the reactor outlet. This way the overall yield can be improved, as a lot of the educts have not yet reacted when the equilibrium is reached. The recycle ratio is describing the percentage of outlet gases, that are remixed with the inlet gases and fed back to the reactor.
Slotboom et al. proposed a different kinetic model, while comparing the steady state kinetic models of Graaf et al. [GSB88], Bussche et al. [Bus96], and Seidel et al. [SJV$^+$18]. The model is applicable within the pressure range of 20 to 70 bars and temperatures ranging from 450 to 530 K, although there is a high probability that these boundaries could be extended further.

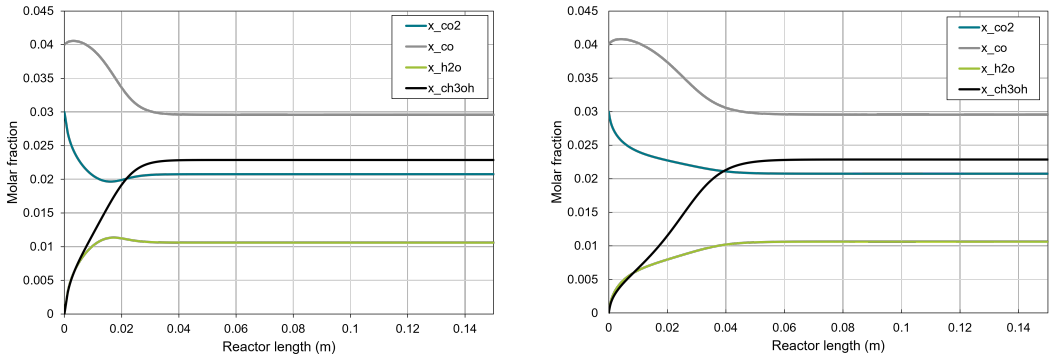

Figure 2.6: Calculated Molar flow rates by Van-Dal (a) and Bussche (b) for similar feed streams.

Operating Conditions		
Catalyst	value	unit
Density	1775	kg/m^3
Porosity	0.5	-
Mass	34.8	g
Pellet diameter	0.0005	m
Reactor		
Diameter	0.016	m
Length	0.15	m
Operating conditions		
T_{inlet}	493.2	K
p_{inlet}	50	bar
mass flow	2.8e-5	kg/s
Feed composition		
CO	4	mol%
H_2O	0	mol%
$MeOH$	0	mol%
H_2	82	mol%
CO_2	3	mol%
$Inert$	11	mol%

Table 2.5: Operating Conditions for the Simulation of the Bench Scale Reactor

Slotboom et al. conducted their own experiments and combined their data with the datasets from Seidel et al. [SJV$^+$18]. All kinetic models mentioned in the paragraph before were compared using a systematic regression method developed for this study. The newly proposed model of Slotboom et al. utilizes only six parameters for its kinetic description and claims to be more robust. However, it is noted that the model currently lacks sufficient discrimination for regression of adsorption terms [SBP$^+$20].

In the work of Nyári et al. [NIT$^+$22], the models of Seidel et al., Slotboom et al., and Van-Dal et al. are thoroughly compared. Standing out are the huge differences in the methanol yields of the three models. At optimal conditions, the yield of the models of Seidel et al., and Slotboom et al. are more than 30% higher than that of Van-Dal et al. or Bussche et al. In that sense, only at low pressures, the Van-Dal model predicts a higher methanol yield than the other two models.

Manenti et al. proposes and compares different steady-state models for methanol synthesis in fixed-bed reactors. The models are divided into three groups: First, a pseudo-homogeneous approach described by means of molar balance in literature. In this group, the decrease in the total amount of moles is neglected, along with the gradient between gas and solid phase. Secondly another pseudo-homogeneous model, based on mass balances rather than molar balances, where the assumption of a constant number of moles along the reactor is removed in order to account for the decrease in the number of moles along the reactor. And lastly a heterogeneous model where both of the assumptions of the first pseudo-homogeneous model are removed, meaning different temperatures for gas phase and catalyst surface, and a decreasing number of moles. It is shown, that especially the neglecting of decreasing mole number has a huge effect on methanol yield, as it is unavoidably underestimated. While the value of the adiabatic temperature is not affected by this assumption, the location of the maximum temperature is altered, up to 14% of the total reactor length. Manenti et al. also investigated the influence of mass flow changes in their work. However, they also include the formation of methanol from carbon monoxide, as well as the formation of CO and H_2 from methane and water in their reactor, making comparisons more complicated. [MCR11]

Jeong et al. [Jeo22] investigated the optimal parametric framework for methanol production in a loped packed bed reactor using the kinetic model provided by Bussche et al. [Bus96]. Optimized were the gas inlet and reactor wall temperature, the recycle ratio and the hydrogen to carbon dioxide ratio prior to the mixing with the recycle stream. This was realized through incorporating neural network techniques. The optimized results under their parameter boundary set were found with a recycle ratio of 0.9 and a hydrogen to carbon dioxide ratio of 5, with the temperature of the inlet between 480-486 K and the reactor wall temperature of 509.76-516.63 K. As this study only offered a technological viewpoint, the higher price for hydrogen was not considered. [Jeo22]

Matthischke et al. investigate the startup time and load range of fixed-bed reactors for an exothermal CO_2 methanation. They report that the time to reach steady state

in adiabatic plug flow reactors is longer compared to cooled reactors. This difference is primarily attributed to the vastly different temperature profiles of the reactors, which is influenced significantly by the thermal capacity of the reactor wall. The temperature peaks in both reactors differ by approximately 400K, and the cooled reactor reaches a steady state after 197 seconds due to these thermal dynamics. [MRG18] However, the difference of the temperature peaks for the synthesis of methanol is about a magnitude smaller, which would lead to shorter startup times if the other parameters remain unchanged. [MRG18]

2.3 Methanol Distillation

Distillation is the most prominent purification process for volatile liquids, and the most frequently used separation operation in the chemical industry [BAJV16]. In separating different components of a mixture into liquid and vapor phases, the more volatile substance can be selectively separated from the less volatile one. This separation is typically achieved by leveraging significant differences in the boiling temperatures of the pure components, leading to distinct fugacities in the vapor and liquid phases. This section is focusing on the theoretical framework of the vapor-liquid-equilibrium of methanol and water, the fundamental process of rectification, the molar flow balances inside the distillation column and the startup of distillation columns.

2.3.1 Vapor Liquid Equilibrium

For technical distillations, it is important to be able to calculate the vapor-liquid-equilibrium (VLE). In the McCabe-Thiele diagram in figure 2.7, the red line shows the vapor concentration of methanol in water plotted against the concentration of methanol in the liquid.

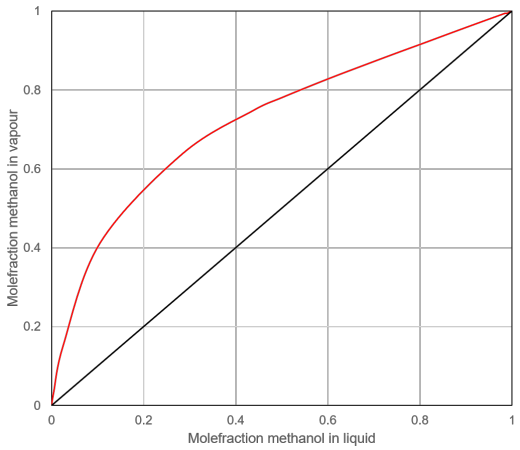

Figure 2.7: vapor-Liquid equilibrium methanol water

For ideal mixtures this curve is described by the term of relative fugacity α, also called separation factor 2.25:

$$\alpha = (y_A/x_A)/(y_B/x_B) \tag{2.25}$$

where:

- y_i is the concentration of component i in the vapor phase,
- x_i is the concentration of component i in the liquid phase.

In ideal vapor-liquid systems, the interactions between all molecules are the same regardless of their type. In this scenario, Raoult's law 2.26 applies, meaning the partial vapor pressure p_i of substance i corresponds to the saturation vapor pressure of the pure substance P_{0i} multiplied by the mole fraction x_i in the liquid phase. The separation factor can be described by equation 2.27, and its influenced by changes in the concentration.
In the context of Figure 2.7, if Raoult's law holds true, the red line depicting the vapor concentration of methanol in water would form a symmetrical hyperbola. When two substances are challenging to separate, the equilibrium curve on the plot tends to lie close to the diagonal line, indicating similar vapor-liquid equilibrium behaviors of the components in the mixture [BAJV16].

$$p_i = P_{0i} \cdot x_i \tag{2.26}$$

$$\alpha = P_{0A}/P_{0B} \tag{2.27}$$

For real systems, an activity coefficient γ_i can be added to the Raoult's law, to correct for asymmetrical, or even azeotropic behavior .

$$p_i = P_{0i} \cdot \gamma_i \cdot x_i \tag{2.28}$$

$$\alpha = (\gamma_A \cdot P_{0A})/(\gamma_B \cdot P_{0B}) \tag{2.29}$$

For the calculation of the activity coefficients multiple models are available, the most prominent ones being the Wilson Model, Van-Laar Model, Margules Model and the Non-Random Two-Liquid (NTRL) Model [JS19], summarized in table 2.6. Nitsche [Nit14] also mentions the same models under methods for strongly non ideal behavior in the liquid phase. Each of these models have some advantages and disadvantages over the other, as explained in the following paragraphs.
Nitsche et al. [Nit14] also mentions other models to calculate the VLE, like the Chao-Seader Method and Grayson-Streed Method for non-ideal behavior in the liquid phase, and the UNIQUAC (Universal Quasi-Chemical) Method, for strongly non ideal behavior in the liquid phase.
In this work, the Margules model was chosen for its capability to describe extrema in activity coefficients. However, as noted by Jain et al., the differences between the models are marginal for methanol-water distillation [JS19]. Calculation of the coefficients is done using equations 2.30 and equation 2.31.

$$\gamma_1 = exp((A_{12} + 2 \cdot (A_{21} - A_{12}) \cdot x_1)x_2^2) \tag{2.30}$$

$$\gamma_2 = exp((A_{21} + 2 \cdot (A_{12} - A_{21}) \cdot x_2)x_1^2) \tag{2.31}$$

The optimal use of distillative separation possibilities is achieved with rectification. It corresponds to a continuous distillation carried out multiple times in succession for improved separation. Unlike individual distillations, it eliminates the need for

Model	Description	Advantages	Limitations
Wilson Model	- Accurate for modeling liquid phase in vapor-liquid equilibrium (VLE) of completely miscible mixtures or cases with one liquid phase. - Calculates activity coefficients based on mole fractions and interaction parameters.	- Suitable for fully miscible systems or single-phase mixtures. - Provides accurate modeling for specific scenarios.	- Cannot model liquid-liquid equilibria.
Van-Laar Model	- Derived from Van der Waals equation, but adjusted with experimental results for practical use. - Helps in correlating experimental results of VLE. - Provides equations for calculating activity coefficients.	- Useful for correlating experimental VLE results.	- Limited by its empirical nature.
NRTL Model	- Based on Wilson's hypothesis that local concentration around a molecule differs from bulk concentration. - Accounts for non-randomness in the liquid phase. - Widely used for calculating phase equilibria and activity coefficients.	- Accurately accounts for non-randomness in liquid phases. - Provides reliable phase equilibria calculations.	- Requires interaction parameters and other data, which can be complex.
Margules Model	- Introduced in 1895. - Describes excess Gibbs free energy of a liquid mixture. - Uses coefficients reflecting interaction between components to calculate activity coefficients.	- Can predict extremities in activity coefficients that other models might miss.	- Limited in scope and may not capture all complexities.

Table 2.6: Models to determine activity coefficients [JS19]

complete condensation of the vapor and its re-evaporation in the next stage; instead, the vapor is directly introduced into the liquid of the next stage. As a result, the more volatile components increasingly vaporize from the bottom to the top of the column, eventually leaving the column at the top as distillate. On the other side, more heavy volatile components condense from top to bottom, until they reach the column base, where they leave the column at last. The feed-stream is to be injected into the stage in which the concentration equals or closely resembles that of the feed-stream. [BAJV16]

2.3.2 McCabe-Thiele-Method

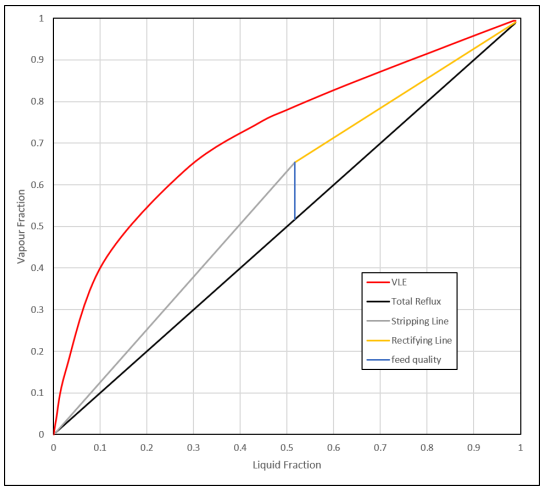

Figure 2.8: McCabe-Thiele Operating Lines for $x_F = 0.52$, $q = 1$ and $v = 1.2$

The McCabe-Thiele-method (MTM) is a graphical technique used in chemical engineering to determine the number of theoretical stages required for a distillation process. This method simplifies the design and analysis of binary distillation columns. The McCabe-Thiele method is based on several assumptions for simplicity and ease of use[Nit14]:

- The distillation operates at steady state.
- The system pressure remains constant.
- The molar vaporization enthalpies of the fluids are consistent throughout the process.
- The molar overflow, which represents the ratio of liquid to vapor flows in the column, is constant, with variations allowed between the rectification and stripping sections of the column.

Despite these simplifications, the McCabe-Thiele method provides a useful approach in the design and analysis of distillation columns for binary mixtures.

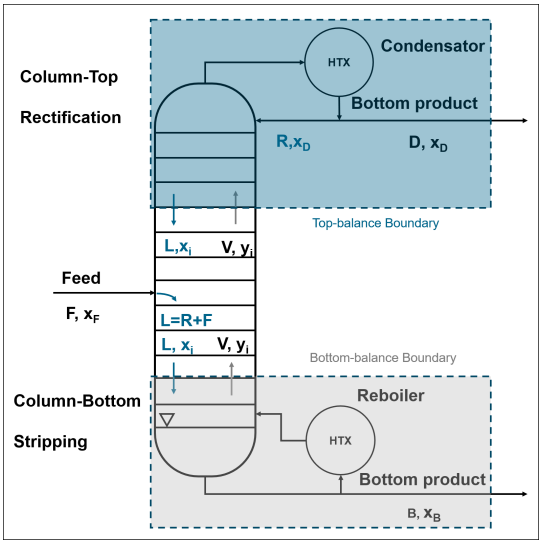

Figure 2.9: Material Balance for the analytical McCabe-Thiele-Method (q=1)

The basis of the MTM is the material balance according to figure 2.9. During steady operation, the sum of the product molar flows at the Top D and at the Bottom B are equal to the molar flow of the feed F. This is true for the total molar flows, as well as the partial flows:

$$F = D + B$$
$$F \cdot x_F = D \cdot x_D + B \cdot x_B$$

Apart from the overall material balance, smaller boundaries can be chosen, for example for q = 1 around the rectification part of the distiller in 2.3.2 according to 2.9:

$$V = D + L \quad with \quad L = R + F$$
$$v = L/D$$
$$V \cdot y_i = D \cdot x_D + L \cdot x_i$$

The material balance for the stripping part of the distiller is thus be described by:

$$L = R + F$$
$$V = L - B$$
$$V \cdot y_i = L \cdot x_i - B \cdot x_B$$

All these equations can be used to construct the rectifying line 2.32 [BAJV16]:

$$y = \frac{x_D}{v+1} + \frac{v}{v+1} \cdot x \tag{2.32}$$

Where:

- V is the amount of vapor,
- L is the amount of liquid in the downcomer,
- y_i is the concentration of component i in the vapor,
- x_i is the concentration of component i in the liquid,
- v is the reflux ratio.

In figure 2.8 this was done for a Methanol-Water Rectification, with a feed molar fraction x_F of 0.5, a feed quality q of 1 and a reflux ratio v of 1.2.
The key elements of the diagram include:

1. **Equilibrium Curve**(red): Shows the equilibrium relationship between the liquid and vapor phases of the mixture. The curve's shape depends on the specific properties of the components being separated.
2. **Operating Lines**: Represent the material balances around the rectifying and stripping sections of the distillation column. The rectifying line(yellow) is used for the section above the feed tray, and the stripping line(gray) is used for the section below.
3. **Feed Line**(blue): Depicts the condition of the feed entering the column, whether it is a liquid, vapor, or a mixture of both (saturated liquid, saturated vapor, or sub-cooled liquid).

The minimum re-flux ratio, which would lead to an infinite number of steps in the diagram, would be determined graphically by the intersection of the operating lines and the equilibrium curve or using equation 2.32.
In the industry, the ratio between distillate flow, feed flow and bottom flow is already determined by the desired concentrations, meaning the minimum number of stages is set. The reflux ratio plays a significant role in influencing the behavior of a distillation column. It impacts various aspects of the column's operation and design, including: total number of stages, dimension of the condenser, dimension of the reboiler, operating costs and capital costs. For this reason, the reflux ratio is an important parameter that has to be optimized in an economic analysis. A common rule of thumb in distillation design is to use a reflux ratio that is approximately 1.1-1.3 times the minimum reflux ratio required for the desired separation. [BAJV16]

In Figure 2.8, if the feed is not a liquid at its boiling temperature (represented by q $\neq$ 1), the feed line on the diagram will exhibit specific characteristics:

- For sub-cooled liquids (q $<$ 1), where the feed temperature is below its boiling point at the column pressure, the feed line will have a positive slope.
- Conversely, if the feed contains vapor (q $>$ 1), where the feed temperature is above its boiling point at the column pressure, the feed line will have a negative slope.

Variations in the feed condition, whether sub-cooled liquid or containing vapor, not only impact the number of stages required in the distillation column but also affect the distribution of liquid and vapor quantities within the rectification and stripping sections of the distiller. Changes in flow rates due to different feed conditions influence the duties of the reboiler and condenser, resulting in altered energy balances for these components

2.3.3 Startup simulation

Simulation of distillation columns under steady-state conditions is well-captured by equilibrium models in literature and widely used chemical software like CHEMCAD®or Aspen®. However, broadly applicable models for cold startup scenarios are currently limited. As the equilibrium models lead to large-scale differential algebraic equation systems with dynamic behavior, the initialization of the system is not trivial. This is why in most software a pseudo warm state is chosen as an initial condition. [WLWW03] The startup dynamics of distillation columns are only relevant indirectly for this work, as there is a big uncertainty of the duration of the startup process.
In their work, Wang et al. introduced a model to describe the startup process of batch distillation columns starting from a cold and empty stage. Mainly, this model was developed to optimize the control during startup processes. The model predicts the transition states of trays within the column during startup, distinguishing between the empty (EM), liquid accumulation (LA), and vapor-liquid equilibrium (VLE) states, while capturing the dynamics temperature rises in each tray. The startup process begins with heating the re-boiler until vapor generation starts, causing trays to transition from EM to LA as vapor condenses on them. This transition continues until trays reach the VLE state, indicating the start of effective separation processes. The total startup time ranges from t=2.8-3.8 hours when filling the column from the bottom up. This process involves evaporating all the liquid by the reboiler and condensing it in the trays and the condenser. Simulation results from the model are compared with experimental data from a pilot plant, showing good agreement in temperature profiles across various trays during the startup.[WLWW03]
Eden et al. introduces a systematic procedure for developing startup sequences for plants, focusing on an energy-integrated distillation plant. It highlights the complexity and non-linearity involved in starting up distillation columns. Eden et al. suggest,

basing the generation of startup procedures on qualitative process knowledge rather than detailed simulation models, due to unusual operating conditions and lack of parameter correlations during startup-processes. The startup operation is divided into three phases: discontinuous, semi-continuous, and continuous. The semi-continuous phase is critical for achieving steady state values and managing disturbances.
The systematic approach that is presented, emphasizes the identification of plant capacities and suitable sequences to fill these capacities. It particularly addresses the challenges posed by process integration, such as energy recycle, on startup sequences.
Eden et al. divide the startup into five phases, each with their own starting indicator. The phases are described in table2.7:

	Purpose	**Initiating action**	**Indicator**
I	Heat condenser system	Feed steam to preheater	OK for startup
II	Heat reboiler and heat pump	Start compressors	Condenser warm
III	Stop startup energy source, establish desired purities	Shut off help energy	Vapor flow OK
IV	Bring process into desired-operating form	Set desired setpoints in-low level controls	Purities acceptable
V	Introduce supervisory control	Selected setpoints specified-by higher algorithm	

Table 2.7: Phase definitions for startup of energy integrated distillation columns acc. to [EKHJ00]

The application of the procedure is demonstrated at an energy-integrated distillation plant. [EKHJ00]
Neves et al. [NAM99] deliver a qualitative control approach for a distillation startup with the ability to supervise a production plant via quantified actions. Using their approach a stable operation of the distillation startup and shutdown was possible, while also reacting to changes of feed concentration. The parameters and the dimensions of the column used are displayed in table 2.8. [NAM99]
To implement the control system, Neves et al. divided the startup process into six phases, also shown in figure 2.10:

1. Establish a liquid level of 30% in the reboiler.
2. Heat the column to purge inert gases.
3. Complete the purging of the column.
4. Obtain a bottom concentration of less than 2% methanol or
5. Achieve a top product concentration of more than 98% methanol.
6. Reach steady state flows and levels.

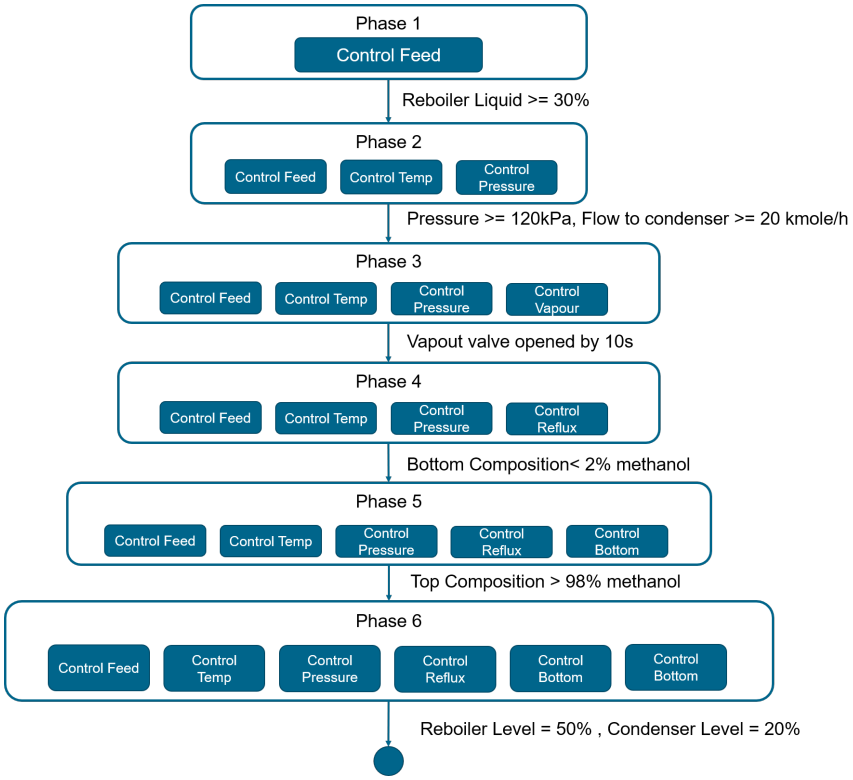

Figure 2.10: Startup procedure, controls and conditions of Neves et al. [NAM99] and Fabro et al. [FAN05]

Parameter	value	unit
Reboiler Volume	0.5	m^3
Condenser Volume	1.43	m^3
Tray Volume	0.04	m^3
Methanol inflow	2721.45	kg/h
	0.0756	kg/s
Water inflow	2721.45	kg/h
	0.0756	kg/s
Feed temperature	75.9	°C
Feed pressure	110	kPa
Top concentration	99.9	% Methanol
Bottom concentration	0.01	% Methanol
Reflux Flow	7890	kg/h
	2.191	kg/s
Reflux Ratio	0.7416	

Table 2.8: Distiller parameters of Neves et al. [NAM99] and Fabro et al. [FAN05]

2.4 Full Scale Plants

Many studies include a methanol synthesis plant that includes additional units such as hydrogen production, distillation, or both, alongside the reactor.
A very detailed system description was presented by Pérez-Fortes et al. [PFSBT16]. It is a techno-economic analysis of a methanol-production plant, focusing on the synthesis, while also briefly considering the distillation of products. The reactor simulation is conducted using CHEMCAD®, with CO2 and hydrogen supplied via pipelines, thereby excluding the use of electrolyzers in the system. With the proposed dimensions, the plant is capable of producing about 440 kilotons of methanol per year, with a nominal hydrogen load of 11 t/h and a CO2 load of 80.5 t/h. Despite the environmental benefits, the analysis of Pérez-Fortes et al. shows that the project was not financially attractive due to high production costs primarily attributed to expensive raw materials such as hydrogen and CO2. However, the capital costs of the plant were found to be lower than those of conventional plants. With increasing prices for methanol, and decreasing prices for CO2 and hydrogen, this might change in the future. [PFSBT16]
The plant analyzed by Van-Dal et al. utilizes captured CO2 from flue gases of a coal power plant, while providing the carbon-free hydrogen through electrolysis. For the simulation and process design, the software Aspen Plus®was used, with similar dimensions as the Pérez-Fortes plant. Both plants are compared in table 2.9.

Variable	**Van-Dal**	**Pérez-Fortes**	**unit**
CO_2 Feed	88	80.5	t/h
CO_2 out	5.82	3.825	t/h
H_2 Feed	12.1 (from water feed)	11	t/h
H_2 out	0.87	0.51	t/h
catalyst mass	44.5	44.5	t
Water Feed	108.1	-	t/h
Water out	33.7	36.39	t/h
Methanol out	59.3	55.1	t/h
O_2	96	-	t/h
Power Electrolysis	645.1	-	MW_{el}
Power Synthesis	21.5	17.36	MW_{el}
Thermal Energy	49.4	24.19	MW_{th}
Cooling needs	-	47.5	MW_{th}

Table 2.9: Comparison between the methanol synthesis plants of Van-Dal et al. and Pérez-Fortes et al., regarding global energy and mass balances. [VDB13] [PFSBT16]

The hydrogen production process in this plant consumes up to 97% of net electricity used by the entire facility. As 36% of thermal energy for the carbon-capture unit of the plant is supplied by the methanol synthesis, rather than the coal power plant, the CO2 abatement of the plant is further increased. The CO2 balance analysis reveals that the proposed process could potentially abate 1.6 tonnes of CO2 per tonne of

produced methanol if the oxygen by-product is sold, or 1.2 tonnes if it is not sold. In the latter case, the oxygen is fed back into the power plant for oxy-combustion to increase the CO2 concentration in the flue gases. In both cases, the hydrogen for the process must be produced using carbon-free electricity. If only 20% of the electricity for the hydrogen production is supplied by the coal plant, the CO2 balance is null. Van-Dal et al. provide a detailed technological analysis of the process and highlight the potential importance of it in the abatement of CO2, however they did not include an economic analysis in their work. [VDB13]

One study on the technical and economic aspects of small-scale methanol plant was presented by Mignard et al. [MP08]. Here, a hybrid process that uses biomass and electrolysis was considered, addressing the critical issue of transportation by transferring the production of bio-fuels to locations where renewable energies are available and biomass production is existing. They found that part-load or variable load of fixed bed reactors is feasible without experiencing hot spots in the reactor or surges in by-product formation. The price of electricity was identified as the most sensitive factor to affect the economics, making the partial load operation during high price periods important.

Moioli et al. investigated another approach on the technical and economic viability of small-scale methanol production configurations. These configurations are designed to adapt to intermittent hydrogen availability and avoid energy-intensive compression stages, with a focus on decentralized production for energy storage. The methanol process is limited to a pressure of 30 bar, the standard hydrogen delivery pressure from an electrolyzer. This saves the high costs and complexity of hydrogen compression at a small scale. The research explores various configurations that differ in their strategy for valorizing the unreacted gas stream, including the potential coupling with other processes such as bio-gas upgrading. The economic analysis reveals that profitable methanol production from renewable hydrogen is not feasible at high electricity prices due to the significant impact on hydrogen cost. The highest electricity price that allows for profitable operation was found to be 0.07$/kWh for the recycling process. However, when methanol production is combined with bio-gas upgrading, the process can operate economicly in a cascade configuration, demonstrating that small-scale methanol production is feasible only under specific conditions such as consistent low electricity prices or integration with waste-handling facilities. [MWS22]

3 Methodology

In this chapter, we delve into the implementation of the different components, commencing with an overview of the simulation tool employed for this work: YACOP. Subsequently, we provide a system overview of the entire methanol synthesis plant. Here, we elucidate the simplifications and alterations made to the models presented in literature. We then proceed to describe the components of the system, detailing their functionality and modeling.
Following the comprehensive overview of the entire methanol synthesis plant, we proceed to introduce the model of the alkaline electrolyzer and the electrolyzer system. Next, we present the methanol synthesis subsystem, which was constructed around the reactor model to streamline the workflow of integrating the reactor into existing subsystems. Subsequently, we discuss the limitations of the reactor implementations. Finally, we showcase the model of the distillation column, with a special emphasis on the incorporated startup calculation.

3.1 YACOP

YACOP stands for Yield Assessment Calculation and Optimization Program. This Python-based tool, developed by DLR, is designed to simulate utility-scale energy production and conversion systems. YACOP prioritizes high modularity and modeling flexibility, achieved through a combination of features such as a generic simulation engine, a library of tools and physical components library, an application library and a data library.
Figure 3.1 illustrates the structure of YACOP's simulation engine.
In summary, YACOP utilizes a common time series calculator to manage the import the inputs and parameters, as well as the distribution, collection, and export of results, and post processing. This calculator also invokes the time step solver for each time step, which resides within the System Level. At this level, subsystems and the interconnections, along with the control strategy, are defined. Subsystems are treated as black boxes with generic base structure, interacting with each other solely through predefined interfaces or control attributes. This design fosters YACOP's interchangeability of Subsystems and flexibility in modeling. Subsystems can be modeled using algebraic equations, data driven models (such as performance maps), or even external tools. Moreover, combinations of data driven models and algebraic models are supported. Interfaces encompass fluid-flow, electric-flow and heat-flow interfaces, while common attribute types include parameters, inputs, controls, results or previous-news, a custom attribute class enabling access the attribute's last value.

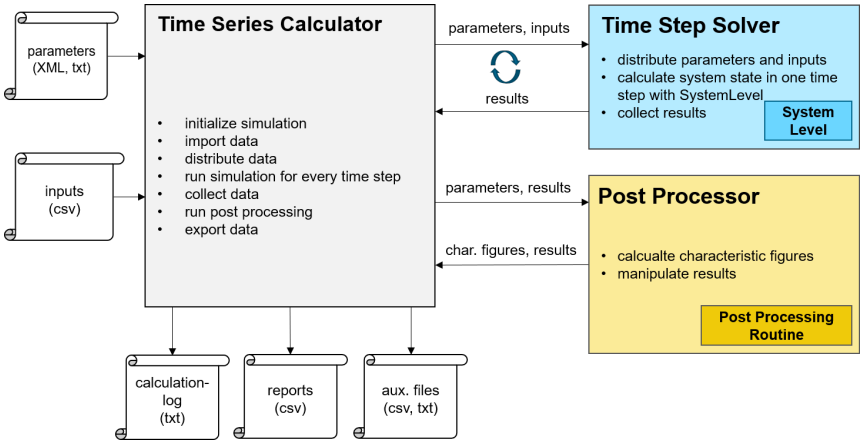

Figure 3.1: Overview of YACOPs Simulation Engine

The models already implemented in YACOP primarily relate to components of concentrated solar power plants such as parabolic trough fields, photovoltaic systems, battery energy storages heat storages, and power blocks for electricity generation, but also heat pumps, heaters, heat exchangers. The latter are also relevant for the integration of the components that have been developed in this work, as some of them are used in the newly implemented systems.
One very interesting feature of YACOP is its capability to divide time steps, allowing for precise calculation of components behavior when their states change within a time step. For example, this feature enables accurate modeling of scenarios such as the complete filling or emptying of a tank or storage unit within a single time step.

3.2 Methanol Production System

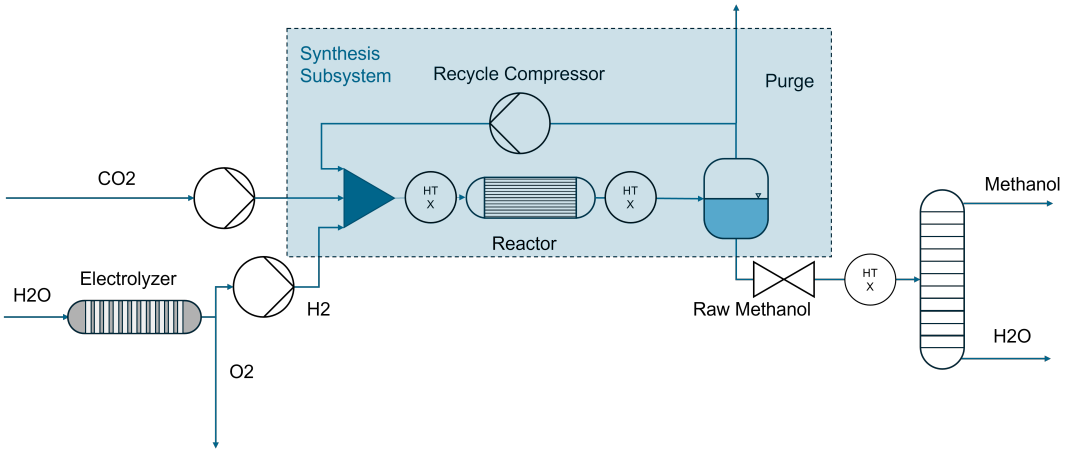

Figure 3.2: Synthesis system around the methanol reactor, including implemented heat-exchangers (HTX), inlet compressors for hydrogen and CO_2, a recycle compressor, a separator and a distiller

This section describes the methanol synthesis on a system level, explaining the interrelations between the components so that the functionalities of the singular units are easier to understand. Additionally, the heat-transfer-fluid- and the compressor-class are explained in this section.
For this study, we have selected a simple yet comprehensive aggregation of components required to produce methanol from water and CO_2, as shown in figure 3.2. Compared to the systems proposed by Van-Dal et al. [VDB13] and Pérez-Fortes et al. [PFSBT16], the main differences lie in the inclusion of complex heat-exchange networks. In this work, these networks are simplified through global heat balances. Additionally, in the case of Pérez-Fortes et al., the system utilizes a purge stream in a furnace to harness excess hydrogen for generating steam and electricity, along with integrating additional flue gases.
As depicted in figure 3.2, the process begins with water being fed into the electrolyzer, where it is converted into hydrogen based on the hydrogen requirements or available electric power. The hydrogen produced by the electrolyzer, at a pressure of 30 bars, is further compressed to reach the reactor inlet pressure of 75 bar. Meanwhile, the oxygen produced by the electrolyzer is not utilized further in the system.
Simultaneously, CO_2 is introduced into the system and compressed to the reactor pressure, in accordance with the chosen $H_2 : CO_2$ ratio. Both the hydrogen and CO_2 streams are then directed into the synthesis subsystem, as described in section 3.4. Within this subsystem, CO_2 and H_2 undergo conversion to form raw methanol, which still contains water.
The raw methanol exiting the Synthesis Subsystem is depressurized and then fed into the distillation column. Upon heating to its boiling temperature, the methanol is separated from the water, with each component exiting the distillation column at

different ends.
When integrating the components into a complete system, the structure resembles that of works by Van-Dal et al. [VDB13] or Pérez-Fortes et al. [PFSBT16] with the addition of an electrolyzer for hydrogen production. However, the complex heat-exchange network is considerably simplified by utilizing heat-exchange interfaces with temperature ports, enabling the determination of heating and cooling duties globally. Although this approach overlooks the essential aspect of pinch analysis, it still allows for the determination and comparison of heating and cooling duties with relative ease when compared to literature values.
In this study, only the functionality of the components is assessed, which is why a simple operating strategy for the system is chosen. The hydrogen demand of the reactor serves as the central control value, upon which the operation of the other components depend. The inflow of carbon dioxide inflow is directly proportional to the inflow of hydrogen, as well as the inflow of water into the electrolyzer system, as indicated in table 3.1. When the load is adjusted, all three of these values are uniformly varied, while the recycling stream within the synthesis system is adjusted based on the newly calculated reactor outlet flows.

Inflow Conditions in steady state

Parameter	**value**	**unit**
H_2O inflow electrolyzer system	27.42	kg/s
H_2 inflow system	3.05	kg/s
CO_2 inflow system	22.36	kg/s
Recycling stream	ca. 100	kg/s

Table 3.1: Synthesis system and electrolyzer system inflows at steady state.

3.2.1 Heat Transfer Fluids

Up to now, the YACOP-class for heat-transfer-fluids (HTFs) has predominantly been utilized for fluids employed in solar plants, such as thermo-oils or -salts. These were primarily accessed for their heat capacities or temperature limitations. Among these HTFs, water had a more sophisticated representation, encompassing properties like saturation temperatures or varying heat capacities. The relevant information for these HTFs is typically stored in isobaric tables, from which properties are read or interpolated as needed.
Using the structure of the water HTF, more chemicals were introduced to be able to accurately calculate fluid properties in the reactor and the methanol distiller. When the pressure and temperature of the HTF is set from the outside, properties like enthalpy, entropy, thermal conductivity and saturation temperature can be accessed. Given that most of the components in YACOP only provide a single fluid interface for both inflow and outflow, a new HTF was introduced. This HTF known as *Mixture* was introduced to compute the properties of fluid mixtures. This was done to prevent

the need for creating of multiple components at the system level, where only a single fluid flow is actually present. The fluid properties are then calculated as followed:

1. Temperature, pressure and molar concentrations are set through the system level.
2. partial pressures are calculated within the mixture.
3. component properties are calculated.
4. mixture properties are calculated from the component properties and molar fractions.

3.2.2 Compressor

Additionally, since YACOP's library did not include a compressor model, a compressor with isentropic efficiency was implemented to accurately represent a complete synthesis plant.
The isentropic efficiency of a compressor ($\eta_{\text{isentropic}}$) is defined as the ratio of the work input required for an ideal (isentropic) compression process to the actual work input required for the real (non-isentropic) compression process. In terms of enthalpy, the formula can be expressed as follows:

$$\eta_{\text{isentropic}} = \frac{h_{2s} - h_1}{h_2 - h_1} \tag{3.1}$$

where:

- h_1 is the enthalpy at the compressor inlet.,
- h_2 is the actual enthalpy at the compressor outlet,
- h_{2s} is the enthalpy at the compressor outlet for an isentropic process (ideal).

This equation assumes that the compressor operates at steady state and that the work is primarily due to changes in enthalpy.
Moreover, a heat flow interface was integrated to the compressor model, to calculate a cooling duty of the outflow gases if required. The structure of the compressor interfaces is shown in figure 3.3. When the outlet temperature does not surpass the predetermined maximum temperature, the interface remains idle. However, if the outlet temperature exceeds this threshold, the cooling duty is calculated using equation 3.2:

$$\dot{Q_{cooling}} = \dot{m} \cdot (h_{out} - h_{desired}) \tag{3.2}$$

where:

- $\dot{m}$ is the mass flow through the compressor,
- h_{out} is the fluid enthalpy at exit temperature,
- $h_{desired}$ is the fluid enthalpy at the desired outlet temperature.

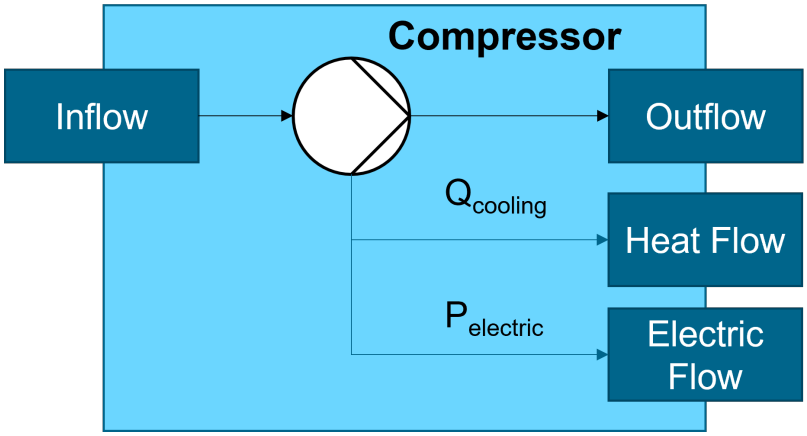

Figure 3.3: Structure of the compressor component in YACOP, with In- and Outflow, heat and electrical interface.

3.3 Alkaline Electrolyzer

In this section, the underlying equations of the alkaline electrolyzer and the electrolyzer system are explained in detail. The model of the alkaline electrolyzer adopts a quasi-steady-state algebraic approach, implementing the equations described in section 2.1 are implemented. While a data driven electrolyzer model was also considered to enhance computation time, it was ultimately disregarded, as such a model would only be valid for a certain parameter set. Given the typical time steps employed in the simulation, which are sufficiently long, the quasi-steady state behavior is assumed. The energy balance that was implemented resembles the quasi-steady state thermal model expressed by Ulleberg [Ull03]:

$$T = T_{int} + \frac{\Delta T}{C_t} \cdot (\dot{Q}_{gen} - \dot{Q}_{loss} - \dot{Q}_{cool}) \tag{3.3}$$

where:

- T is the temperature after the time step,
- T_{int} is the temperature before the time step,
- ΔT is the duration of the time step,
- $\dot{Q}_{gen}$ is the generated heat,
- $\dot{Q}_{loss}$ is the heat loss to the environment,
- $\dot{Q}_{cool}$ is amount of heat that is purged by cooling.

According to the current hydrogen production, $\dot{Q}_{gen}$ is calculated. For this, the current density, the cell voltage, the thermoneutral voltage and the faradaic efficiency have to be calculated. However, these variables are all temperature-dependent, presenting a challenge for straightforward calculation. While an iterative approach is feasible, it would substantially prolong computation times. To circumvent this, a constant faradaic efficiency was adopted to estimate the current density, from which the cell voltage is derived. Additionally, a temperature estimation is required at this point. The temperature rise ΔT per hour was introduced as a parameter to ensure the electrolyzer's temperature ascends steadily but not too rapidly, until it reaches a steady-state temperature. If the heat generated within the electrolyzer is insufficient to induce this temperature increase, the actual temperature rise is calculated subsequently. In both cases, the assumed temperature is calculated by the following equation:

$$T = T_{start} + 0.5 \cdot T_{rise} \tag{3.4}$$

The temperature estimation and calculation of the cooling duty are depending on the electrolyzer state and operating mode. The scheme to determine the temperature and the cooling duty is summarized in the list below:

- *Idle*: If the electrolyzer is not producing, cooling is not necessary and only the heat-loss to the environment is calculated.
- *Heating*: If the electrolyzer is producing, but the heat generated in the time step is not large enough for the system to reach the desired, steady state temperature of the reactor, cooling is still not necessary, as a higher temperature leads to higher efficiencies, given that the temperature rise is noncritical.
- *Operating*: Otherwise, if the desired temperature is reached, the cooling amount will be the excess heat generated in the system, which is not dissipated to the environment.

Contrary to Ulleberg et al., the cooling amount was not calculated from the mass flow of the cooling water, but is a result of the temperature development in the electrolyzer. This may lead to a slight variation of the cooling duty in the here implemented case, as the temperature rise might be overestimated during the heat up phase. Additionally, if the temperature is actually lower, the efficiency is lower as well, meaning the amount of electricity is underestimated.
The heat-loss to the environment $\dot{Q}_{loss}$ is calculated by a combination of heat-loss due to convection $\dot{Q}_{conv}$ and radiation $\dot{Q}_{rad}$:

$$\dot{Q}_{loss} = \dot{Q}_{conv} + \dot{Q}_{rad} \tag{3.5}$$

$$\dot{Q}_{conv} = \alpha \cdot (T - T_{amb})^{1.25} \cdot A_{stack} \tag{3.6}$$

$$\dot{Q}_{rad} = \epsilon \cdot \sigma \cdot (T^4 - T_{amb}^4) \cdot A_{stack} \tag{3.7}$$

where:

- α is the overall convective heat transfer coefficient,
- T is the stack temperature,
- T_{amb} is the ambient temperature,
- A_{stack} is the relevant stack area for heat-loss,
- ϵ is the emissivity of the stack surface,
- σ is the Boltzmann constant.

The production capacity of an electrolyzer stack is limited by the maximum cell area and the maximum number of cells. As an increasing number of cells result in a rise in shunt currents through the KOH solution, the overall voltage efficiency is decreasing. [HZA+24]. Additionally, as more gas bubbles are produced between the

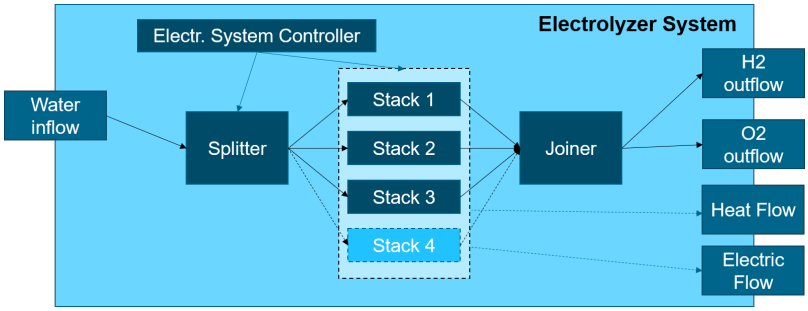

Figure 3.4: Electrolyzer system with stacks, joiner, splitter , system controller and interfaces

electrodes that limit the contact area of the electrolyte and the electrodes. [HZA+24]. As simple up-scaling of a single electrolyzer stack becomes impractical beyond a certain threshold, the implemented electrolyzer system functions as a subsystem with a variable number of electrolyzer stacks. A schematic of the electrolyzer system is shown in figure 3.4. The system incorporates electric, heat and fluid flow interfaces for water, hydrogen and oxygen, facilitating connectivity between the Subsystem and the System Level. Additionally, flow-joiner and a flow-splitter classes were introduced to manage the distribution and collection of the different flows to and from the stacks within the electrolyzer system.

Unfortunately, due to the architecture of YACOP, subsystems are initialized before systems. Consequently, parameters such as the number of stacks in the electrolyzer system are not initialized when the electrolyzer stacks are initialized. As a workaround, the stacks had to be initialized manually in the beginning of the time series calculation within the *init_values* function. Similarly, this applies to the splitter and joiner, as the number of flow connectors must be specified during the initialization.

Additionally to the temperature state, each stack was also implemented with a startup time parameter. There are multiple approaches and also different statements regarding the startup time and whether production is possible during startup. Seibel et al. [SK18] in 2018 mention that 50 % load can be achieved within minutes, whereas Bertuccioli et al. [LADF14] cite multiple electrolyzer producers in reporting that the stacks need a minimum of 20 minutes to reach minimal load, typically around 30%. In YACOP, the startup behavior of Seibel et al. [SK18] was considered. This means that if the operating time of the stack is lower or equal to the startup time, the electrolyzer is only capable of handling 50 % of its nominal load. Given the relatively large time steps in the simulation, a modification of the startup time parameter could also mimic the behavior according to Bertuccioli et al. [LADF14]. By doubling the startup time t_s to t_{s_2}, the period of the load restriction is doubled, and on average, the stack now delivers 0% load during t_s and 100% from t_s to t_{s_2}. This behavior is taken into account by the electrolyzer system controller.

The load of the electrolyzer system is either determined by the hydrogen demand or the available power at the electric flow interface. In the first case, it is calculated from

the water inflow, with the assumption that the complete inflow shall be converted to hydrogen and oxygen. If the total inflow exceeds the maximum load of the stacks, the water is redirected to the water outflow interface. The function distributing the water flow to the individual electrolyzer stacks is attached in the appendix at 6.1. In reality the electrolyzer inflow would not be exceeding the maximum load, but this behavior bypasses the need for an additional time step calculation initiated by the controller.

3.4 Methanol Synthesis

In this section, we further explore the literature and structure of the implemented methanol reactor. The modeling of the synthesis is derived from the works of Bussche et al. [Bus96] and Mignard et al. [MP08], with additional details on the kinetic parameters provided by Van-Dal et al. [VDB13]. These models are based on kinetics derived from the catalyst mass rather than the reactor volume. Consequently, the parameter for the total catalyst mass takes precedence over parameters such as reactor volume, catalyst density, bed porosity and more.
While other kinetic models need fewer parameters, such as the often-cited model proposed by Slotboom et al. [SBP+20], the Van-Dal model was chosen, as the data-set of the Slotboom model is not yet discriminating enough for regression of adsorption terms. Conversely, the model proposed by Seidel et al. [SJV+18] focuses on the simulation of dynamic behavior under varying feed conditions, particularly emphasizing catalyst dynamics. However, given the time step size in the yield calculation ranging from 15 to 60 minutes, prioritizing an accurate representation of the steady-state was chosen to be more important. [NIT+22]
Despite all this, the large difference in the yield prediction should be kept in mind, especially when a techno-economic analysis is performed.

Using the equations from chapter 2, the material balances for each component in steady state can be expressed by the following reaction rates [LZF19]:

$$\begin{aligned}
\frac{dF_{CH3OH}}{dw} &= r_{CH_3OH} = r_1 \\
\frac{dF_{H2O}}{dw} &= r_{H2O} = r_1 + r_2 \\
\frac{dF_{CO2}}{dw} &= r_{CO_2} = -r_1 - r_2 \\
\frac{dF_{CO}}{dw} &= r_{CO} = r_2 \\
\frac{dF_{H2}}{dw} &= r_{H_2} = -3 \cdot r_1 - r_2
\end{aligned}$$

For each component, the variation of the molar flow dF_i aligns with the reaction rate r_i, when dw represents the mass of catalyst in the balance room. To enhance stability in coarser discretizations, the reaction rates were constrained by a parameter r_{max}. This approach significantly reduces computation time without compromising the reactor outputs.
As the reaction rates are not only depending on the partial pressures but also on the temperature, the change of temperature along the reactor must be taken into account 3.8 [LZF19]. The total molar flow-rate was changed to the mass flow, as the material values like average thermal capacity or density are calculated within the HTF class related to substance mass.

$$\frac{dT}{dw} = \frac{U \cdot a \cdot (T_j - T)}{\dot{m} \cdot C_{pm}} - \frac{\Delta H^{\circ}_{r1} \cdot r_1}{\dot{m} \cdot C_{pm}} - \frac{\Delta H^{\circ}_{r2} \cdot r_2}{\dot{m} \cdot C_{pm}} \tag{3.8}$$

where:

- dT is the temperature change of Temperature T along the reactor, related to the
- dw is the change of catalyst mass,
- U is the total heat transfer coefficient,
- a is the specific surface area for the heat transfer per kg catalyst,
- T_j is the temperature of the reactor wall,
- $\dot{m}$ is the mass flow,
- C_{pm} is the average specific heat.,
- ΔH°_{ri} is the reaction enthalpy of reaction i,
- r_i is the reaction rate of reaction i.

For the calculation of the pressure drop, the Ergun equation was implemented 3.9 [LZF19].

$$\frac{dP}{dw} = \frac{G}{\rho \cdot g_c \cdot d_p} (1 - \Phi)^3 - \frac{150 \cdot (1 - \Phi) \cdot \mu}{d_p} + \frac{1.75 \cdot G}{S \cdot (1 - \Phi) \cdot \rho_p} \tag{3.9}$$

where:

- P is the pressure,
- dw is the change of catalyst mass,
- G is the superficial mass velocity,
- g_c is a conversion factor in $\mathrm{kg}/m^3/s^2\mathrm{N}$,
- d_p is the average equivalent diameter of catalyst pellets in the bed,
- Φ is the bed porosity,
- μ is the fluid viscosity,
- z is the reactor length,
- S the tube cross section surface area,

- ρ_P is the density of catalyst pellets.

This model represents a pseudo-homogeneous model which would lead to an ordinary differential equation system. The pseudo-homogeneous model neglects concentration and temperature gradients between the gas phase and the solid catalyst phase, while also neglecting the axial heat and concentration diffusion. However, this model still accounts for the decrease in total molar flow rate as the sum of substance flow rates is formed after the reaction for each balance room.
The previously mentioned equations were integrated into the components, with the number of balance rooms serving as a parameter. This allows users to change the discretization of the reactor. For each slice of the reactor, material balance equations, temperature development and pressure drop are calculated. Additionally, the heat flow to the environment is calculated and offset by the electric heater within the reactor wall. Using the temperature and the pressure, for each calculation loop, the fluid properties of the reactants are calculated by accessing the HTF class where the information of the fluid behavior is stored. A closer description of the HTF class can be found in subsection 3.2.1.

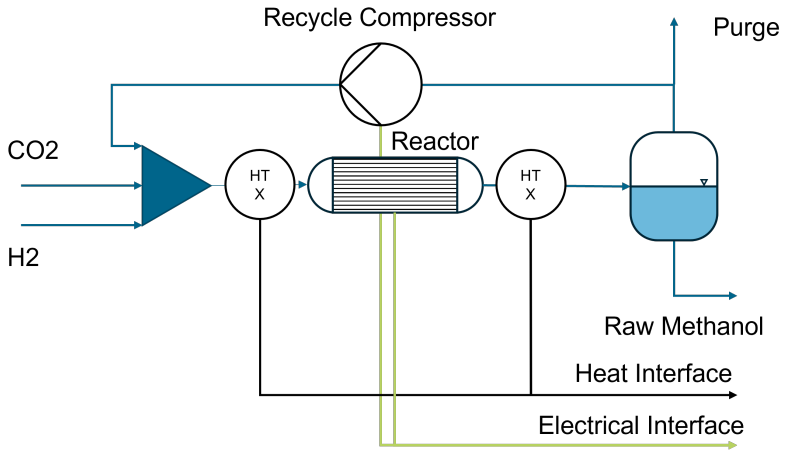

Figure 3.5: Synthesis subsystem with reactor, heat exchangers, recycle compressor, purge valve and interfaces for heat (black) and electricity (green).

The reactor component has a large number of fluid flow interfaces, one in- and one outflow for each chemical component, and an electric flow interface for the heating of the reactor. Actual inflows from the system level, however, are only hydrogen and carbon dioxide; the rest can only enter the reactor through the recycle stream. A schematic of the synthesis subsystem is shown in figure 3.5. This grouping of components is also more reasonable because the reactor is almost exclusively operated as a looped reactor. Therefore, the reactor's handling at the system level is more intuitive, and resembles the approach to the reaction section as seen in the works of Manenti et al.[MCR11] or Jeong et al. [Jeo22]. The products (water and methanol), are separated from the other outflows (hydrogen, carbon monoxide and carbon diox-

ide) and fed to the distiller. The separation of water and methanol from the other gases is performed in a gas-liquid separator at reactor outlet pressure, in which all the reactants are cooled until water and methanol are completely liquefied. The gases are then compressed and mixed with the feed flow of hydrogen and CO_2 and then reheated to reactor inlet temperature. As not all of the outlet gases might be able to be fed back to the reactor due to unfavorable molar fractions, a purge valve is implemented before the gases enter the recycle compressor. As a rule of thumb, the recycle feed is around five times bigger in weight than the fresh feed of hydrogen and CO2 [PFSBT16].
To start the reactor, the inflows are tracked, and once the pressure within the reactor reaches 80 bars, the calculation is started. If at that point the reactor has not yet reached the reaction temperature necessary for catalyst operation, the reactor operates without altering the molar flow-rates, gradually heating up due to convection between the reactor walls and the reactants. This means, that the startup time is also determined by the reactor size, and the inflow rates.
Once the reactor is filled and the reaction temperature is reached, the recycle stream is started and a new time step is initiated in YACOP. This new time step has the duration of the residence time of the reactor under the current inflow, meaning the recycle stream is now available at the outlet of the reactor. Starting with this new time step, the recycle stream is mixed with the hydrogen and carbon dioxide entering the synthesis subsystem and the reactor is calculated with the now increased mass flow. With the mixture of the recycling stream, the inlet concentrations of the reactor are now changed. This again, changes the reactor outflows. Therefore, multiple recalculations of the reactor are performed until the system reaches a steady-state. Steady-state is defined to be reached when the inflow concentrations of the reactor in the new time step are within a defined mass tolerance, compared to the inflow concentrations of the previous time step. This parameter has a huge influence on how many times the reactor is recalculated during startup or after load changes. If the steady state is reached, the calculation of the reactor is skipped, and the outflows are those of the previous time steps.

3.4.1 Limitations of the kinetic model

Especially Mignard et al. [MP08] highlight some limitations of the implemented simulation. The model does not consider the production of any by-products that could affect the catalysts performance. Additionally, pore diffusion would be expected to decrease the rate of methanol production. However, this mechanism is often inaccurately modeled, as it is typically considered viable only for first order reactions. To compensate this, the residence time in the reactor would have to increase. [MP08]
The kinetic model has its own restrictions and there is still some disagreement over the actual reaction mechanisms. The model is based on partial pressures rather than fugacities, which would describe the equilibria better according to Graaf et al. [GSB88]. As the reactor model deals with a mixture of polar and non-polar components at high pressures, this might be the source of some inaccuracies. [MP08]

Moreover, Klier et al. [KLI82] found that high concentration of CO2 such as 20% and higher, may lead to a significant formation of methane.
Even though the model provided by Mignard et al. is a big improvement over older ones, there might still be some big misunderstandings about how the reaction actually works. Ostrovskii et al. in 2002 discovered that, under normal conditions for methanol production, water is not adsorbed or desorbed by the catalyst like previously assumed. Instead, it appears that water either oxidizes the catalyst, releasing hydrogen, or undergoes chemical reactions on the catalyst's surface, leading to its decomposition. This discovery contradicts the theory and kinetic model described by Froment and Vanden Bussche [Bus96].
Ostrovskii also found that the location of the water-gas shift reaction takes place on the copper part of the catalyst, while the methanol production takes place on the ZnO parts. His experiments supported the findings of Bussche et al. and Van-Dal et al. that CO2 is the primary carbon source for methanol production. Additionally, his research suggests that CO and CO2 attach to different sites on the catalyst. This finding disagrees with what was once considered solid research by Vanden Bussche and Froment in 1996. They claimed that both reaction (A1) and the WGS-reaction happen only on the copper parts, even though ZnO improves this process. However, Ostrovskii noticed that conventional methods, like temperature-programmed desorption (TPD), may not effectively remove all the residual carbon materials, CO2, and water from the catalyst. This could result in incorrect initial catalyst conditions prior to experiments and lead to variations in kinetic parameters. For instance, Vanden Bussche and Froment in 1994 prepared their catalyst by treating it with CO at 250 degrees Celsius and then heating it under argon at 280 degrees Celsius. But Ostrovskii showed that you need temperatures between 400–450 degrees Celsius to completely remove CO2 and water. [Ost02] [MP08]

3.5 Distillation

This section is focusing on the implementation of the distillation column and can be divided into two parts. The realization of the steady state simulation is explained in the first part, considering the calculation of the heating and cooling duties and the heat loss to the environment. The second subsection focuses on the startup simulation. Here the considered literature is presented again in detail and the implemented methods are explained.
During regular operation, the distillation column is designed to calculate the steady-state output of methanol and water, considering the current feed concentration specified parameters such as number of stages, reboiler power, feed stage location, reflux ratio and desired top and waste concentrations. Additional parameters like tray size play a crucial role in determining the startup duration, as further explained in section 3.5.1.
In each time step, the conditions for methanol production are evaluated. This involves checking if the column is filled and if the feed is greater than the minimum inflow. Vapor-liquid-equilibria in the column are then calculated to assess whether methanol production if feasible given the current feed concentration. The implemented functions for the rectification part of the column can be seen in the appendix 6.2. Additionally, it is verified whether the concentration at the bottom of the column is below the specified waste concentration to prevent methanol loss through the bottom. If the column is not yet filled, the startup is calculated, even if the minimal load is not met.
Depending on the partial load, the condenser and reboiler duties are calculated according to the internal mass flows:

$$Q_{Condensator} = -\dot{m}_{Condensator} \cdot \Delta H_V = -V \cdot M_{Methanol} \cdot \Delta H_V(Methanol) \quad (3.10)$$

$$Q_{Reboiler} = \dot{m}_{Reboiler} \cdot \Delta H_V = (L - B) \cdot M_{H_2O} \cdot \Delta H_V(H_2O) + Q_{loss} \quad (3.11)$$

with:

$$Q_{loss} = \alpha \cdot A \cdot \Delta T \cdot + \epsilon \cdot \sigma \cdot A \cdot (T_{wall}^4 - T_{amb}^4) \quad (3.12)$$

where in accordance with figure 2.9:

- $\dot{m}_i$ are the mass-flows or $(L-B)$ or V are molar-flows through the components,
- $\Delta H_V(substance)$ the evaporation enthalpies of the respective components,
- M the molar masses of the respective components,
- A is the cylindrical are of the column,
- ΔT is the temperature difference between the column wall and the environment,

- $\alpha = Nu \cdot \lambda_{air}/h_{column}$ is the convective heat transfer coefficient,
- Nu is the Nusselt number,
- λ_{air} is the thermal conductivity of the surrounding air,
- h_column is the column height,
- ϵ is the emissivity of the column surface,
- σ is the Boltzmann constant.

The reflux flow is assumed to be liquid at boiling temperature, while the vapor from the reboiler is considered to be at saturation temperature. As the methanol concentrations are greater than 99.9% at the tope or lower than 0.1% at the bottom, the substances are assumed to be pure to calculate the conversion from mass-flow to molar-flow and the evaporation enthalpies. The heat loss of the distillation column is added to the reboiler duty.
The feed is fixed to be at saturation temperature to simplify the calculations and avoid incorrect positioning of the feed tray. Not only does this lead to the same substance balances within the column, it also results in an easier comparison between different reboiler and condenser duties. However, this approach necessitates an additional heat exchanger at the system level to bring the feed flow to saturation temperature.
The partial load limits and the partial load behavior of distillation columns are determined by the susceptibility of the column to weeping and flooding. Weeping occurs when vapor flow in some parts of the column diminished, causing liquid to weep through trays into the trays below, thus reducing tray efficiency. This issue can be mitigated using bell bottom trays with chimney to prevent weeping. Conversely, flooding arises from excesive liquid volume or foam generation during downcomer flow and mixing. These occurrence prevent fluid from reaching the tray below, leading to decreased tray efficiency. Tray type, tray and column geometry, as well as the nature of the separated liquids, heavily influence these phenomena. Therefore, parameters for minimum and maximum load were incorporated to accommodate this behavior.
Multiple assumptions are made here:

- complete separation of methanol and water,
- fluid entering the column at saturation temperature,
- steady state/neglecting dynamic effects during load/concentration changes in the feed,
- simplified upper and lower bounds of the flow rates.

These assumptions simplify the distillation column model, primarily to reduce the number of parameters that might only influence the components performance on a very detailed level.

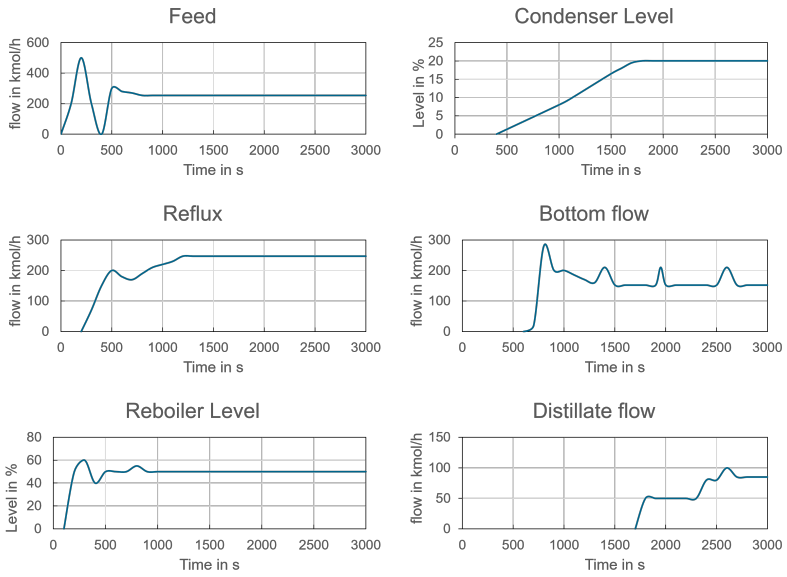

Figure 3.6: Startup of the distillation column with the control strategy of Neves et al. [NAM99]

3.5.1 Startup Simulation

As mentioned before the availability of broadly applicable cold startup models is very limited [WLWW03]. Two of the most detailed approaches were made by Neves et al. [NAM99] and Fabro et al. [FAN05], which are further explained in this section, starting with the findings of Neves et al.

In figure 3.6, various levels and flows during the startup operation are shown. The feed gradually increases from t = 0 s until it peaks at 500 kmole per hour around t = 100 s. Subsequently, the re-boiler level starts to rise, causing the feed stream to decelerate until it reaches 0 kmole per hour again by t = 200 s. During that period, the re-boiler reaches the 50% mark and starts operating. This can be observed in the re-flux stream and the condenser level, both of which begin to ascend. The feed rate is linked to the re-boiler level; when the reboiler drops below 50% , the feed rate increases until it reaches the steady-state at around t = 800 s. Shortly after that, the bottom flow changes from 0 to 250 kmole per second, and then slowly oscillates around it's steady state of 152 kmole per second. Once the condenser is filled and the desired product concentration is reached at t = 1800 s, the column starts to produce methanol and the distillate flow quickly reaches it's steady-state of 85 kmole per second. [NAM99]

Fabro et al. introduce another control system for the startup of continuous distillation columns based on the parameters and framework of Neves et al. This system utilizes a combination of recurrent neural networks, fuzzy logic controllers, and genetic algorithms to efficiently manage the complex process of initiating distillation

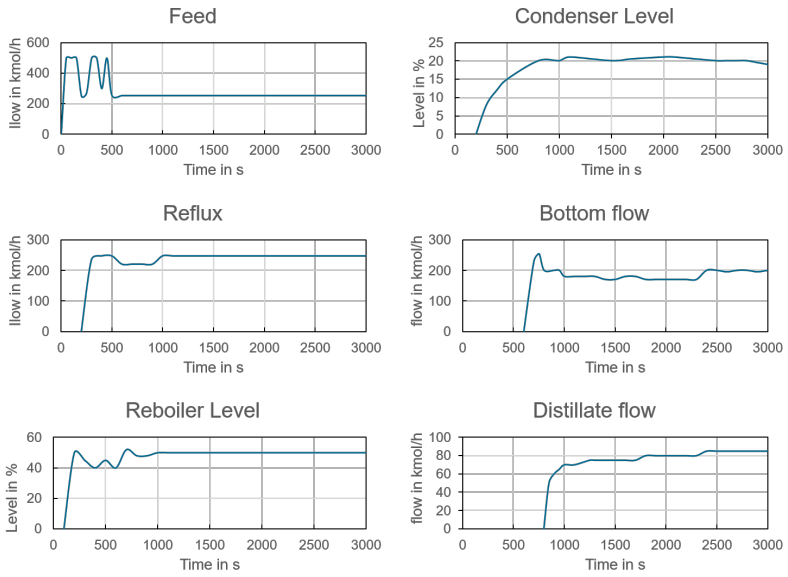

Figure 3.7: Greater feed stream and earlier production in the startup process of the distillation column with the control strategy of Fabro et al. [FAN05], compared to Neves et al. [NAM99]

operations. The core challenge addressed is the difficulty of controlling the distillation column during startup due to its nonlinear behavior and varying operational phases. The proposed control system was tested through simulations, demonstrating enhanced performance compared to traditional methods and the control strategy proposed by Neves et al, see figure 3.7. Although the feed rate can be maintained at a higher value, the re-flux flow, and especially the condenser level, rise earlier and more rapidly in the optimized startup process. While this does significantly affect the bottom flow-rate, the distillate flow starts nearly 1000 seconds earlier, indicating that production starts nearly twice as fast. [FAN05]
For the simulation of the startup of the distillation column, a model closely resembling the startup strategy proposed by Fabro et al. [FAN05] was implemented, although some simplifications where made. Since only the startup time and energy are important, no detailed control strategy needed to be implemented. The startup can essentially be divided into three phases, as depicted in figure 3.8:

1. Filling the stages below the feed stage and the reboiler.
2. Starting the reboiler and filling the condenser and the stages above the feed stage.
3. Cutting of the feed stream and operating the distillation column with total reflux, to achieve the desired concentrations at the top and bottom.

During phase two and three, the reboiler is running either at full power, or according to the inflow mass of the distillation column, while the condenser is coupled to the

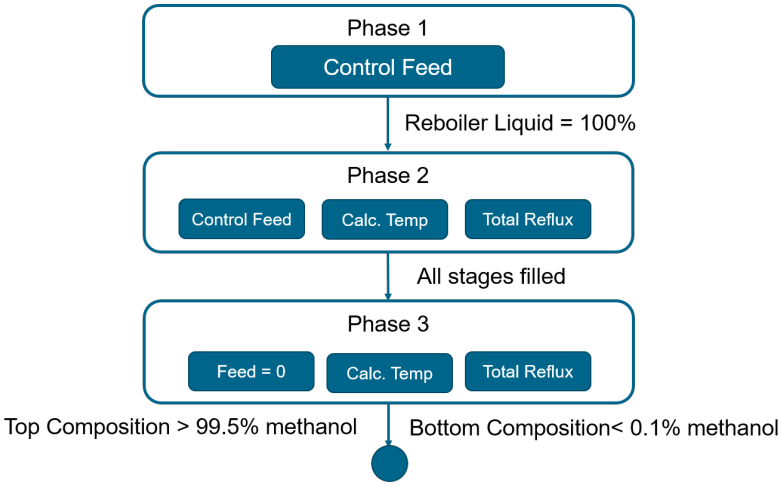

Figure 3.8: Simplified startup process to calculate the filling time and the heating and cooling duties.

total vapor flow-rate in the column, as all of the vapor stream needs to be condensed. This means that along with the total fluid volume of the distillation column with condenser and reboiler included, the duration of the startup is also depending on the inflow rate and the maximum reboiler power.

While the column is filled at the end of the calculated startup time, it is not clear if the concentrations at the top and bottom are acceptable for production or waste removal respectively. However, in the startup simulation described by Fabro et al., the distillate flow begins when the accumulated fluid in the system reaches a state equivalent to the steady-state filling levels of full trays, along with partly filled reboiler and condenser units [FAN05]. This is also the case for the startup process proposed by Neves et al. [NAM99]. However, with a lower feed stream rate, the condenser level progresses much more slowly. Based on these results, the assumption was made that if the liquid accumulated in the column is equal to the total liquid volume of the distiller, production is possible at steady-state conditions, given the fairly large time step size.

To avoid additional time splitting due to the start of production of the distillation column, a productivity value is implemented. This productivity value is directly proportionate to the duration of production in the current time step. Essentially, if the column is only filling, and not producing during a time step, the productivity value is 0. Conversely, if the column is producing 60% of the duration of the time step, the productivity value is 0.6 and so on. This approach allows us to account for the delay in production without complicating the time splitting process. The delay of production is in this sense not directly visible as a delay in time, but a penalty on the production capacity of the distillation column. If the distillation column is not filled at the end of the time step, there is not any product or waste flow during this time step. This is only valid for a system, where no other component is depending

on the methanol or water/waste flow out of the distillation column temporally.
In addition to the simplified model described before, another startup calculation was implemented, to estimate the startup time of the distillation column while simulating the vapor liquid equilibria within the column at the start of the time series calculation. This startup calculation was also divided into the three phases shown in figure 3.8. As the reboiler is idle during phase one, the calculation of the equilibria starts in Phase two, as vapor is introduced at the bottom of the column.

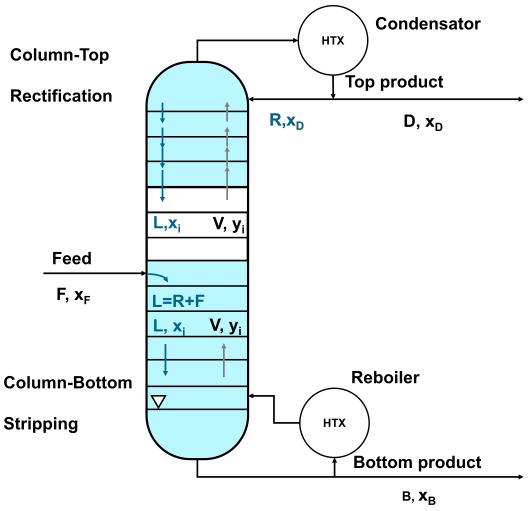

Figure 3.9: Phase two of the time series startup calculation

Figure 3.9 shows the distillation column during phase two. The stages below the feed are already filled, displayed blue, while some stages above the feed are also full. The highest tray that is displayed white, is the tray that is currently filled by the liquid coming down from the stage above and the vapor coming from the bottom. The temperature in each tray is calculated by the boiling temperature of the current mixture in the tray. This means, that for every mole that condenses inside the tray, one mole of liquid also leaves the tray in the form of vapor to enter the stage above. This way, at the very beginning of stage two, the vapor rising from the feed tray enters the condenser directly, while the fluid exiting the condenser enters tray one. Fluid exiting the respective trays is only occurring, when the tray is filled. Once all stages are filled, the feed stream is shut down, and the column enters to total reflux state. This state is held, until the desired concentrations at the top and bottom are reached. While this resembles coarsely the behavior of the column in the real startup process, many assumptions regarding the dynamic behavior are made. This simplified approach does not only neglect the partial filling of the condenser as it is shown in the simulation by Neves et al. and Fabro et al., but also the liquid accumulating through condensation in the other trays, as the column temperature in the beginning is still colder than the boiling temperature of the mixture. Additionally, all the assumptions of the steady-state Mccabe-Thiele-Method are made, such as equal

molar flows throughout the column in Phase three, ideally mixed trays and similar molar enthalpies of the fluid. A critical assessment of the implemented process is done in chapter 4. As there was very little data to validate this model, it is not part of the final version of the distillation column model, but may be further improved and possibly included in future studies.
The startup time is mostly affected parameter-wise by the liquid holdup of trays, reboiler and condenser and the reboiler power. Additionally, factors like the total amount of produced methanol and water play significant roles. While the energy required to heat the column's metal to processing temperature is relatively minor compared to other phases, it's overshadowed by the continuous evaporation of the entire feed stream in phase one, and the further evaporation of the reflux flow in phase three.

4 Results

In this chapter, the validation of the implemented components and simulation results are presented. The chapter begins with a section on the alkaline electrolyzer model, followed by an exploration of the findings related to the electrolyzer system. Subsequently, the validation of the methanol reactor is discussed, comparing the implemented model to reference results. Additional comparisons of the reactor with literature can be found in the appendix. Next, the validation of the distillation column is presented, focusing first on the startup validation and afterwards on the steady-state behavior. In the final section, the system is evaluated, and the results are compared to the literature, firstly focusing on the startup and steady state behavior and then showcasing the systems behavior under partial load scenarios. Especially the rise and drop in load are examined, and the role the individual components play during these load changes.

4.1 Alkaline Electrolyzer

In this section, the results of the alkaline electrolyzer component are presented. The initial focus lies on validation in the first section. Here, the implemented electrolyzer is compared to the initial model of the electrolyzer taken from literature, focusing on the interrelation of temperature and current. This subsection is followed by a further examination of single stack behavior. Here the heat up process of the electrolyzer stack is discussed and the different cooling modes are presented. The temperature dependency of the efficiency is also discussed in this part of the chapter. Subsequently, the third section delves into the results and discussions surrounding the electrolyzer system with multiple stacks. This last subsection is primarily showcasing the different behavior of electrolyzer systems in contrast to single stack behavior.

4.1.1 Validation

This subsection focuses on the validation of the electrolyzer model by comparing it to the model in literature presented by Ulleberg [Ull03], on which the implemented electrolyzer is also based.
Figure 4.1 shows the current and temperature of the electrolyzer that was implemented in YACOP compared to the electrolyzer model of Ulleberg [Ull03]. The parameters of the electrolyzer stack are summarized in table 4.1, while the parameters for the cell voltage and the faradaic efficiency are those of Ulleberg, already mentioned in section 2.1. The initial temperature at $t = 0$ hours is 323.6 K. For the

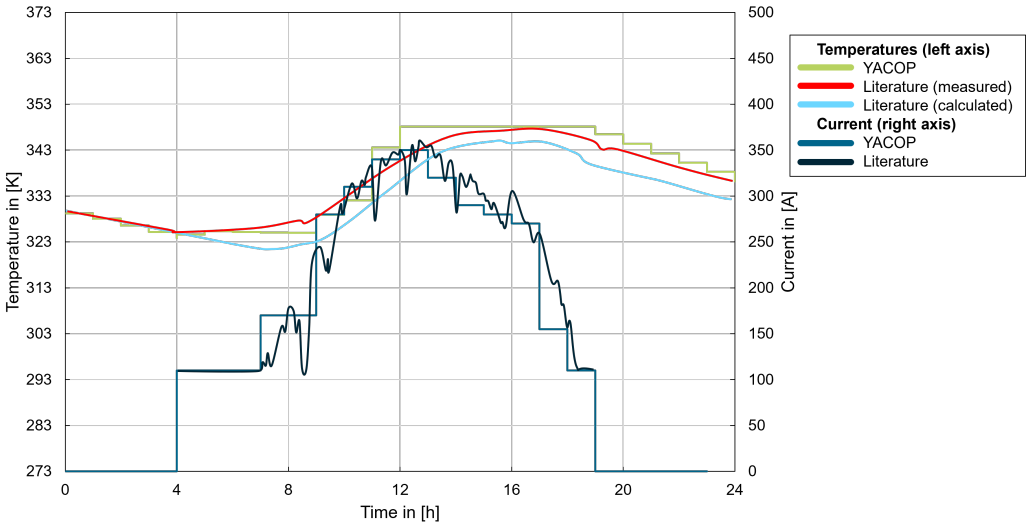

Figure 4.1: Electrolyzer model in YACOP compared to the electrolyzer model presented by Ulleberg [Ull03]. Temperature and current over 24 hours.

Parameter	value	unit
Operating pressure	7	bar
Nominal temperature	75	°C
Stack power	26	kW
Startup time	1800	s
Hydrogen production	0.2512	kg/h
	2.9	m^3/h
Heat Capacity	625	kJ/kg

Table 4.1: Validation parameters of electrolyzer (PHOEBUS electrolyzer) [Ull03]

first 4 hours of the simulation, the current and thus the hydrogen production is set to 0. At $t = 4$ hours, the current is set to 100 A. However, in Ulleberg's simulation, the flow of cooling water also initiates at this point, marking a notable difference between Ulleberg's work and the model presented in this study.

In Ulleberg's approach, the cooling flow is predetermined based on the set value in the experiment. In contrast, in YACOP, the cooling demand is calculated as an estimation of the required cooling to maintain the temperature of the electrolyzer within an acceptable range. As a results, while the temperature in YACOP has already stabilized, Ulleberg's simulation shows the temperature beginning to rise after $t = 7$ hours when the current is increased. From this point, the distinct dynamics between the two simulation become evident.

A crucial factor to consider when comparing the two simulations is the time step size: in YACOP, it is 1 hour, whereas Ulleberg's simulation had a time step size of only 5

minutes. This implies that not only is the current approximated in YACOP, but also that the resolution of the temperature development is lower. Particularly during the initial hours after the initial start of the electrolyzer, the current in YACOP is, on average, slightly higher than in Ulleberg's simulation, which could partly explain the higher temperature during this time frame. The maximum temperature after which cooling is initiated in YACOP, is reached at $t = 12$ hours, at 75°C. Unfortunately, it is challenging to compare the cooling amount in YACOP to the results of Ulleberg, as the outlet temperature of the cooling water is not mentioned [Ull03]. In general, the electrolyzer in YACOP reaches a higher temperature, which could be explained by the immediate cooling of the electrolyzer in Ulleberg's simulation, in contrast to the cooling in YACOP, which depends on the actual stack temperature.

4.1.2 Single Stack

In this subsection, the parameters are changed to those in table 4.2, while only the results of a single stack are presented. Here, the behavior of the stack temperature during the heating process is visible and with it the effect the temperature has on the efficiency. The production capacity and the nominal power are significantly higher, as well as the operating pressure, compare table 4.1. The stack parameters resemble those of the complete system described in subsection 4.4.

Parameter	value	unit
operating pressure	40	bar
nominal temperature	90	°C
system power	20	MW
number of stacks	9	
stack power	2.22	MW
startup time	1800	s
Nominal hydrogen production		
system	375.12	kg/h
system	7776	m^3/h
stack	41.688	kg/h
stack	463.68	m^3/h

Table 4.2: Production parameters of electrolyzer system and stacks

In figure 4.2, the hydrogen production of a single alkaline electrolyzer stack is plotted over 48 hours, along with the overall efficiency, which is calculated using the Lower-Heating-Value of hydrogen, within the following equation:

$$\eta_{el} = \frac{LHV \cdot \dot{m}_{hydrogen}}{P_{el}} \tag{4.1}$$

Production starts at $t = 5$ hours at 30% of the nominal production rate. The overall efficiency is mainly influenced by two key factors: the stack temperature and the production rate. Lower hydrogen production rate in the stack result in lower currents and

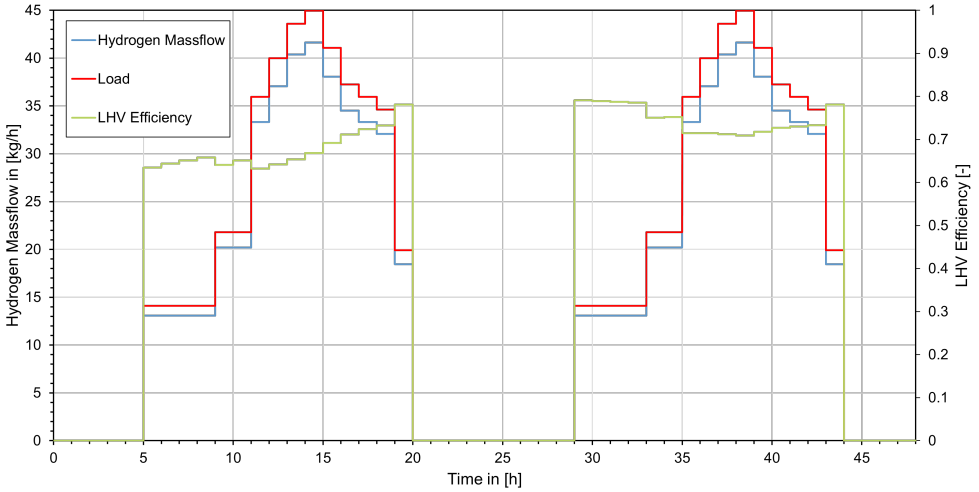

Figure 4.2: Hydrogen Production and Lower-Heating-Value efficiency of a single stack over 48 hours

thus lower current densities, as hydrogen production is directly proportional to the current 2.10. According to the equation for the cell voltage 2.9, lower current densities result in lower cell voltages. As the product of the two is equal to the consumed power in the electrolyzer, the overall efficiency η_{el} is higher at lower hydrogen production rates. Ideally, production is chosen to be at the rate, where the cell voltage is equal to the thermo-neutral voltage U_{th} to eliminate the need for cooling 2.1. However, achieving thermo-neutral operation for all electrolyzer stacks becomes challenging when the available power or the hydrogen demand varies. The temperature development of the stack is plotted in figure 4.3 over the same time span. When comparing the lower partial load periods from $t = 5 - 9$ hours, the effect of temperature on the efficiency is significant. This is also an effect of the lower cell voltages at higher temperatures, as explained in chapter 2.1.
Furthermore, it is evident that the stack temperature increases more rapidly during periods of higher production and decreases during times of no or low production, as observed from $t = 29$ to 33 hours. Here, the stack temperature is decreasing while remaining relatively high, which results in increased heat transfer to the environment and reduced heat production due to improved efficiency.

4.1.3 Electrolyzer System

In this subsection the results of the implemented electrolyzer system are presented. Especially the different behavior of multiple stacks in contrast to a single stack electrolyzer is a key aspect of this subsection. The electrolyzer parameters used in the simulation are summarized in table 4.2.
Figure 4.4 shows the accumulated production of an electrolyzer system with n=9 stacks and a startup time of $t_{startup} = 1800$ seconds with a 50% production rate

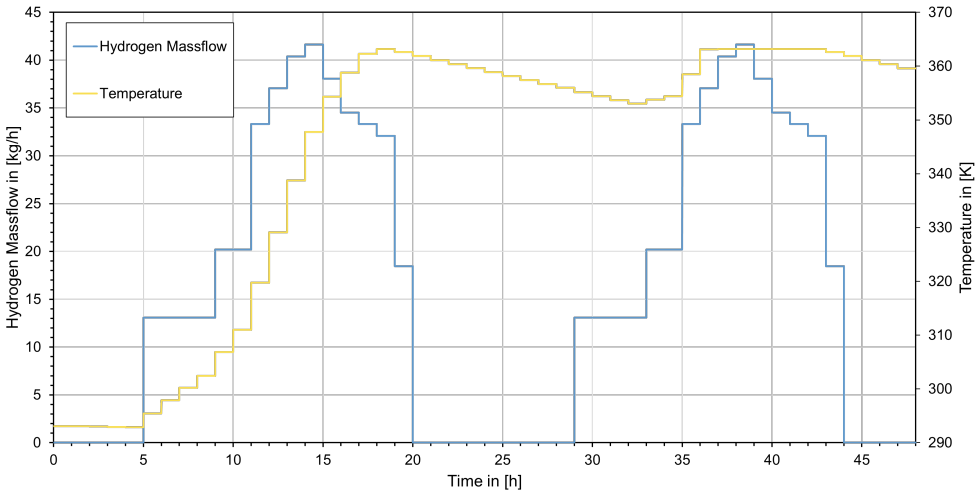

Figure 4.3: Temperature and hydrogen production of a single electrolyzer stack over 48 hours

during the startup. The water inflow, from which the hydrogen demand is calculated, is shown in figure 4.5. At $t = 0 - 0.5$ hours, seven of the nine electrolyzer stacks are running to produce the desired amount of hydrogen, while at $t = 0.5 - 1$ hour, more hydrogen can be produced with only 4 stacks. This is due to the startup time of 1800 seconds, during which all of the stacks can only produce at 50% capacity. The impact this has on hydrogen production is also evident at $t = 8$ hours. From $t = 7 - 8$ hours, *stacks*7 to 9 are idle, so the sudden rise in hydrogen demand at $t = 8$ hours cannot be met immediately by these stacks due to their startup time. This results in a water outflow from the electrolyzer system, as shown in figure 4.5, at $t = 8$ hours for 1800 seconds. This phenomenon occurs multiple times within the shown time frame, consistently following significant changes in the load (at $t = [0, 4, 7, 11, 14, 17, 19, 22]$). In figure 4.5 this behavior leads to a negative H_2O flow out of the electrolyzer system, the exact amount that could not be converted to hydrogen and oxygen in that time step.

Figure 4.6 shows the stack temperatures of *stack 1*,n *stack 5* and *stack 9* during the same period. *Stack 1*, which operates continuously at 100% capacity, shows an increase of the steady temperature until it stabilizes at the desired steady-state temperature of 363.15 K (90 °C). In contrast, *stack 9*, which is active for a total of 3 hours, has a significantly lower temperature at the end of the 24-hour period compared to *stack 1* and *stack 5*. It is also evident that *stack 5* experiences greater heat loss, indicated by a sudden temperature decrease observed between t=8-10h. In contrast, *stack 9* exhibits lower heat loss due to its smaller temperature difference with the environment. Alongside the stack temperatures, the total electrical efficiency of the electrolyzer system is also plotted. Since the cell voltage and efficiency are primarily influenced by the stack temperature, higher temperatures across all stacks result in higher overall system efficiency. The efficiency, approximately 68% with the

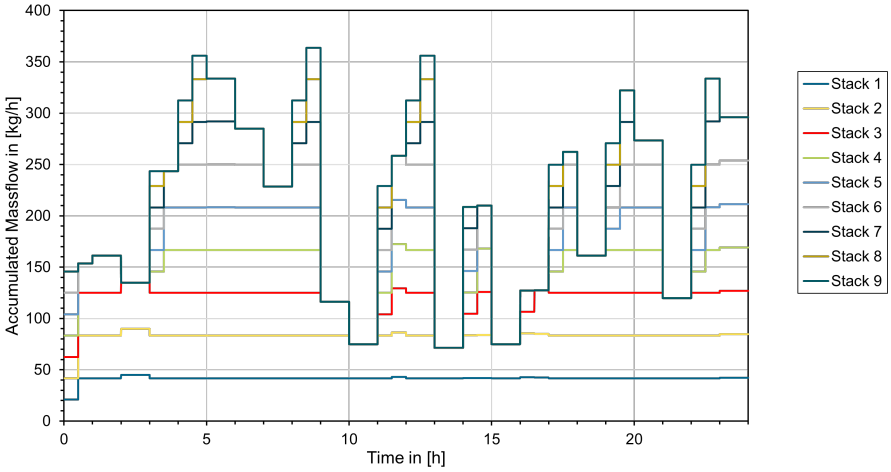

Figure 4.4: Accumulated hydrogen production for $n = 9$ stacks with $t_{startup} = 1800s$.

Lower Heating Value (LHV) or around 85% with the Higher Heating Value (HHV) of hydrogen, aligns well with the reported efficiency by Bertuccioli et al. [LADF14]. This underscores the validity of the temperature and load dependency of the overall efficiency for both the system and individual stacks.

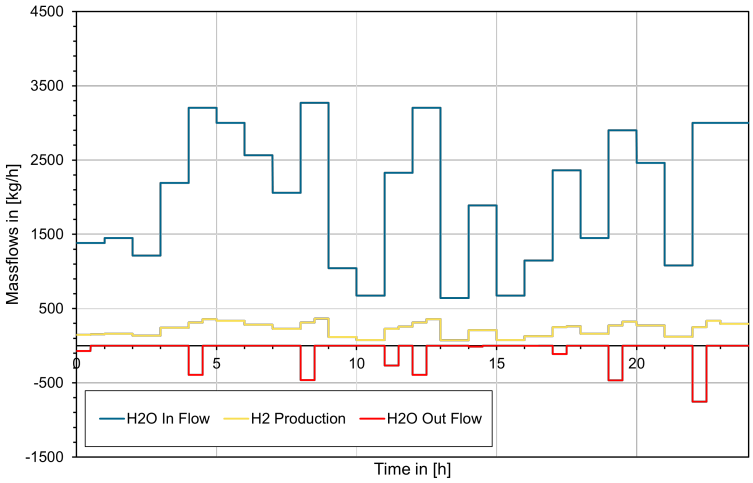

Figure 4.5: Electrolyzer system in and out flows for a startup time of $t_{startup} = 1800$s. Water out flows represent insufficient hydrogen production due to startup times.

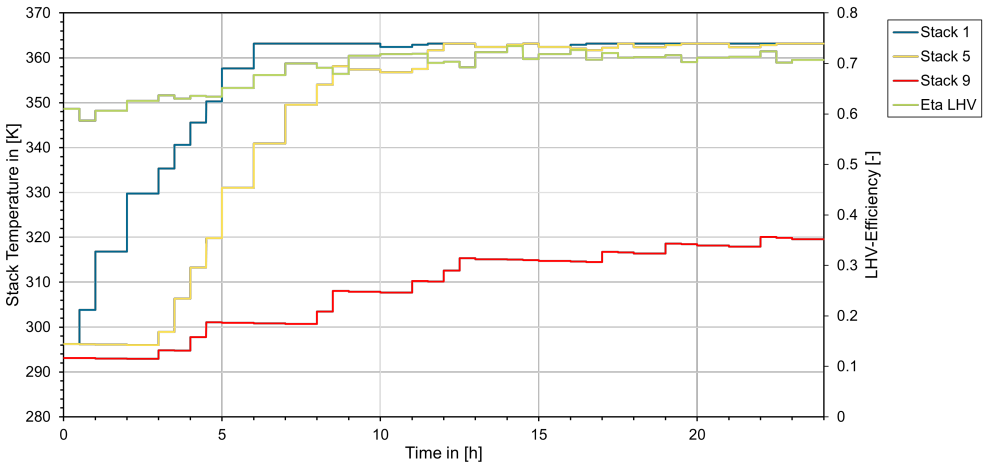

Figure 4.6: Temperatures of Stacks 1, 5 and 9 during the first 24 hours of production, along with the LHV-efficiency.

4.2 Methanol Reactor

This chapter focuses on the validation of the methanol reactor component. The overall reaction sequence at nominal inflow temperature is explained in detail while comparing the results calculated in YACOP to the results reported by literature. Afterwards, the reactor performance under varying inlet temperatures is examined and evaluated. Additional validations are presented in the appendix 6. As the evaluation of the production performance of the reactor is primarily an economic task, KPIs like selectivity and yield are not addressed in this work.

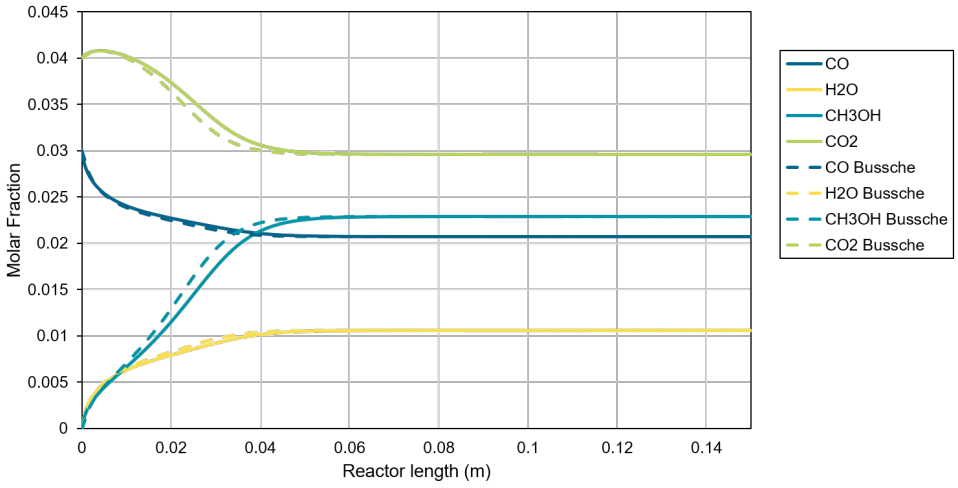

Figure 4.7: Molar Fractions of the reactor implemented in YACOP generated with the kinetics of Bussche et al., in comparison to the source material [Bus96]

Figure 4.7 displays the concentrations of methanol, carbon monoxide, carbon dioxide and water as simulated by the implemented reactor model in YACOP, compared to the model presented in the works of Bussche et al. [Bus96]. The parameters for the displayed simulation are listed in table 4.3.
As the water concentration in the beginning is 0, the rate of the Reverse-Water-Gas-Shift-Reaction (RWGS) is negative, which can be observed in the increase of CO. However, the formation of methanol indicates a positive reaction rate for the methanol synthesis reaction.
An inflection point can be seen at x = 2 cm, where the RWGS switches direction. As the reaction is endothermic, it hinders the temperature rise of the mixture, thus slowing down the reaction before that point. As Bussche et al. state, the reactor, or more precisely the reactor mass is exceeding the minimum amount needed to reach the equilibrium at the simulated flow rate. This is confirmed also in our simulation, as the concentration curves reach a steady state at x = 5 cm in the reactor.
The simulated molar concentrations at equilibrium almost perfectly resemble the concentrations simulated by Bussche et al. This is also the case for varied inlet temper-

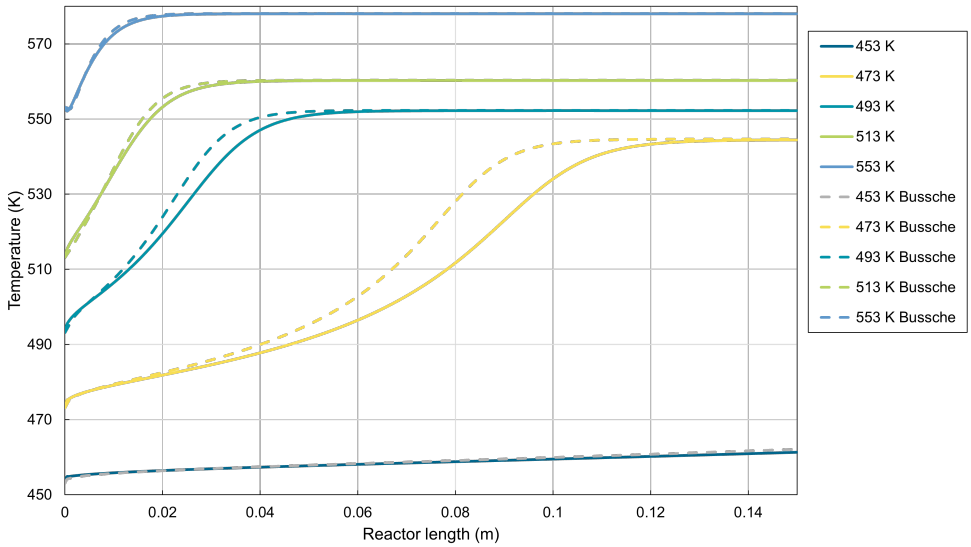

Figure 4.8: Temperature profiles with inlet temperature variation in accordance with the variations performed by Bussche et al.[Bus96]

atures in figure 4.9. However, there is a slight delay visible in the beginning of the reactor for the concentration profiles in 4.7. This is also present in the various temperature profiles of the inlet temperature variation diagram in figure 4.8. The difference is particularly noticeable at lower inlet temperatures, such as 473 K and 453 K. Since reaction speed and equilibrium are highly dependent on the temperature within the system, even slight differences in the temperature calculations can result in noticeable differences in the concentration profile. To calculate the change in molar flow, there are multiple approaches, some well summarized by Manenti et al. [MCR11], e.g. heterogeneous or homogeneous models. Depending on the chosen model, the reactor simulations yield similar but slightly different results, see also section 2.2. Unfortunately it is unclear which approach Bussche et al. used for their simulation. However, for the reactor in YACOP a homogeneous approach was chosen. There is also no energy balance given in Bussche's article. Whether the implemented reactor is ideal and neglects the axial diffusion of reactants is also not mentioned. Additionally, the differential equation system was not solved as such, but as a first order Taylor series approximation described in 2.2. It is indeed safe to say that Bussche et al. accounted for the decreasing number of moles, as evidenced by the equilibrium value of methanol concentration matching the calculated methanol concentration in YACOP. Nevertheless, it is important to bear this in mind when using the models, as it may lead to a more conservative approach when determining reactor dimensions, potentially resulting in a slight overestimation of catalyst mass.
For additional comparisons of the implemented reactor with literature, please refer to the appendix (6) of this work.

Operating Conditions			
Parameter	value	unit	
Catalyst			
	Density	1775	kg/m^3
	Porosity	0.5	-
	Mass	34.8	g
	Pellet diameter	0.0005	m
Reactor			
	Diameter	0.016	m
	Length	0.15	m
Feed conditions			
	T_{inlet}	493.2	K
	p_{inlet}	50	bar
	mass flow	2.8e-5	kg/s
Feed composition			
	CO	4	mol%
	H_2O	0	mol%
	$MeOH$	0	mol%
	H_2	82	mol%
	CO_2	3	mol%
	$Inert$	11	mol%

Table 4.3: Operating Conditions for the Simulation of the Bench Scale Reactor

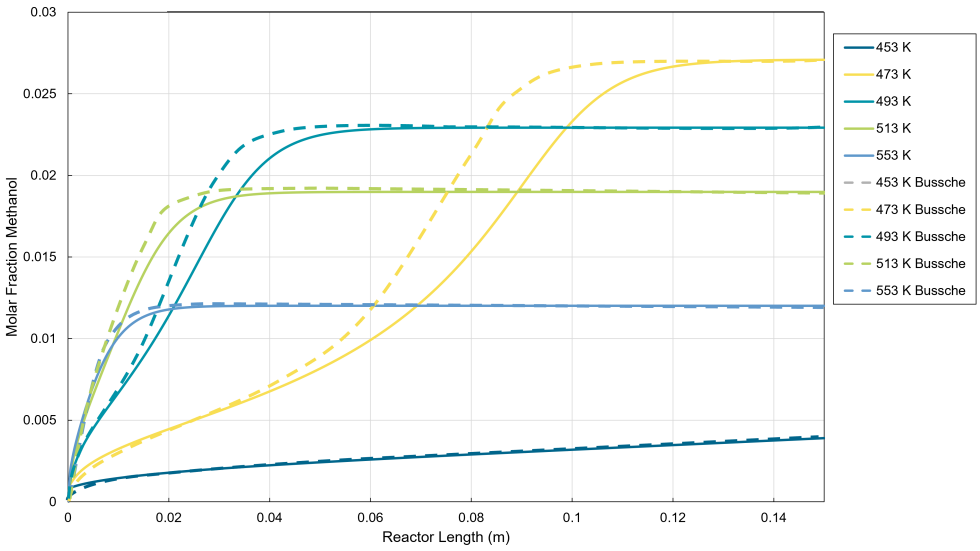

Figure 4.9: Methanol concentration profiles with inlet temperature variation in accordance with the variations performed by Bussche et al.[Bus96]

4.3 Distillation Column

In this chapter, the results of the distillation column are presented and discussed. The discussion is divided into two main sections: the startup process and the steady-state operation. First, the startup process of the distillation column is examined. This section covers the initial conditions, the procedures followed to initiate the distillation, and the transitional phases leading to steady-state operation. Various parameters influencing the startup, such as reboiler power, feed rate, and reflux ratio, are analyzed to understand their impact on the overall performance and efficiency of the column during startup. Following the startup analysis, the chapter investigates the steady-state operation of the distillation column. This section provides a comprehensive examination of the column's performance under stable operating conditions. Key performance indicators such as separation efficiency, energy consumption, and product purity are discussed. Additionally, the effects of different operational parameters, like the number of stages, condenser duty, and feed stage location, are evaluated to optimize the distillation process.

4.3.1 Startup

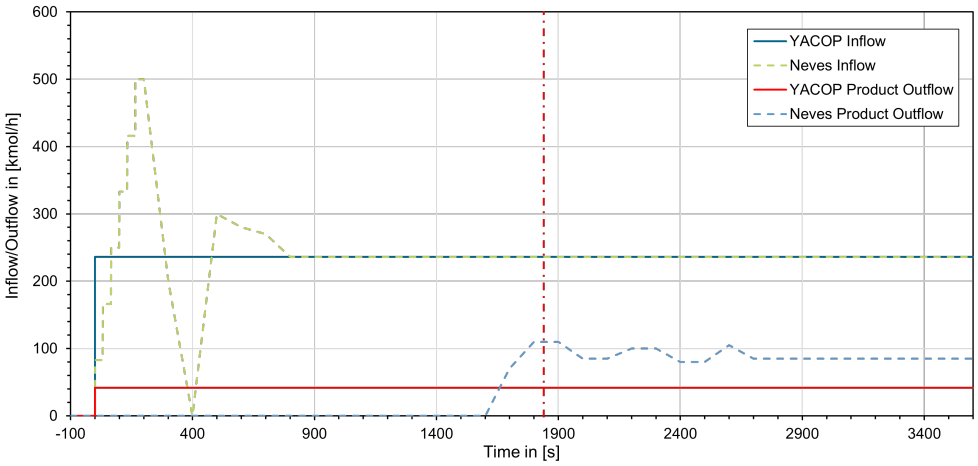

Figure 4.10: Comparison between the startup of Neves et al. [NAM99] and the startup implemented in YACOP.

Figure 4.10 presents the inflows and distillate during the startup process as reported by Neves et al. [NAM99], alongside the corresponding inflows and outflows of the model implemented in YACOP. The parameters used for the startup simulation are summarized in table 6.2. This comparison aims to validate the accuracy and performance of the YACOP model against established data.
In Neves' case, the feed varies between 0 and 500 kmol/h during the initial filling of the reboiler (steady-state holdup = 50%), which is completed at t=250s. It should

be noted that the steady state liquid holdup of the reboiler is only 50%, meaning the volume of the reboiler is only partially filled with liquid. At this point, all stages below the feed, along with the reboiler (see Figure 3.6). From this point onward, the feed increases to its steady-state value of 236 kmol/h, reaching this level at approximately t=450s. After around 1500 seconds, the condenser attains its steady state-liquid holdup, along with the other trays above the feed, as described in 3.5. From this point forward, the column produces at approximately 85 kmol/h, which is the steady-state value reported by Neves et al. [NAM99].
In YACOP, a constant inflow value of 236 kmol/h was chosen, as it represents the average inflow of Neves' simulation. The calculated startup time, with the parameters listed in table 6.2, is $t = 1841s$, indicated by the vertical dotted line in figure 3.8. As explained in section 3.5, the distiller outflow is calculated as an average over the time step to avoid additional time step splitting. Thus, the outflow for the entire time step is calculated to be around 49% of the steady-state value of 85 kmol/h, which is 41.53 kmol/h. As mentioned earlier in section 3.5, the delay in production is not directly visible as a delay in time but rather as a penalty on the production capacity of the distillation column. If the distillation column is not filled by the end of the time step, there is no product or waste flow during this time step. This approach is valid as long as no other component temporally depends on the methanol production. If for example a methanol tank is implemented, this approach has to be changed.

4.3.2 Steady-State

As the distillation column is operating exclusively at steady-state once the startup is complete, the accurate transition to the steady-state and estimation of the heat and cooling duties is essential. The parameters used for the steady-state simulation are summarized in table 6.3, based on the distillation column parameters provided by Pérez-Fortes et al. [PFSBT16]. This ensures that the model closely follows the established benchmark for similar distillation processes.
Figure 4.11 illustrates the mass flows within the distillation column. Our initial focus is on the startup process, occurring from t=7h until t=9h. During t=7-8h, the column is not producing any output. However, after t=8h, production begins according to the startup scheme described previously. Specifically, the column starts production around t=8.2h, achieving an average production rate of approximately 80% of its nominal capacity. By t=9h, the column transitions to steady-state operation, where 100% of the in-flowing methanol-water mixture is efficiently separated in its constituent components.
Figure 4.12 depicts the condenser and reboiler duties along with the total inflow and outflow mass flows of the column during the same time period. The startup process is clearly visible, with both reboiler and condenser duties rising to their startup values at t=7h. During the time step from t=8-9 hours, the column's filling is incomplete, leading to a situation where the total outflow remains lower than the total inflow. Consequently, the reboiler and the condenser duties have not yet reached their steady-state values, as the filling process is still ongoing at t=8h. Thus, from t=8-9h, the

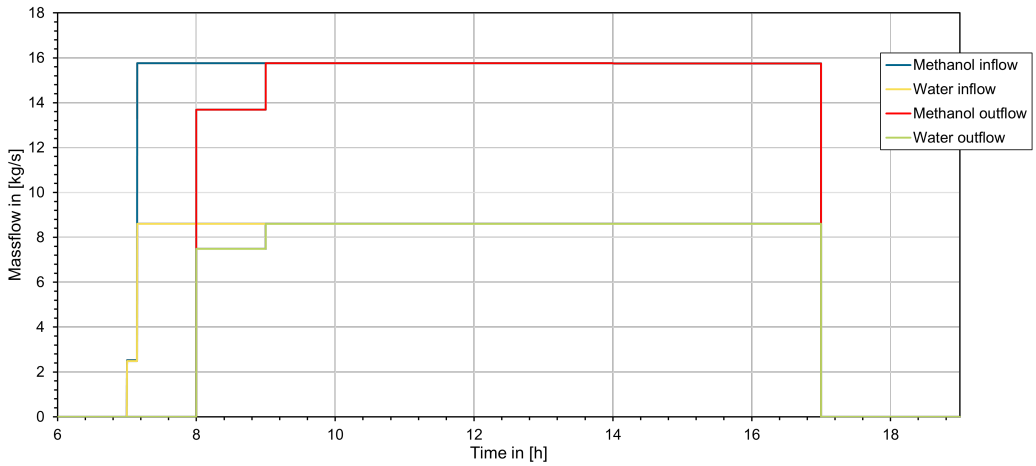

Figure 4.11: Mass flows of the distillation column over a 14h time period with startup delay.

reboiler and condenser duties consist of a combination of steady-state values and overlapping startup values, which extend into this time step. From t=9-17h the column operates in steady state, with the condenser duty now being lower than the reboiler duty.
It is evident that the condenser duty is significantly higher during the startup compared to during regular production. This observation is supported by the temperature distribution in figure 4.13, where most tray temperatures are lower than the feed temperature. During production, hot water exits the column at the bottom, and relatively hot product exits at the top. However, during startup, the column operates in a state of total reflux, meaning no fluid exits the column.
Since the feed temperature is fixed at the boiling temperature of the feed mixture at its respective concentration, the liquid in the trays above the feed must be cooled down relative to the entry temperature. The reboiler duty remains constant and cannot be reduced because all trays above the feed must be supplied with vapor produced by the reboiler. This necessity results in a higher condenser duty because, apart from heat losses, there is no other way for the excess energy to exit the column.
A plot with the condenser and reboiler duties under varying mass flows is shown in the Appendix 6.8, along with a comparison for the steady state temperatures of the column trays by Wang et al. [WLWW03].

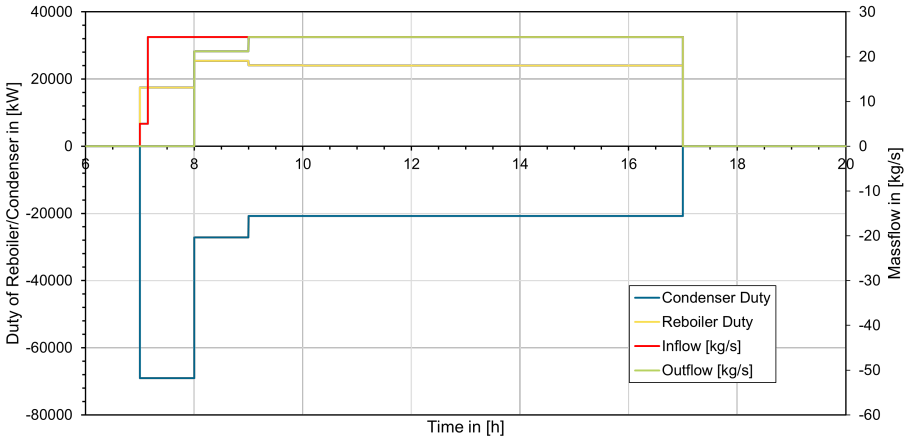

Figure 4.12: Reboiler and Condenser duties of the distillation column over a 14h time period with startup delay.

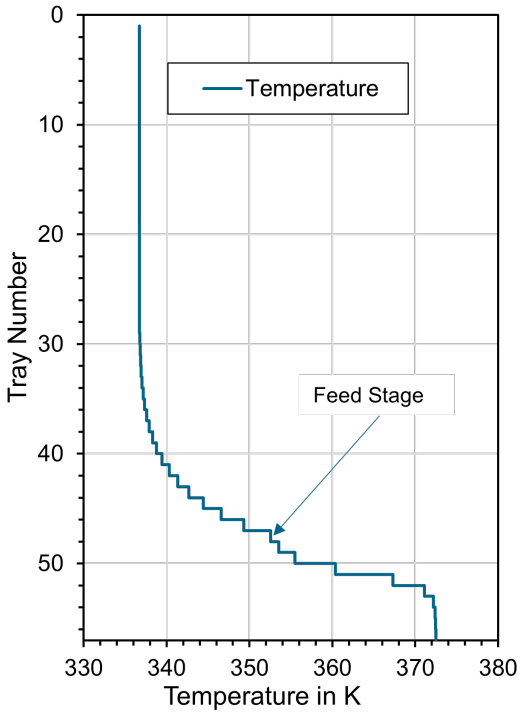

Figure 4.13: Tray temperatures in steady state calculated in YACOP, tray 1 being the top tray

4.4 System

This section is showcasing the results of the complete methanol synthesis system. Again, the section is divided into two subsections. The first one is examining the components effects on startup time and the inter-dependency of the components. In the same section, the results of the system simulation in YACOP are compared to similar synthesis plants in literature. The second subsection is investigating the systems behavior under a varying load scenario.

4.4.1 Startup and Steady State

In this subsection, the results of the complete methanol synthesis process are presented, focusing on the delay of production between the components and the steady state behavior. Additionally, the systems production and electricity, heat and raw material demands during steady state are compared to similar synthesis plants in literature. The parameters for this first startup simulation are summarized in tables 6.4,6.5 and 6.6 in the Appendix.

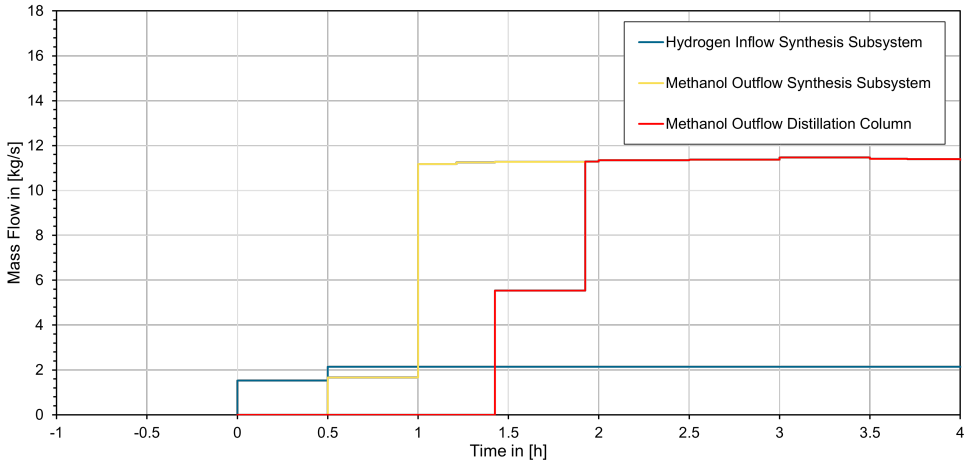

Figure 4.14: Mass flows of the methanol synthesis plant.

Figure 4.14 shows the mass flows during startup of the complete methanol synthesis system, including the alkaline electrolyzer, synthesis subsystem and distillation column, as described in section 3.2. In this startup case, the load is set to 70%. Starting at t=0h, the electrolyzer system operates at 50% of its nominal hydrogen production capacity. At t=0.5h, the startup period of 1800 seconds concludes, and the system increases production to 70% capacity, equating to 2.14 kg/s hydrogen. It takes over 30 minutes for the reactor to reach operating pressure and start production between t=0.5h and t=1h, producing an average of 1.66 kg/s of methanol. After t=1h, the reactor's methanol production rises to 11.1 kg/s. As the reactor has not yet reached steady-state, the time step from t=1-2 hours is split multiple times. Between t=1.42-

1.92 hours, the distillation column begins separating methanol from water, averaging 5.54 kg/s. This indicates that the column starts production at around t=1.67h, as described in subsection 4.3.1. After t=1.92 h, the entire system achieves steady-state production, resulting in a total startup time of less than 2 hours with the chosen parameters.

Variable	**(VD)**	**(PF)**	**YACOP**	**unit**
CO_2 Feed	88	80.5	72-76.428	t/h
CO_2 out	5.82	3.825	0	t/h
H_2 Feed	12.1 (from water feed)	11	10.988	t/h
H_2 out	0.87	0.51	0	t/h
catalyst mass	44.5	44.5	44.5	t
Water Feed	108.1	-	98.89	t/h
Water out	33.7	36.39	31.32	t/h
Methanol out	59.3	55.1	54-55.8	t/h
O_2	96	-	74.34	t/h
Power Electrolysis	645.1	-	517-610	MW_{el}
Power Synthesis	21.5	17.36	15-18.7	MW_{el}
Thermal Energy (net)	49.4	24.19	136	MW_{th}
Thermal Energy without electrolyzer cooling			60	MW_{th}
Cooling needs	-	47.5	60-64 (gross)	MW_{th}
Reboiler Duty	21.2	21.2	22	MW_{th}
Condenser Duty	21.6	-	19	MW_{th}

Table 4.4: Comparison of the methanol synthesis plants of Van-Dal et al. (VD) [VDB13], Pérez-Fortes et al. (PF)[PFSBT16] and the in YACOP implemented components.

Table 4.4 is a summary of the simulation results of Van-Dal et al. [VDB13], Pérez-Fortes et al. [PFSBT16] and the implemented System in YACOP.
As PF did not include the H_2 production in their plant, the electric load and cooling duty of the electrolyzer system was considered separately. Overall, the production of VD is approximately 7% higher than that of PF and the synthesis in YACOP. This higher yield is driven by an increased CO_2 and H_2 flows of a similar magnitude. In the case of hydrogen production, VD utilizes a constant 4.8 kWh/m^3 electric energy for hydrogen production, whereas the electrolyzer in YACOP operates within a range of 3.95 to 4.88 kWh/m^3, explaining the lower electricity consumption in hydrogen production. The figure of 3.95 kWh/m^3 or 47 kWh/kg_{H_2} reported in YACOP represents the lower end of the energy consumption range compared to the findings of Bertuccioli et al. [LADF14].
It is important to note that the implemented reactor system operates without the utilization of the purge valve of the synthesis subsystem presented in section 3.4. This means there is no waste of hydrogen or carbon dioxide/monoxide, due to the slightly altered inflow concentrations of the reactor.

Parameter	value	unit
H_2 inflow system	3.05	kg/s
CO_2 inflow system	22.36	kg/s
Recycling stream	ca. 100	kg/s

Table 4.5: Reactor inflows for the System evaluation for the YACOP reactor during steady state.

4.4.2 Partial Load Behavior

This subsection is investigating the systems behavior during the sudden change of the hydrogen load from 70% to 100%, as well as the change back to 70%. Key component in this scenario is the synthesis subsystem, because the hydrogen production of the electrolyzer system is directly connected to the hydrogen inflow of the synthesis subsystem, meaning a delay of production is visible here. The distillation column on the other hand is reacting to load changes without delay as shown in figure 6.8.

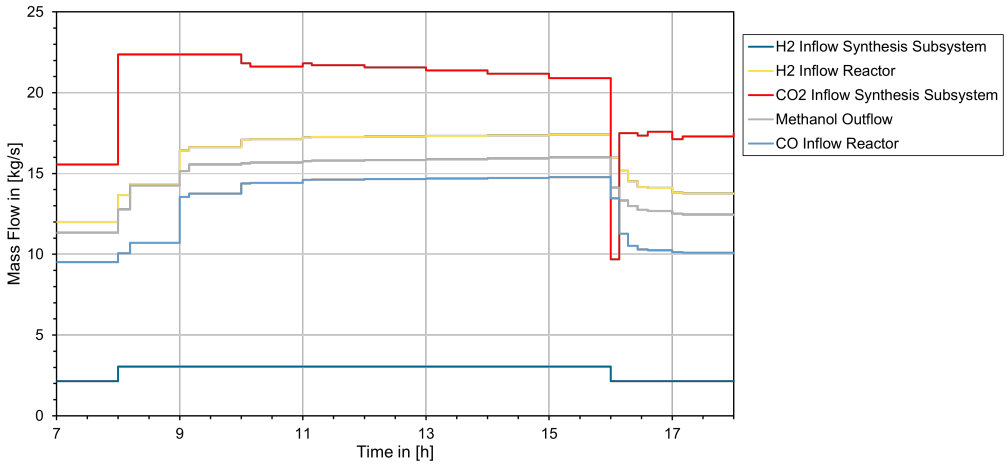

Figure 4.15: Inflows of the synthesis system and the reactor under load changes with methanol production.

In figure 4.15, the inflows of the reactor and the synthesis subsystem are plotted over a time of 12 hours. As the reactor is relatively large, with a calculated residence time of approximately 500 seconds, it requires multiple iterations for the concentrations in the reactor to adapt to the load changes. In this case, it takes approximately 90 minutes and for this adjustment to occur. This phenomenon can be observed more clearly in figure 4.16, where the recycle stream is plotted along with the load. It is evident that the hydrogen inflow, plotted on the secondary y-axis, is delayed due to the startup of the remaining stacks in the electrolyzer system. Consequently, the carbon dioxide concentration remains higher for the first 30 minutes after the load change, while the hydrogen flow in the recycle stream remains lower.
Although the delay in hydrogen inflow, methanol production increases immediately

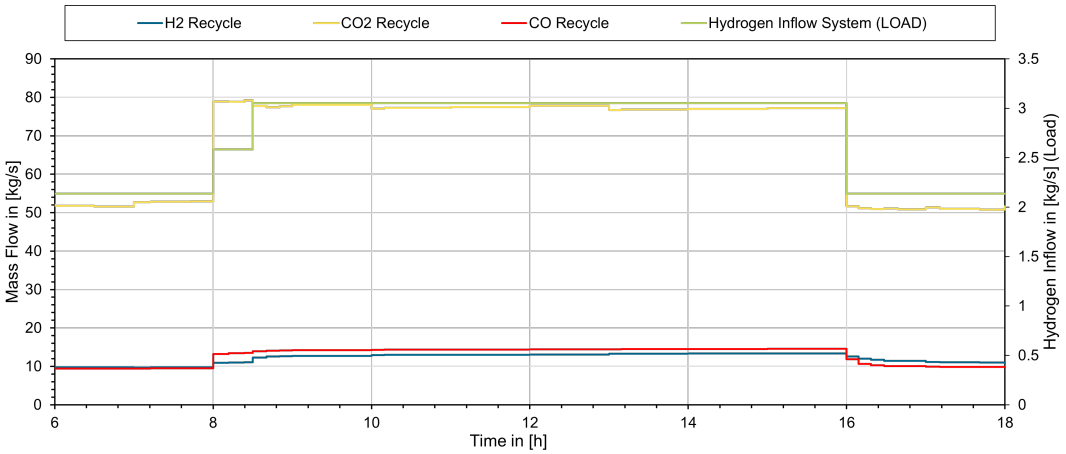

Figure 4.16: Mass flows of the recycle stream in the synthesis subsystem during load changes.

after the load change. This is accompanied by an increase in the flow of carbon monoxide and carbon dioxide flow in the recycle stream.
The transition to a 70% production load facilitates a quicker return to a steady-state. This is because both the hydrogen and carbon dioxide streams through the reactor promptly adjust to their steady-state values. Consequently, fewer additional time steps are needed to determine the new steady recycle flow, as depicted in figure 4.15. There is significant drop in CO_2 inflow after t=16h, attributed to the recycle stream still containing a substantial amount of CO_2. Once the recycle stream is updated, the CO_2 inflow rises again to its steady-state value in accordance with 70 % load setting.

5 Conclusion

This chapter summarizes the findings of the thesis and provides a perspective on domains in which the models can be improved in the future. The primary objective of the thesis was to determine whether YACOP is a suitable platform for modeling chemical processes, particularly in conjunction with renewable energy sources, and to identify critical components during production. This work confirms that YACOP is adept at modeling the energetic aspects of methanol synthesis, including the synthesis reactor itself. The incorporation of hydrogen production as fuel for the synthesis was achieved through the implementation of both single-stack and multiple-stacks electrolyzer models. Additionally, the purification process was modeled using a distillation column model capable of accurately predicting steady-state values of reboiler power and condenser power. Importantly, all models were designed to account for startup dynamics, which can be customized using appropriate parameters.
The electrolyzer model was primarily based on the approaches outlined by Ulleberg [Ull03] and Sanchez et al. [SARCJ18]. Startup considerations were incorporated by a production limitation over a defined period of time and adjusting efficiency based on load and stack temperature, mainly based on the information provided by Bertuccioli et al. [LADF14] and Lüke et al. [LZ20] regarding modern electrolyzers.
Additionally, alternative methodologies proposed by Varela et al. [VMZ21] and Zheng et al. [ZYBM22] were considered, particularly those suggesting different operating modes for the electrolyzer stacks to mitigate periods of renewable power shortages. Section 5.1 provides a comprehensive overview of these details. The implemented model demonstrates similar performance to that proposed by Ulleberg [Ull03], while also aligning with the more recent statistical findings of Bertuccioli et al. [LADF14] regarding modern alkaline electrolyzers.
The reactor model drew its foundation from Behr et al. [BAJV16], integrating the kinetics outline by Mignard et al. [MP08]. The validation was conducted using the kinetic model source provided by Bussche et al. [Bus96]. Minor and non-critical variations along the reactor length were observed primarily at lower inlet temperatures, resulting in a minimal overestimation of the required catalyst mass. Nonetheless, the reactor model effectively predicts reaction equilibrium without constrains. The limitations of this kinetic modeling approach have been summarized in section 3.4.1. Startup behavior is contingent upon the heating system, reactor inflow, and size, requiring pre-filling and heating before production start. During steady-state, the reactor accurately calculates raw methanol production based on current inflows while determining pure methanol concentration in the product. In future analysis, especially during techno-economic evaluations, consideration of alternative kinetic models, such as the approach by Slotboom et al. [SBP$^+$20], could be explored and compared

to the model employed in this study, particularly given the significantly higher yields reported by Nyari et al.[NIT+22].

The distillation column model is based on the work of Behr et al. [BAJV16] and Nitsche et al. [Nit14]. Employing the McCabe-Thiele-Method, the model accurately calculates product and waste concentrations for a given feed stream while reliably predicting reboiler and condenser duties during steady state. Remarkably, with comparable parameters, the model proposed in this study yields nearly identical results to those reported by Pérez-Fortes et al. [PFSBT16].

Regarding the startup simulation, the works of Neves et al. [NAM99]and Fabro et al. [FAN05] served as primary references. The implemented distillation column model successfully replicates these works in a traceable way. However, further validation is needed to confirm the model's applicability across diverse parameter sets. For instance, discrepancies arise when compared to findings by Wang et al. [WLWW03], who report significantly longer filling durations. Additional insights and limitations are detailed in section 5.2.

The methanol synthesis system implemented in this study is a simplified version inspired by the designs proposed by Van-Dal et al. [VDB13] and Pérez-Fortes et al. [PFSBT16]. The simplifications primarily revolve around the complex heat exchange network, which has been streamlined to focus on heat balances, and the exclusion of the carbon capture unit.

The results presented in table 4.4 demonstrate that the implemented models, yield similar results in comparison to the studies published by Van-Dal and Pérez-Fortes. [VDB13] [PFSBT16]. Although the distillation column exhibits nearly identical results, there are notable differences in the behavior of the electrolyzer system. The higher efficiency of the electrolyzer and the lower hydrogen feed in YACOP lead to a decrease in electrical power consumption compared to the results reported by Van-Dal. Specifically, while Van-Dal reported 11.24 MW/ton methanol, the system in YACOP forecasts 9.83-11.5 MW/ton methanol, with the higher value observed only during the startup phase of the cold electrolyzer system.

During the evaluation of the results, no single component could be identified as the primary bottleneck during startup procedures. Both the methanol reactor and the distillation column exhibited delays in production of similar magnitudes, with both depending on the flow rate of substance that is filling the components. The electrolyzer system is limiting production mainly due to the absence of a predictive operating strategy, which could, in reality, be implemented. Such a strategy would lead to an earlier start of nominal hydrogen production, consequently leading to earlier filling of the reactor as discussed in section 4.4.

The potential implementation of a methanol tank to initiate the filling process of the distillation column could also be investigated in the future. However, the heat used in the reboiler might not yet be provided by the methanol reactor if this method is implemented. Assessing the feasibility of this is approach becomes an economic question as well, especially regarding the investment costs associated with the methanol tank. Currently, the control strategy relies on regulating hydrogen inflow, which leads

to prolonged adaptation times for the reactor in response to load changes, specially variations hydrogen inflow. This issue could potentially be mitigated by utilizing the purge valve of the synthesis subsystem to maintain a more consistent mixture of hydrogen, CO_2 and CO in the reactor. Nonetheless, such a modification would require an economic analysis to evaluate whether diverting this stream reasonable, or if it could be utilized elsewhere, perhaps in a gas turbine application, as discussed in the works of Pérez-Fortes et al. [PFSBT16].
While all three components have been validated in their implemented functionality, the system evaluation and control strategy are difficult to address, as a lot of aspects require a broader approach including the economics of the single components, as well as the educt and product flows. This wider method could require alteration of the implemented models regarding their functionalities or production modes e.g. stand-by states for the distillation column or the electrolyzer.

5.1 Limits of the implemented electrolyzer model

In future developments, the electrolyzer system could be expanded, particularly concerning optimal stack deployment or standby state utilization. Integration with other components such as the methanol synthesis subsystem could enhance the electrolyzer system's performance through the implementation of a more sophisticated control strategy, potentially even a predictive control approach. As illustrated in Figure4.4, certain stacks undergo the startup process only to be shutdown afterwards due to the risen production capacity of higher-priority stacks. Momentarily, the reactor and its hydrogen demand dictate production, rendering this control strategy effective. However, when incorporating the electrolyzer system as a power-controlled system, minimizing startup and shutdown cycles becomes imperative. Tackling these startup issues aligns with an economic assessment of the system, where in some cases the production of hydrogen with electricity originating from the power grid might be economically sensible.

5.2 Limits of the Distillation Column Model

The assumption of ideal separation in the distillation column is reasonable for high condenser concentrations of methanol, which are typically desired for fuel production (e.g., 99.7% purity as cited in [PFSBT16]). In such cases, the mass flow error remains below 0.03%., which is acceptable. However, when dealing with lower methanol concentrations in the condenser, this error increases due to differences in molar masses. This becomes particularly relevant for seasonal simulations, where varying conditions must be considered.
Anticipating the distillation column's susceptibility to flooding and weeping without proper dimensioning of the column poses a significant challenge. This is an elaborate task and would need to be repeated even for minor parameter adjustments. Additionally, incorporating various important parameters such as type of tray, tray-hole

size, weir height, foam factor, among others, significantly increases the complexity. Since the simulation primarily focuses on the system level, attempting to encompass all these aspects would result in an overly complex and time-consuming process.
The fixed temperature requirement for the inflow imposed a very strict limitation. While it simplifies the calculation of the inner column process, as detailed in section 3.5, it leads to unreasonably high condenser duty during the startup process. Introducing a colder inflow temperature could mitigate this issue by aligning the temperature with the average fluid temperature in the column at steady-state, rather than the temperature of the feed tray. To address this presently, the condenser duty could be offset by the heating duty of an inlet heater or heat exchanger, which is necessary for the integration of the distillation column with other components, as discussed in section3.2. Realistically, during the filling process, the feed temperature would indeed be lower than that the steady-state temperature to avoid excessive condenser duty.
As noted in section 3.5, bell bottom trays can prevent weeping since the bells cover the vapor holes in the tray. This feature could be advantageous for shutting down the reboiler and condenser without the trays emptying into the bottom tray, a problem that occurs with sieve trays. By maintaining the column at or near steady-state temperature, short-term drops in the feed stream could be absorbed. Conversely, with sieve trays, if the minimum vapor flow condition or minimum partial load condition is not met, the trays would weep into the trays below, eventually necessitating a refill of the distillation column. Running the distillation column under minimum partial load conditions, without mass flow into the column and without product extraction, could potentially avoid the need for a new filling process. However, there is no literature available on these procedures to support this approach.
The validation of the startup calculation is primarily based on the works of Neves et al. [NAM99] and Fabro et al. [FAN05]. In contrast, other authors such as Wang et al. [WLWW03], or Eden et al [EKHJ00] report longer startup times. Unfortunately, the columns sizes and inflow values are not provided in the work of Wang et al. These significant variations suggest that further research is necessary to accurately predict and validate the startup time and its calculation.

6 Appendix

6.1 Alkaline Electrolyzer

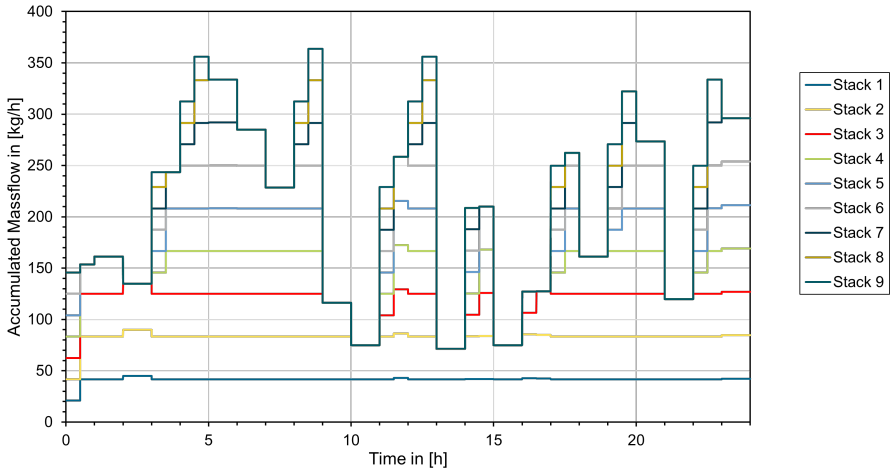

Figure 6.1: Accumulated hydrogen production for $n = 9$ stacks with $t_{startup} = 1800s$.

Figure 6.1 shows the accumulated hydrogen production of all nine stacks with a startup time of 1800 seconds. The total hydrogen production is thus plotted by line 'Stack 9'. The hydrogen demand is altered at every full hour. Noticeable are the changes in number of active stacks when the hydrogen demand is not changed, which is either due to insufficient production capacity by the electrolyzer stacks, or the rising production capacity of warm stacks in contrast to cold stacks. Parameters are listed in table 6.4.
The function in 6.1 shows the distribution of water to the individual electrolyzer stacks. `self.fl_cons` contains the fluid flow connectors of the flow-splitter that are connected to the water inflows of the electrolyzer stacks.

```
def _calc_spr_cons(self):
    """
    Calculates the water flow rate to the individual stacks, based on
    their states.
    Returns
    -------
    total_in: water inflow that is not converted to hydrogen
    stack_times(list): list containing the active stack times
    """
```

```
10      total_in = self.water_mf
11      new_time_step = False
12      if self.t_on_stacks is not None:
13          stack_times = list(self.t_on_stacks)
14      else:
15          stack_times = [0 * self.u_s] * self.n_stacks
16      for i, con in enumerate(self.fl_cons):
17          if total_in > 0 * self.u_mf:  # Water inflow is not yet
18          distributed fully -> Stack is active
19              stack_times[i] += self.time_step
20              if stack_times[i] - self.time_step >= self.t_startup:
21                  mf_factor = 1  # stack capacity 100%
22              elif self.t_startup >= stack_times[i] >= 0 * self.u_s:
23                  mf_factor = 0.5  # stack capacity 50%
24              elif self.t_startup < stack_times[i] < self.t_startup +
25              self.time_step:
26                  time_1 = stack_times[i] - self.t_startup
27                  time_05 = self.time_step - time_1
28                  self.new_time_step = time_05
29                  new_time_step = True
30                  mf_factor = 0.5  # stack capacity 50% until new time
31                  step
32              else:
33                  mf_factor = 0.5  # stack capacity 50%
34          else:  # no water inflow (left) -> stack is idle
35              stack_times[i] = 0 * self.u_s
36              mf_factor = 0
37          if total_in >= self.H2O_m_nom_stack * mf_factor:  # water mass
38          flow is greater than the nominal load
39              mass_flow = -self.H2O_m_nom_stack * mf_factor
40              total_in -= self.H2O_m_nom_stack * mf_factor
41          elif (self.min_partial_load * self.H2O_m_nom_stack <= total_in
        <
42                self.H2O_m_nom_stack * mf_factor):  # water mass flow is
43                within load limits
44              mass_flow = -total_in
45              total_in = 0 * self.u_mf
46          else:  # water mass flow is distributed to the previous stacks
47              mass_flow = 0 * self.u_mf
48              stack_times[i] = 0 * self.u_s
49              if i >= 1 and total_in != 0 * self.u_mf:
50                  count = 0
51                  for j, prev_con in enumerate(self.fl_cons[:i]):
52                      if stack_times[j] - self.time_step >=
53                      self.t_startup:
54                          mf = prev_con.mf - total_in / i
55                          count += 1
56                          prev_con.reset()
57                          prev_con.mf = mf
58                          prev_con.t = self.H2O_in_flow.t
59                  total_in -= total_in / i * count
60          con.mf = mass_flow
61          con.t = self.H2O_in_flow.t
```

```
62      if new_time_step:
63          self.logger.info('new_time_step in elec_system: ' +
64          str(max(time_05, 10*self.u_s)))
65      return dict(total_in=total_in, stack_times=stack_times)
```

Listing 6.1: Distribution of water to the individual electrolyzer stacks in the electrolyzer system.

6.2 Methanol Reactor

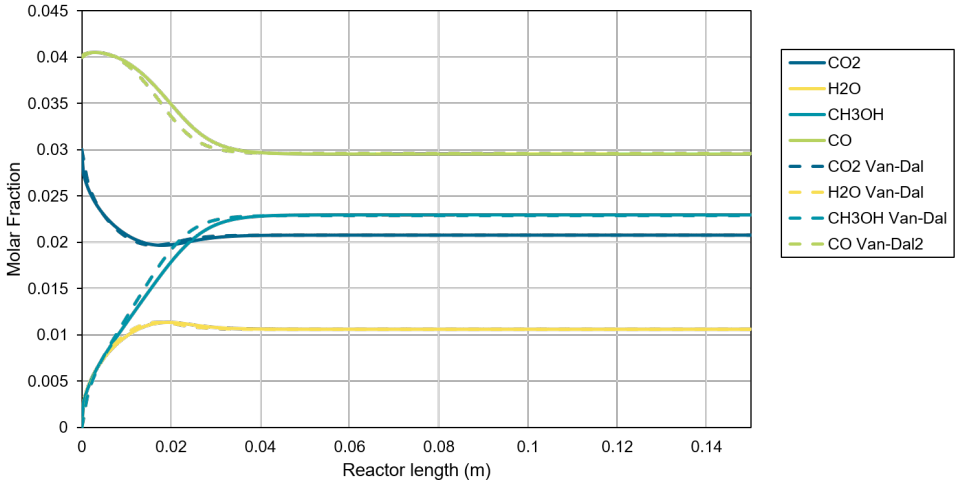

Figure 6.2: Molar Fractions of the reactor generated with the kinetics of Van-Dal et al./Mignard et al., in comparison to the source material. [VDB13], [MP08]

Figure 6.2 shows the molar fractions in the reactor for different kinetic parameters, in this case the parameters by Mignard et al. [MP08], which were also used by Van-Dal et al. [VDB13]. The concentration profile strongly resembles the profile in figure 4.7, with the only significant difference being the local maxima and minima in the first 0.03 m of the reactor. This is a result of the adjustment of the reaction activation energies seen in table 2.4 [VDB13]. Similar to the slight delay in concentration in figure 4.7, there is also a variation of the concentration profiles in axial direction. Again, also Van-Dal et al. do not specifically mention the energy balance that was used, or if the implemented reactor in ASPEN®is ideal.
The same kinetic parameters were used by Perez et al. [PFSBT16]. A comparison is shown in figure 6.3. Perez et al. implemented the reactor to be an ideal plug flow reactor in CHEMCAD, and the concentration profiles are quite well replicated. This could lead to the assumption that Bussche et al. and Van-Dal et al. did not use an ideal reactor in their simulations. Along with the closely resembled concentration profiles, the adiabatic outlet temperature of 561 K published by Perez et al. only slightly varies from the calculated outlet temperature of 562.7 K in YACOP. This

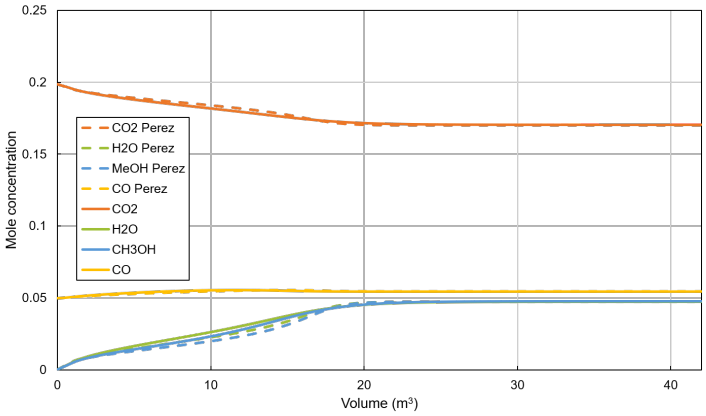

Figure 6.3: Molar Fractions of the reactor generated with the kinetics of Mignard et al., in comparison to the reactor parameters of Perez et al. [PFSBT16]

could be the consequence of slightly different heat capacities or reaction enthalpies, which in YACOP are interpolated from data sheets.

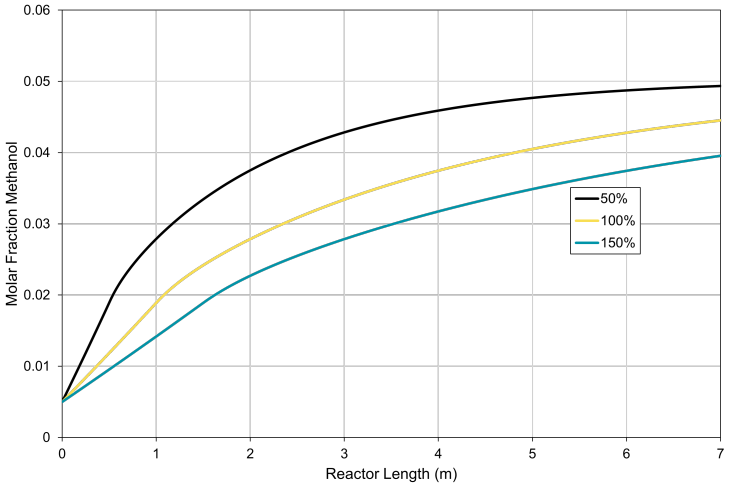

Figure 6.4: Methanol concentration profile of the reactor mass flow variation.

In figure 6.4 the methanol concentration profile for a variation of the total mass flow is shown. The parameters were chosen as close as possible to the parameters chosen by Manenti et al. [MCR11]. Unfortunately, some parameters were not documented, like the total catalyst mass or the heat transfer coefficient between the reactor wall and the reactants. The parameters are summarized in table 6.1. By comparing figure 6.4 with the reference figure 6.5, it is safe to assume that the reactor in YACOP reacts similarly to mass flow changes. It is important to note the methanol yields at the end of the reactor. Manenti et al. did take the formation of CO and H_2 from CH_4 and H_2O into account, which was not implemented in YACOP (Methane is inert in YACOP). This could result in higher methanol yields, as CO and H_2 are formed in the reactor while they are consumed by the RWGS reaction and the methanol synthesis reaction. This makes the results difficult to compare. Additionally, Manenti et al. used a mass flow based pseudo-homogeneous model, which yields different results than molar flow based pseudo-homogeneous models like the one implemented in YACOP [MCR11].

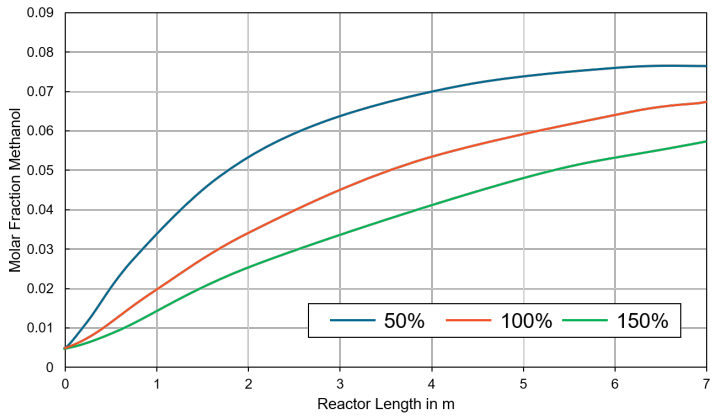

Figure 6.5: Methanol concentration profile of the reactor mass flow variation of Manenti et al. [MCR11]

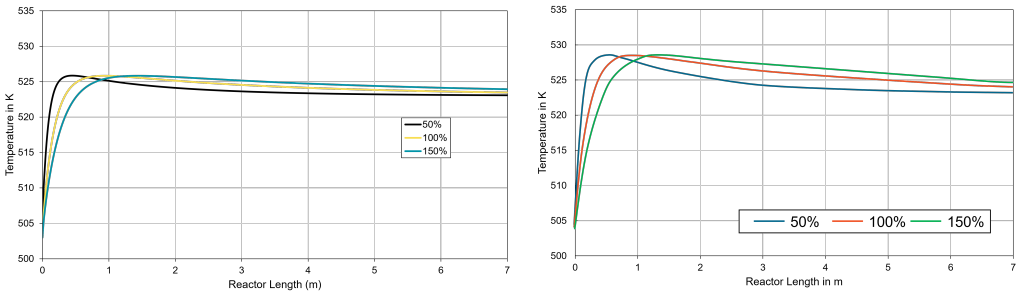

Figure 6.6: Comparison of the Temperature profiles calculated by YACOP(left) and Manenti et al.[MCR11] (right) under mass flow variations of +- 50% of the nominal mass flow.

The temperature profile is affected by the mass flow variation as well. In figure 6.6 the temperature profiles calculated by YACOP (left) and Manenti et al. (right) are displayed. While the behavior is similar, there are slight differences in the peaks of the temperature profiles in the beginning of the reactor. The overshooting of the temperatures reported by Manenti et al. is greater than the overshooting predicted by YACOP, leading to a flatter course of the profiles throughout the reactor. One explanation could be that the assumed HTC between the gases and the reactor wall was overestimated in YACOP, leading to a faster alignment of the temperature profiles to the reactor wall temperature of 523 K. This could also explain the lower peak temperatures. On the other hand, the additionally produced methanol for Manenti et al. would heat up the gases further, as the synthesis reaction is exothermal. Figure 6.4 and figure 6.5 clearly show that the system has not reached its equilibrium at the

Operating Conditions		
Catalyst		
Density	1770	kg/m^3
Porosity	not mentioned, assumed 0.5	-
Mass	not mentioned, assumed 1.2	kg
Pellet diameter	0.000547	m
Reactor		
Diameter	0.08404	m
Length	7	m
T_{inlet}	503	K
T_{wall}	540	K
$HTC_{gas-wall}$	300	$W/K/m^2$
p_{inlet}	77	bar
mass flow	2.8e-5	kg/s
Feed composition		
CO	4.6	mol%
H_2O	0.04	mol%
$MeOH$	0.5	mol%
H_2	65.9	mol%
CO_2	9.4	mol%
CH_4	9.3	mol%
$Inert$	10.26	mol%

Table 6.1: Operating Conditions for the Simulation of Manenti et al. [MCR11]

end of the reactor, meaning methanol is still formed in an exothermal reaction, while the amount in the reactor calculated by Manenti et al. is clearly higher, meaning more heat is introduced. Overall, the comparison between the results Manenti et al. presented to the results of this work is difficult because of the many discrepancies in the reactor models and insufficient documentation of the parameters used.

6.3 Distillation Column

Operating Conditions for the startup validation			
Parameter	value	unit	
	number of trays	20	-
	feed stage	14	-
	diameter column	1.2	m
	height column	8	m
	Reboiler Power	4	MW
	tray size	0.04	m^3
	Reboiler size	0.5	m^3
	Condenser size	1.43	m^3
	column mass	500	kg
	Heat capacity column	0.5	kJ/kg/K
	methanol concentration product	99.9	%(molar)
	methanol concentration waste	1	%(molar)

Table 6.2: Operating Conditions of the Distillation Column for the startup validation and Neves et al. [NAM99]

Wang et al. [WLWW03] reported the temperature profile shown in figure 6.7 after t=2 hours of their startup simulation, and not in steady state, which is reached at t=2.8 hours or t=3.8h with a total reflux process. It is important to note, that in their report, the column is filled from the bottom up, and not from the feed stage, prolonging the filling process as the stages below the can be filled quicker from the feed stage.

Operating Conditions during steady state			
Parameter	value	unit	
	number of trays	54	-
	feed stage	44	-
	diameter column	4.4	m
	height column	25	m
	Reboiler Power	25	MW
	tray size	0.64	m^3
	Reboiler size	4	m^3
	Condenser size	3	m^3
	column mass	5	t
	Heat capacity column	0.5	kJ/kg/K
	methanol concentration product	99.9	%(molar)
	methanol concentration waste	0.03	%(molar)

Table 6.3: Operating Conditions of the Distillation Column in section 4.3.2 and figure 6.8

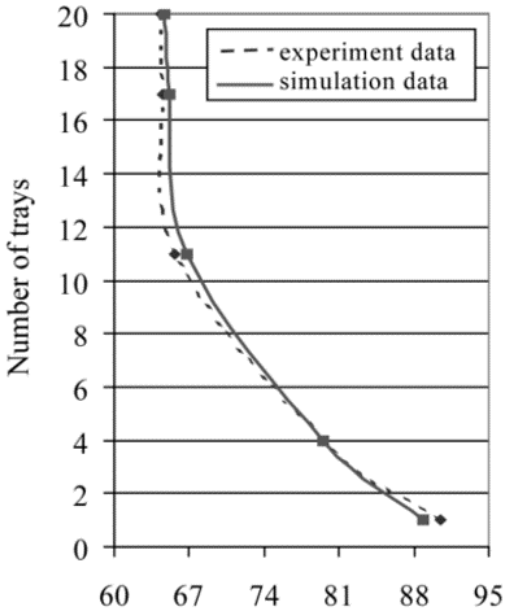

Figure 6.7: Tray temperatures reported by Wang et al. for n=20 stages

The functions displayed at 6.2 are used to calculate the vapor-liquid-equilibrium in the distillation column's top section, starting with the feed concentration at the feed stage. From here, the liquid concentration in the tray above the current tray is calculated from the vapor concentration in the current tray. The tray efficiency is considered through a lower number of theoretical stages, calculated from the actual number of stages.

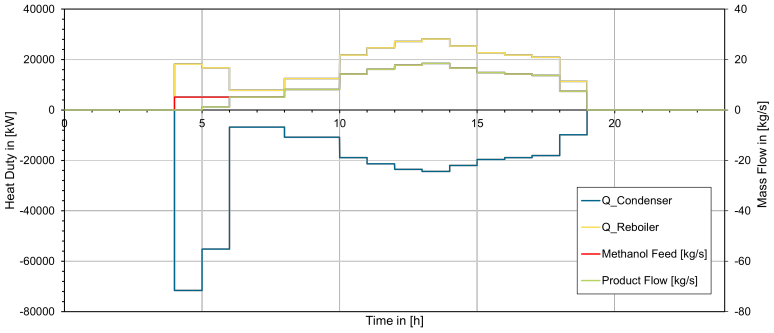

Figure 6.8: Condenser and Reboiler duties for varying mass flows.

```
def _calc_top(self):
    """
    Calculate the product molar fraction.
    """
    y1_top = self.x_top
    if self.partial_load == 0:
        y1_top = self.x_d
    elif self.partial_load != 0 and not self.steady:
        x_f = self.x_feed_new
        c_verst = self.x_d / (self.v + 1)  # Verstaerkungsgerade Y-
    Achsenabschnitt
        y_f = self.v * x_f / (self.v + 1) + c_verst
        m = (y_f - self.x_waste) / (x_f - self.x_waste)
        c_ab = self.x_waste * (1 - m)  # Abtriebsgerade Y-
    Achsenschnittpunkt

        x_bott, t_bott = ([self._calc_bottom_molar_mass(c_ab, m, x_f)
    ],
                          [self.t_bottom])
        x_feed, t_feed = self._calc_strip_molar_mass(x_bott, t_bott,
    c_ab,
                                                     x_f,
                                                     m)
        x_ch3oh, t_profile = self._calc_rect_molar_mass(x_feed, t_feed
    ,
                                                        c_verst)
        y1_top = x_ch3oh[-1]
return y1_top

x_top = Attribute(tag=Attribute.TAG_PREVIOUS_NEW,
                  functions=[_calc_top])

def _calc_rect_molar_mass(self, x_ch3oh, t_profile, c_verst):
    """
    For startup calculation.
    Calculate the molar fractions above the feed (rectifying section).
    """
    for i in range(int((self.n_stages - self.feed_stage) *
                       self.tray_efficiency), self.n_stages - 1):
        y_next_stage = self._calc_VLE(x_ch3oh[i])
        x1_top = min((y_next_stage - c_verst) *
                     (self.v + 1) / self.v, y_next_stage)
        t_profile.append(self._get_t(self.p_inlet, x_ch3oh[-1]))
        x_ch3oh.append(x1_top)
    return x_ch3oh, t_profile

def _get_activity_coeff(self, x1):
    """
    Calculate the activity coefficients using margules method
    """
    gamma1 = math.e ** ((1 - x1) ** 2 *
            (self.a12 + 2 * (self.a21 - self.a12) * x1))
    gamma2 = math.e ** (x1 ** 2 *
```

```
49              (self.a21 + 2 * (self.a12 - self.a21) * (1 - x1)))
50      return gamma1, gamma2
51
52  def _calc_VLE(self, x1):
53      """
54      Calculate the Vapor Liquid Equilibrium for the given concentration
        .
55      """
56      t = self._get_t(self.p_inlet, x1)
57      self._change_cond(t, self.p_inlet)
58      gamma1, gamma2 = self._get_activity_coeff(x1)
59      p1 = max(x1 * gamma1 * self.CH3OH.p_0, 0)
60      p2 = max((1 - x1) * gamma2 * self.H2O.p_0, 0)
61      p = p1 + p2
62      y_next_stage = p1 / p
63      return y_next_stage
```

Listing 6.2: VLE calculation in the top part of the distillation column.

6.4 Methanol Synthesis System

Alkaline Electrolyzer System		
Parameter	value	unit
operating pressure	40	bar
nominal temperature	90	°C
system power	20	MW
number of stacks	9	
stack power	2.22	MW
startup time	1800	s
system	0.1042	kg/s
system	2.16	m^3/s
stack	0.01158	kg/s
stack	0.1288	m^3/s

Table 6.4: Electrolyzer parameters for the first System evaluation

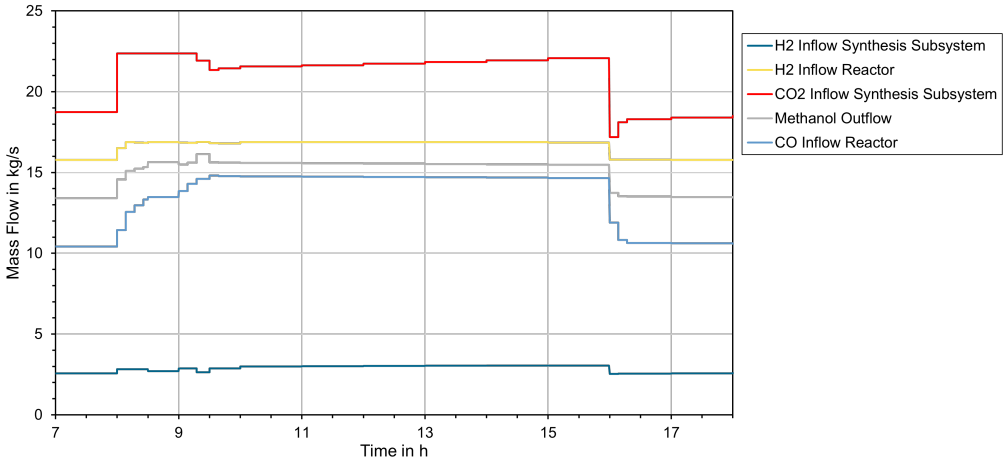

Figure 6.9: Inflows of the synthesis system and the reactor under load changes with carbon monoxide plotted.

Methanol Reactor

Parameter	value	unit
maximum mass flow	129.889	kg/s
recycle ratio	0.9	-
catalyst mass	44500	kg
reactor mass (without catalyst)	60000	kg
cp	0.5	kJ/kg/K
length reactor	7	m
diameter reactor	3	m
diameter tube	0.05	m
number of tubes	3000	-
isolation thickness	0.2	m
thermal conductivity isolation	0.035	W/m/K
bed porosity	0.4	-
$cp_{catalyst}$	0.4211	kJ/kg/K
efficiency electric heating	0.95	-
heating power	2000	kW
htc gas reactor wall	200	$W/K/m^2$
htc wall environment	0.5	$W/K/m^2$
pressure reactor inlet	76.39	bar
temperature inlet	483.15	K
temperature inner wall	550	K
temperature outer wall	320	K

Table 6.5: Reactor parameters for the first System evaluation

Distillation Column

Parameter	value	unit
number of trays	54	-
feed stage	44	-
diameter column	4.4	m
height column	25	m
Reboiler Power	25	MW
tray size	0.64	m^3
Reboiler size	4	m^3
Condenser size	3	m^3
column mass	5	t
Heat capacity column	0.5	kJ/kg/K
methanol concentration product	99.9	%(molar)
methanol concentration waste	0.03	%(molar)

Table 6.6: Distillation column parameters for the first System evaluation

Bibliography

[Alv16] Marc Alvarado. The changing face of the global methanol industry. (3), 2016.

[BAJV16] Arno Behr, David W. Agar, Jakob Jörissen, and Andreas J. Vorholt. *Einführung in die Technische Chemie*. Lehrbuch. Springer Spektrum, Berlin and Heidelberg, 2. auflage edition, 2016.

[BM16] Giulia Bozzano and Flavio Manenti. Efficient methanol synthesis: Perspectives, technologies and optimization strategies. *Progress in Energy and Combustion Science*, 56:71–105, 2016.

[BT20] Jörn Brauns and Thomas Turek. Alkaline water electrolysis powered by renewable energy: A review. *Processes*, 8(2):248, 2020.

[Bus96] Bussche, K. M. V., et al. A steady-state kinetic model for methanol synthesis and the water gas shift reaction on a commercial cu/zno/al2o3 catalyst. *JOURNAL OF CATALYSIS 161*, pages 1–10, 1996.

[Car12] Carbon Recycle International. George olah methanol plant, 2012.

[Car22] Carbon Recycle International. Shunli plant, 2022.

[CDJ+88] G. C. Chinchen, P. J. Denny, J. R. Jennings, M. S. Spencer, and K. C. Waugh. Synthesis of methanol. *Applied Catalysis*, 36:1–65, 1988.

[Dai16] Issam Dairanieh, editor. *Carbon dioxide utilization (CO2U): ICEF Roadmap*, 2016, 2016.

[EKHJ00] Mario R. Eden, Arne Koggersbøl, Louis Hallager, and Sten B. Jørgensen. Dynamics and control during startup of heat integrated distillation column. *Computers & Chemical Engineering*, 24(2-7):1091–1097, 2000.

[FAN05] João Alberto Fabro, L.V.R. Arruda, and Flávio Neves. Startup of a distillation column using intelligent control techniques. *Computers & Chemical Engineering*, 30(2):309–320, 2005.

[GRZ17] Noris Gallandat, Krzysztof Romanowicz, and Andreas Züttel. An analytical model for the electrolyser performance derived from materials parameters. *Journal of Power and Energy Engineering*, 05(10):34–49, 2017.

[GSB88] G. H. Graaf, E. J. Stamhuis, and A.A.C.M. Beenackers. Kinetics of low-pressure methanol synthesis. *Chemical Engineering Science*, 43(12):3185–3195, 1988.

[HZA+24] Danji Huang, Zhiyao Zhong, Xiaomeng Ai, Kewei Hu, Binyu Xiong, Qunlei Wen, Jiakun Fang, and Shijie Cheng. Size design strategy for scaling up alkaline water electrolysis stack integrated with renewable energy source: A multiphysics modeling approach. *Energy Conversion and Management*, 300:117955, 2024.

[Jeo22] Dong Hwi Jeong. Methanol production reactor simulation and optimization under kinetic parameter uncertainty conditions. *Chemical Engineering Research and Design*, 185:14–25, 2022.

[JS19] Tarun Jain and Parminder Singh. Estimation of activity coefficients for binary mixture vle data using matlab. *IARJSET*, 3(10):141–147, 2019.

[KLI82] K. KLIER. Catalytic synthesis of methanol from co/h2iv. the effects of carbon dioxide. *Journal of Catalysis*, 74(2):343–360, 1982.

[LADF14] Luca Bertuccioli, Alvin Chan, David Hart, and Franz Lehner. Development of water electrolysis in the european union. 2014.

[LDL+22] B. E. Lebrouhi, J. J. Djoupo, B. Lamrani, K. Benabdelaziz, and T. Kousksou. Global hydrogen development - a technological and geopolitical overview. *International Journal of Hydrogen Energy*, 47(11):7016–7048, 2022.

[LZ20] Lukas Lüke and Andrei Zschocke. Alkaline water electrolysis: Efficient bridge to co 2 –emission–free economy. *Chemie Ingenieur Technik*, 92(1-2):70–73, 2020.

[LZF19] Grazia Leonzio, Edwin Zondervan, and Pier Ugo Foscolo. Methanol production by co2 hydrogenation: Analysis and simulation of reactor performance. *International Journal of Hydrogen Energy*, 44(16):7915–7933, 2019.

[MCR11] Flavio Manenti, Silvia Cieri, and Marco Restelli. Considerations on the steady-state modeling of methanol synthesis fixed-bed reactor. *Chemical Engineering Science*, 66(2):152–162, 2011.

[MP08] Dimitri Mignard and Colin Pritchard. On the use of electrolytic hydrogen from variable renewable energies for the enhanced conversion of biomass to fuels. *Chemical Engineering Research and Design*, (86):473–487, 2008.

[MRG18] Steffi Matthischke, Stefan Roensch, and Robert Güttel. Start-up time and load range for the methanation of carbon dioxide in a fixed-bed recycle reactor. *Industrial & Engineering Chemistry Research*, 57(18):6391–6400, 2018.

[MWS22] Emanuele Moioli, Anne Wötzel, and Tilman Schildhauer. Feasibility assessment of small-scale methanol production via power-to-x. *Journal of Cleaner Production*, 359:132071, 2022.

[NAM99] Jr. Flávio Neves and Joseph Aguilar-Martin. Qualitative event-based expert supervision for transient condition monitoring. *Applied Intelligence*, 10(2/3):197–210, 1999.

[Nit14] Manfred Nitsche. *Kolonnen-Fibel: Für die Praxis im chemischen Anlagenbau*. Springer Vieweg, Berlin and Heidelberg, 2014.

[NIT+22] Judit Nyári, Daulet Izbassarov, Árpád I. Toldy, Ville Vuorinen, and Annukka Santasalo-Aarnio. Choice of the kinetic model significantly affects the outcome of techno-economic assessments of co2-based methanol synthesis. *Energy Conversion and Management*, 271:116200, 2022.

[Ost02] V. Ostrovskii. Mechanisms of methanol synthesis from hydrogen and carbon oxides at cu–zn-containing catalysts in the context of some fundamental problems of heterogeneous catalysis. *Catalysis Today*, 77(3):141–160, 2002.

[PFR+12] Maximilian Peter, Matthias B. Fichtl, Holger Ruland, Stefan Kaluza, Martin Muhler, and Olaf Hinrichsen. Detailed kinetic modeling of methanol synthesis over a ternary copper catalyst. *Chemical Engineering Journal*, 203:480–491, 2012.

[PFSBT16] Mar Pérez-Fortes, Jan C. Schöneberger, Aikaterini Boulamanti, and Evangelos Tzimas. Methanol synthesis using captured co2 as raw material: Techno-economic and environmental assessment. *Applied Energy*, 161:718–732, 2016.

[Roz89] Aleksandr Ya Rozovskii. Modern problems in the synthesis of methanol. *Russian Chemical Reviews*, 58(1):41–56, 1989.

[SARCJ18] Mónica Sánchez, Ernesto Amores, Lourdes Rodríguez, and Carmen Clemente-Jul. Semi-empirical model and experimental validation for the performance evaluation of a 15 kw alkaline water electrolyzer. *International Journal of Hydrogen Energy*, 43(45):20332–20345, 2018.

[SBP+20] Y. Slotboom, M. J. Bos, J. Pieper, V. Vrieswijk, B. Likozar, S.R.A. Kersten, and D.W.F. Brilman. Critical assessment of steady-state kinetic models for the synthesis of methanol over an industrial cu/zno/al2o3 catalyst. *Chemical Engineering Journal*, 389:124181, 2020.

[SJV+18] C. Seidel, A. Jörke, B. Vollbrecht, A. Seidel-Morgenstern, and A. Kienle. Kinetic modeling of methanol synthesis from renewable resources. *Chemical Engineering Science*, 175:130–138, 2018.

[SK18] Christopher Seibel and Jens-Wilhelm Kuhlmann. Dynamic water electrolysis in cross–sectoral processes. *Chemie Ingenieur Technik*, 90(10):1430–1436, 2018.

[SMC98] M. Sahibzada, I. S. Metcalfe, and D. Chadwick. Methanol synthesis from co/co2/h2over cu/zno/al2o3at differential and finite conversions. *Journal of Catalysis*, 174(2):111–118, 1998.

[The] The International Renewable Energy Agency. Green hydrogen cost reduction: Scaling up electrolysers to meet the 1.5c climate goal.

[Ull03] O. Ulleberg. Modeling of advanced alkaline electrolyzers: a system simulation approach. *International Journal of Hydrogen Energy*, 28(1):21–33, 2003.

[VDB13] Éverton Simões Van-Dal and Chakib Bouallou. Design and simulation of a methanol production plant from co2 hydrogenation. *Journal of Cleaner Production*, 57:38–45, 2013.

[VMZ21] Christopher Varela, Mahmoud Mostafa, and Edwin Zondervan. Modeling alkaline water electrolysis for power-to-x applications: A scheduling approach. *International Journal of Hydrogen Energy*, 46(14):9303–9313, 2021.

[WLWW03] Lin Wang, Pu Li, Günter Wozny, and Shuqing Wang. A startup model for simulation of batch distillation starting from a cold state. *Computers & Chemical Engineering*, 27(10):1485–1497, 2003.

[WS17] Thomas Willner and Anika Sievers. *Fortschrittliche alternative flüssige Brenn- und Kraftstoffe: Für Klimaschutz im globalen Rohstoffwandel [Positionspapier des ProcessNet-Arbeitsausschusses „Alternative flüssige und gasförmige Kraft- und Brennstoffe]*. 2017.

[ZYBM22] Yi Zheng, Shi You, Henrik W. Bindner, and Marie Münster. Optimal day-ahead dispatch of an alkaline electrolyser system concerning thermal–electric properties and state-transitional dynamics. *Applied Energy*, 307:118091, 2022.